University of Venda
Creating Future Leaders



Commensal searches for radio transients/variables in the data from the MHONGOOSE Large Survey Project

Vhuthu Miranda Tshilengo
16008396

February 2025

Thesis presented for the degree of Master of Science
in the Faculty of Science, Engineering and Agriculture
Department of Physics
UNIVERSITY OF VENDA

Supervisors: Prof. P. A. Woudt and Prof. N.E Maluta

© University of Venda

University of Venda
Creating Future Leaders

Abstract

The MeerKAT radio telescope in South Africa, a precursor to the mid-frequency component of the Square Kilometre Array (SKA1-Mid), offers exceptional sensitivity and a wide field of view, making it ideal for exploring time-domain radio astronomy. This dissertation presents the use of MeerKAT images from three different fields of the MHONGOOSE Large Survey Project (LSP) to identify radio transient and variable sources. Each of these three fields consists of 10 different epochs spanning time scales of order one month to over 1 year. The MHONGOOSE survey operates at a central observing frequency of 1.28 GHz. I made use of South African Radio Astronomy Observatory (SARAO) Science Data Processing (SDP) images of the MHONGOOSE observations, with source detection and variability analysis conducted via the Transient Pipeline (TraP) software on the Inter-University Institute for Data Intensive Astronomy (IDIA) cloud. The light curves generated by TraP enabled the calculation of variability parameters: the reduced weighted chi-square (χ^2) of a fit that assumes constant brightness represented by the symbol (η_ν) and the coefficient of variation (V_ν). Analysis of ten epochs across the fields of NGC 1566, NGC 5068, and NGC 1371 led to the identification of 31 variable sources. All variable sources identified in this study are associated with known objects listed in existing multi-wavelength catalogues and are classified as active galactic nuclei (AGNs). One radio transient was found in the NGC 1566 field "SRC76717", which is associated with a nearby flaring M dwarf located at a distance of 48 pc (Doyle et al., 2019).

Key words: Transients, Variables, Galaxies, and Radio astronomy.

© University of Venda

University of Venda
Creating Future Leaders

Acknowledgements

I would like to express my deepest gratitude to my supervisors, Prof. Patrick Woudt and Prof. Eric Maluta, for their unwavering support, encouragement, and invaluable contributions to this work. My sincere thanks also go to the University of Cape Town (UCT) colleagues—Dr. Zwidofhela, I sincerely thank Zwidofhela for consistently tracking my progress and checking in with me throughout my research. Your constant encouragement and dedication to ensuring I stay on track and complete my work have been invaluable. Thank you for your unwavering support, for always commenting on my work, guiding me and giving good suggestions. I want to express my heartfelt gratitude to Moses for his invaluable support throughout my research, particularly during the analysis and interpretation of my results. His significant role in shaping the outcome of my work cannot be overstated. Moses generously dedicated his time and expertise, guiding me in generating the plots and figures that became essential to my findings. I deeply appreciate his unwavering commitment, as he consistently checked on my progress and imparted his knowledge and skills. Amogelang, I would like to express my deepest gratitude to Amogelang for being there from the beginning of my research journey, both day and night. You always made time for me, teaching me how to run TraP and patiently explaining the basics of Python and Linux when I was utterly unfamiliar with them. Your guidance enabled me to start the methodology section of my research successfully, and through your support, I gained a deep understanding of these crucial tools. For that, I sincerely thank you. Thank you, Reika, for teaching me how to generate the Radio vs Optical plot. You helped me familiarize myself with GitHub, which enabled me to create clear and well-structured plots. Your guidance was instrumental, and I genuinely appreciate your support. I am particularly grateful to Alex Andersson (University of Oxford) for providing an advanced lecture on the TraP software, which was pivotal to this study.

I would also like to acknowledge my fellow students from the University of Venda—Tshifhiwa, Takalani, and Rebecca—for their unwavering support throughout my academic journey, particularly during my presentation and conference preparations. Their guidance and motivation have been invaluable. Additionally, I extend my gratitude to Khedzi and Ndivhuwo for their camaraderie and support, especially in helping me navigate LaTeX and providing essential guidance on its use. Their assistance has significantly contributed to my success. A special thank you to my family, parents' sisters, and brothers for their endless encouragement and belief in me. I am

© University of Venda

University of Venda
Creating Future Leaders

also deeply thankful to my friend Ndamulelo for the support. I want to thank myself for not giving up on this long, tiring journey of my master's research. It was challenging and demanding but incredibly interesting, filled with learning new things, travelling, and presenting. Lastly, I thank Almighty God for His protection and blessings throughout my journey. I acknowledge the financial support provided by the SARAO postgraduate bursary, which made this research possible. I accept that the ilifu cloud computing resource ilifu, which is a collaboration between the Cape Peninsula University of Technology, Stellenbosch University, Sol Plaatje University, the University of Cape Town, and the University of the Western Cape, was used. Contributions to the ilifu facility come from the Data Intensive Research Initiative of South Africa (DIRISA), the Computational Biology division at UCT, and the Inter-University Institute for Data Intensive Astronomy (IDIA), a collaboration between the University of Cape Town, the University of Pretoria, and the University of the Western Cape. This work used the Cube Analysis and Rendering Tool for Astronomy (CARTA) software. The South African Radio Astronomy Observatory, a division of the National Research Foundation and the Department of Science and Innovation, is responsible for operating the MeerKAT telescope. The 4K continuum images from the SDP, which were produced automatically by SARAO data pipeline, were used in the study. I want to extend my sincere gratitude to the University of Venda, Department of Physics, for allowing me to register and further my studies in Astronomy. Their support has been instrumental in advancing my academic and research pursuits.

© University of Venda

University of Venda
Creating Future Leaders

Declaration

I, Tshilengo Vhuthu Miranda (16008396), declare that I understand the meaning of plagiarism and declare that this master's thesis is my work. All content, ideas, and results presented in this document, except where explicitly acknowledged or properly cited, are original and created by me.

Student Signature: 

© University of Venda

University of Venda
Creating Future Leaders

Contents

1 Introduction **1**
1.1 Background . . . 1
1.2 Radio astronomy . . . 4
1.3 Radio Telescopes . . . 5
1.3.1 MeerKAT Radio Telescope . . . 5
1.4 Radio interferometry . . . 7
1.5 Interstellar Scintillation . . . 9
1.6 The MeerKAT Large Survey Projects . . . 10
1.7 Radio emission . . . 11
1.7.1 Coherent emission . . . 11
1.7.2 Incoherent emission . . . 12
1.8 Radio transients . . . 14
1.8.1 Various kinds of radio transients . . . 14
1.9 Aim and Objectives . . . 19

2 Transient Pipeline and Data processing **20**
2.1 Transients Pipeline . . . 20
2.1.1 Quality control . . . 23
2.1.2 Check for proximity to bright radio sources . . . 23
2.1.3 Source detection and measurement . . . 23
2.1.4 Source association . . . 24
2.1.5 Variability metrics . . . 24
2.2 Data . . . 28
2.3 The SARAO Science Data Processor (SDP) . . . 29
2.3.1 Imaging Process Overview . . . 29
2.3.2 Primary Beam Correction Process . . . 29
2.4 Flux errors due to calibration . . . 30
2.5 Ilifu and IDIA . . . 31
2.5.1 Visual inspection . . . 31

© University of Venda

University of Venda
Creating Future Leaders

2.6 Method . . . 32
2.7 Counterparts across different wavelengths . . . 34

3 Results for the NGC 5068 field **36**
3.1 Variability parameters η_ν and V_ν . . . 36
3.2 Light curves of variables sources . . . 43
3.3 Snapshots of variable sources identified in NGC 5068 . . . 44
3.4 Correlation of flux density and variability parameter η and V . . . 49
3.5 Counterparts across different wavelengths . . . 50
3.5.1 SRC74654 . . . 50
3.5.2 SRC75133 . . . 51
3.5.3 SRC73087 . . . 51
3.5.4 SRC73395 . . . 52
3.5.5 SRC74898 . . . 52
3.5.6 SRC74455 . . . 52
3.5.7 SRC75267 . . . 53
3.5.8 SRC73326 . . . 53
3.5.9 SRC73612 . . . 53
3.5.10 SRC75046 . . . 54
3.5.11 SRC72807 . . . 54
3.5.12 SRC74685 . . . 55

4 Results for the NGC 1566 field **58**
4.1 Variability parameters η_ν and V_ν . . . 58
4.2 Light curves of transient and variable sources . . . 62
4.3 Snapshots of variable sources identified in NGC 1566 . . . 63
4.4 Correlation of flux density and variability parameter η and V . . . 68
4.5 Counterparts across different wavelengths . . . 69
4.5.1 SRC79674 . . . 70
4.5.2 SRC77927 . . . 70
4.5.3 SRC78411 . . . 71
4.5.4 SRC79948 . . . 71
4.5.5 SRC76861 . . . 72
4.5.6 SRC79765 . . . 72
4.5.7 SRC77880 . . . 73
4.5.8 SRC79920 . . . 73
4.5.9 SRC79328 . . . 74
4.5.10 SRC79364 . . . 74
4.5.11 SRC76717 . . . 75

© University of Venda

University of Venda
Creating Future Leaders

5 Results for the NGC 1371 field **80**
5.1 Variability parameters η_ν and V_ν . . . 80
5.2 Light curves NGC 1371 . . . 84
5.3 Snapshots of variable sources identified in NGC 1371 . . . 86
5.4 Correlation of flux density and variability parameter η and V . . . 90
5.5 Counterparts across different wavelengths . . . 91
5.5.1 SRC68059 . . . 91
5.5.2 SRC69112 . . . 92
5.5.3 SRC67332 . . . 92
5.5.4 SRC68028 . . . 93
5.5.5 SRC68915 . . . 93
5.5.6 SRC66491 . . . 94
5.5.7 SRC66636 . . . 94
5.5.8 SRC67602 . . . 95
5.5.9 SRC69764 . . . 95

6 Conclusion **100**
6.1 Future work . . . 101

A NGC 5068 **110**

B NGC 1566 **113**

C NGC 1371 **116**

© University of Venda

University of Venda
Creating Future Leaders

List of Figures

1.1 Electromagnetic spectrum comparison of wavelength, frequency, and energy. Whereas radio waves have the longest wavelengths, gamma rays have the shortest. Frequency is inversely related to wavelength, meaning shorter wavelengths have higher frequencies. Energy is directly related to frequency, so higher-frequency radiation (like gamma rays) corresponds to higher energy. (Credit: NASA's Imagine the Universe, referred to the The Electromagnetic Spectrum). 3
1.2 MeerKAT radio telescope. (Credit: South African Radio Astronomy Observatory (SARAO), referred to MeerKAT radio telescope). 6
1.3 Two antennas (labelled A and B), separated by a distance D, both observing a plane wave (incoming radio signal) from a distant cosmic source at an angle θ, represent the time delay between antenna A and antenna B, this setup adapted from (Thompson et al., 2017). 7
1.4 The luminosity of various transient sources as a function of their width (W) and frequency (ν). The diagonal lines represent a constant brightness temperature. The brightness temperature of 10^{12} K distinguishes coherent emission mechanisms from incoherent ones, with incoherent emitters occupying the shaded lower-right region. The long-period sources shown in the box appear to cluster together, as indicated by the box. However, this box is only for visual emphasis and does not imply any physical significance (Caleb et al., 2024). 13

2.1 An overview of the Transients Pipeline, the flow of data as an image "cube" is processed, creating an archival light curve database and, if applicable, transient alert messages (Swinbank et al., 2015). 22
2.2 The distributions of the two variability parameters, η_ν and V_ν, are shown for all unique sources detected in the MAXI J1820+070 field across the four observing frequencies. The dashed black lines indicate the 1.5σ thresholds used to filter these parameters.(Rowlinson et al., 2022). 26
2.3 The Zooniverse workflow categorises four types of observations, each represented by a light curve and an image. This classification is adapted from (Andersson et al., 2023). 27

© University of Venda

University of Venda
Creating Future Leaders

2.4 The sample of images that passed visual inspection. The first panel on the top left shows an image from NGC 1371, the top right panel is from NGC 5068, and the bottom panel displays the image from NGC 1566. 32

3.1 Distribution of two variability metrics, V_ν and η_ν. The dashed purple lines show the 2σ thresholds used for filtering these parameters, the thresholds are $V_\nu = 0.22$ and $\eta_\nu = 171.41$. Different colours represent 12 variable sources, and black sources were not investigated. 37

3.2 Light curves of some selected green sources identified in Figure 3.1, corresponding to unique IDs 73107, 72639, 73052, 72434, 75427, and 72719. These light curves show no significant variability, suggesting that the sources remained stable throughout the observation period. In some light curves, the error bars were too small to be visible on the light curves. 39

3.3 The radio snapshot images of green sources identified in Figure 3.1 where in their corresponding light curves are shown in Figure 3.2. The first panel represents SRC72434; the middle panel corresponds to SRC72639; the bottom panel represents SRC72719. All the images are scaled to the same flux density range of -0.10 to 0.20 milliJansky (mJy) on a linear scale. The yellow circle in the lower-left corner of each image indicates the point spread function (PSF). Flux remains constant throughout the whole 10 epochs. 40

3.4 Snapshot of radio images of selected green sources from Figure 3.1, with their corresponding light curves shown in Figure 3.2. The first panel displays SRC73052, the middle panel shows SRC73107 and the last panel represents SRC75427. Every image has been linearly scaled to the same flux density range: (-0.10 to 0.20) mJy. The yellow circle in the lower-left corner shows each image's PSF. For the entire ten epochs, flux stays constant in each panel. 41

3.5 MeerKAT SDP image with source overlay of the field of NGC 5068. The sources marked in different shapes and colours denote 12 variable sources as listed in Table 3.1. 42

3.6 Light curves of variable sources located above the diagonal solid line in Figure 3.1, corresponding to unique IDs 73087, 74455, 74654, 74898, 75133, and 75267. In some light curves, flux density uncertainties are too small to be visible on the light curves. 43

3.7 Light curves of variable sources located above the diagonal solid line in Figure 3.1, corresponding to unique IDs: 72807, 73326, 73395, 73612, 74685 and 75046. In some light curves, flux density uncertainties are too small to be visible on the light curves. 44

© University of Venda

University of Venda
Creating Future Leaders

3.8 Radio image snapshots showing each source across ten observed epochs. The first panel represents SRC74654, with a flux density range of -0.10 to 0.20 mJy. The middle panel corresponds to SRC75133, with a flux density range of -0.10 to 0.30 mJy, while the bottom panel represents SRC73087, also within a flux density range of -0.1 to 0.4 mJy. The yellow circle in the lower-left corner of each image indicates PSF. Flux variations are observed across epochs. 45
3.9 Snapshots of radio images from ten observed epochs, each panel displays each source. SRC73395 is represented by the first panel, which has a flux density range of -0.1 to 0.5 mJy. SRC74898 is represented by the middle panel, which has a flux density range of -0.1 to 0.4 mJy. SRC74455 is represented by the bottom panel, which has a flux density range of -0.10 to 0.30 mJy. The yellow circle in the lower-left corner shows each image's PSF. There are differences in flux between epochs. 46
3.10 Radio images snapshots from ten epochs that display each source per panel. The first panel, which has a flux density range of -0.1 to 0.5 mJy, is for SRC75267. With a flux density range of -0.10 to 0.30 mJy, the middle panel represents SRC73326, while the bottom panel represents SRC73612, whose flux density range is -0.1 to 0.4 mJy. Each image displays the PSF as a yellow circle in the lower-left corner. Across epochs, flux fluctuations are seen. 47
3.11 Radio image snapshots from ten epochs, each displaying a different source per panel. The first panel represents SRC75046 with a flux density range of -0.10 to 0.30 mJy. The middle panel corresponds to SRC72807, with a flux density range of -0.1 to 0.4 mJy, while the bottom panel shows SRC74685, ranging from -0.10 to 0.20 mJy. The yellow circle in the lower-left corner of each image indicates the PSF. Flux variations are observed across epochs. 48
3.12 The correlation between the flux density and the variability parameters. The left panel shows η vs Flux (mJy), whereas the right panel shows V against flux (mJy). 49
3.13 The panel presents optical images from the Pan-STARRS catalogue for the selected sources. The first panel on the left represents SRC74654, while the right panel shows SRC75133. The middle panel contains SRC73087 (left) and SRC73395 (right), and the final panel displays SRC74898 (left) and SRC74455 (right). Each source is marked at its central position with a red cross. The images measure 1 arcminute by 45 arcseconds, with arrows in the bottom right corner indicating the sky direction, where "N" denotes North and "E" denotes East. 56

© University of Venda

University of Venda
Creating Future Leaders

3.14 The first panel presents optical images from the Pan-STARRS catalogue, with SRC75267 on the left and SRC73326 on the right. The middle panel displays SRC73612 (left) and SRC75046 (right), while the final panel shows SRC72807 (left) and SRC74685 (right). Each source is marked at its central position with a red cross. The images measure 1 arcminute by 45 arcseconds, with arrows in the bottom right corner indicating the sky's orientation, where "N" denotes North and "E" denotes East. 57

4.1 The variability parameters for all of the sources detected in the field NGC 1566, the different colours show the 10 variable sources and 1 transient marked by square which is cyan in colour for colour (see; Table 4.1). The black sources were not investigated. The dashed purple lines show the 2σ thresholds used for filtering these parameters, $\eta_\nu = 270.38$ for and $V_\nu = 0.28$. 59

4.2 MeerKAT SDP image of the field of NGC 1566. The sources marked in different shapes and colours denote variable sources as listed in Table 4.1. One source is marked with a cross to show visibility because it is on top of another source. . . 61

4.3 The light curves from TraP of variable sources identified in Figure 4.1, with unique IDs: 76717, 77880, 79328, 79364, 79674 and 97720. Uncertainty measurements are too small to be visible on some light curves. The flux is plotted in mJy along with the observation date in MJD. 62

4.4 The light curves from TraP of variable sources identified in Figure 4.1, with their corresponding Unique ID sources 76861, 77927, 78411, 79765 and 79948. Uncertainty measurements are too small to be visible on some light curves. The flux is plotted in mJy along with the observation date in MJD. The brightest source is SRC77927, has a peak flux of 1.7690 mJy. 63

4.5 Snapshots radio images showing the evolution of each source over the observed ten epochs: The first panel correspond to SRC79674 flux density in image range from -0.1 to 0.5 mJy, the middle panel to SRC77927 where in flux density in image range from -0.1 to 0.5 mJy and the bottom panel to SRC78411 its flux density in image range from -0.10 to 0.30 mJy. The PSF is indicated by the yellow circle in each image in the lower-left corner. 64

4.6 Snapshots of radio images showing the evolution of each source over the observed ten epochs: The first panel correspond to SRC79948 flux density in image range from -0.10 to 0.30 mJy, the middle panel to SRC76861 where in flux density in image range from -0.1 to 0.5 mJy and the bottom panel to SRC79765 its flux density in image range from -0.10 to 0.30 mJy. The PSF is indicated by the yellow circle in each image in the lower-left corner. The source can be seen varying in flux from epoch to epoch. 65

© University of Venda

University of Venda
Creating Future Leaders

4.7 Radio image snapshots illustrating each source across the ten observed epochs: The first panel represents SRC77880, the flux density of in the image range from -0.1 to 0.5 mJy, the middle panel represents SRC79920 in the flux density image range of -0.10 to 0.20 mJy, and the bottom panel represents SRC79328 with the flux density in image range of -0.10 to 0.20 mJy. The yellow circle in each image's lower-left corner represents the PSF. The source's flux varies between consecutive epochs. 66
4.8 Radio images snapshots that demonstrate how each source has changed across the ten epochs that have been observed: First panel: SRC79364, the bottom panel: SRC76717, both flux density in image range is between -0.10 and 0.20 mJy. Each image's yellow circle in the lower-left corner indicates the PSF. The flux of the source is observed to change from one epoch to the next. 67
4.9 The correlation between the flux density and the variability parameters. The left panel shows η vs Flux (mJy), whereas the right panel shows V against flux (mJy). 68
4.10 Radio versus optical flux density of objects from different classes, adapted from (Stewart et al., 2018), all my sources are represented by black colour with different symbols. Their positions relative to the diagonal dashed lines and survey limits can help identify their classes. 77
4.11 The first panel presents optical images from the Dark Energy Survey (DES), with SRC79674 on the left and SRC77927 on the right. The middle panel displays SRC78411 (left) and SRC79948 (right), while the final panel shows SRC76861 (left) and SRC79765 (right). Each source is marked at its central position with a red cross. The images measure 1 arcminute by 45 arcseconds, with arrows in the bottom right corner indicating the sky direction, where "N" denotes North and "E" denotes East. 78
4.12 The first panel presents optical images from the Dark Energy Survey (DES), with SRC77880 on the left and SRC79920 on the right. The middle panel displays SRC79328 (left) and SRC79364 (right), while the final panel represents SRC76717. Each source is marked at its central position with a red cross. The images measure 1 arcminute by 45 arcseconds, with arrows in the bottom right corner indicating the sky direction, where "N" denotes North and "E" denotes East. 79

5.1 The distribution of variability parameters for all sources detected in the NGC 1371 field. Different colours represent the nine variable sources, while black indicates sources that were not investigated. Green denotes sources whose radio images and light curves were visually inspected across ten epochs. The dashed purple lines mark the 2σ thresholds used for filtering these parameters, with $\eta_\nu = 804.04$ and $V_\nu = 0.4$. 81

© University of Venda

University of Venda
Creating Future Leaders

5.2 MeerKAT SDP image with sources overlayed of the field of NGC 1371. The sources marked in different shapes and colours denote 9 variable sources as listed in Table 5.1. 83
5.3 The light curves of variable sources identified in Figure 5.1, Each subplot corresponds to a different 9 variable source, identified by unique ID:66491, 66636, 76332, 67602, 68028, 68059, 68915, 69112 and 69764. Uncertainty measurements are too small to be visible on some light curves. The brightest source is 68059 with peak flux density 1.1332 mJy. 85
5.4 Radio image snapshots illustrating the evolution of each source over ten observed epochs. The first panel represents SRC68059, the middle panel shows SRC69112, and the bottom panel corresponds to SRC67332. All the images are scaled to the same flux density range of (-0.1 to 0.5) mJy on a linear scale. The yellow circle in the lower-left corner of each image marks the PSF. 87
5.5 Snapshots of radio images showing how each source has changed throughout ten observed epochs. SRC68028 is represented by the first panel, SRC68915 by the middle panel, and SRC66491 by the bottom panel. In the last panel, all the images are scaled to the same flux density range from -0.10 to 0.30 mJy, while in the first and second panels, all images are scaled to the same flux density range of (-0.1 to 0.5) mJy on a linear scale. The yellow circle in the lower-left corner indicates each image's PSF. 88
5.6 Snapshots of radio images illustrating the changes in each source over ten observed epochs. The first panel represents SRC66636, with all images scaled to a flux density range of -0.10 to 0.30 mJy. The middle panel corresponds to SRC67602, and the bottom panel corresponds to SRC69764, with the middle and last panels all images scaled to a flux density range of -0.10 to 0.20 mJy on a linear scale. The yellow circle in the lower-left corner of each image marks the PSF. 89
5.7 The correlation between the flux density and the variability parameters. The left panel shows η vs Flux (mJy), whereas the right panel shows V against flux (mJy). 90
5.8 Radio versus optical flux density of objects from different classes, adapted from (Stewart et al., 2018), all my sources are represented by black colour with different symbols. Their positions relative to the diagonal dashed lines and survey limits can help identify their classes. 97
5.9 The first panel presents optical images from the Dark Energy Survey (DES), with SRC68059 on the left and SRC69112 on the right. The middle panel shows SRC67332 (left) and SRC68028 (right), while the final panel shows SRC68915 (left) and SRC664915 (right). Each source is marked at its central position with a red cross. The images measure 1 arcminute by 45 arcseconds, with arrows in the bottom right corner indicating the sky's direction, where "N" denotes North and "E" denotes East. 98

© University of Venda

University of Venda
Creating Future Leaders

5.10 The first panel presents optical images from the Dark Energy Survey (DES), with SRC66636 on the left and SRC676027 on the right, while the final panel represents SRC69764. Each source is marked at its central position with a red cross. The images measure 1 arcminute by 45 arcseconds, with arrows in the bottom right corner indicating the sky direction, where "N" denotes North and "E" denotes East. 99

© University of Venda

University of Venda
Creating Future Leaders

List of Tables

2.1 Details of the observations for the NGC 1566, NGC 5068, and NGC 1371 galaxy fields in the MHONGOOSE Large Survey Project. 28
2.2 The parameters used within the TraP. 33

3.1 Characteristics of 12 variable sources identified in Figure 3.1, including their ID, position (RA and DEC), variability metrics, colour, and shape. 38
3.2 Summary of the characteristics of the 12 variable sources, including their Source ID, RA, DEC, variability indices η_ν and V_ν, and peak flux measurements with uncertainties, highlighting their variability and flux ranges. 50

4.1 Characteristics of variables and transient sources identified in Figure 4.1, including their ID, position (RA and DEC), variability metrics, colour, and shape. 60
4.2 Characteristics of 11 selected sources, including Source ID, RA, DEC, variability indices η_ν and V_ν, and observed flux values with uncertainties. The table provides an overview of the variability and flux range for each source. 69

5.1 Characteristics of the nine variable sources identified in the NGC 1371 field, including their ID, position (RA and DEC), variability metrics, colour, and shape. 82
5.2 Characteristics of 9 selected variable sources, including Source ID, RA, DEC, variability indices (η_ν and V_ν), and peak flux measurements with uncertainties, summarising their variability and flux ranges. 91

© University of Venda

University of Venda
Creating Future Leaders

Chapter 1

Introduction

1.1 Background

Astronomers study celestial objects and phenomena beyond the Earth's atmosphere (Condon & Ransom, 2016). One of the primary tools for this study is the electromagnetic spectrum, which encompasses all types of electromagnetic radiation, from gamma rays to radio waves. Different types of electromagnetic radiation provide unique insights into the universe, as various astrophysical processes emit energy at different wavelengths. The electromagnetic spectrum is divided into several ranges based on wavelength (λ) and frequency (ν) as shown in Figure 1.1. Gamma rays have the short wavelengths, while radio waves have the long wavelengths. As you move from gamma rays to radio waves, the wavelength increases by at least 12 orders of magnitude. The visible light spectrum, which includes colours from violet to red, is between ultraviolet (UV) and infrared light, with wavelengths shorter than infrared and longer than UV.

Frequency is inversely related to wavelength, i.e., ν=c/λ, where c is the speed of light. Energy (E) is directly related to frequency, i.e., $E = h \times \nu$, where h is the Planck constant. Therefore, higher frequency radiation (such as gamma rays) corresponds to higher energy. Gamma and X-rays are highly energetic due to their high frequency and short wavelengths, whereas radio waves associated with thermal processes have low energy due to their low frequency and long wavelength.

Gamma-ray radiation traces extremely energetic events like gamma-ray bursts, supernovae, and active galactic nuclei (AGN). Gamma rays reveal the most energetic and violent processes in the universe. They are often associated with the birth and death of stars and other high-energy phenomena. X-ray radiation, on the other hand, plays a crucial role in our understanding of high-temperature regions, such as the vicinity of black holes, neutron stars, supernova remnants, and hot gas in galaxy clusters. X-rays are crucial for studying phenomena like black hole accretion

© University of Venda

disks, the hot intergalactic medium, and the remnants of exploded stars. Ultraviolet radiation traces hot stars, young star-forming regions, and the interstellar medium. Very hot objects emit UV light and can reveal the properties of young, massive stars and the composition and behaviour of interstellar gas and dust.

As illustrated in Figure 1.1, the electromagnetic spectrum includes visible light, essential to observe stars, planets, galaxies, and other celestial bodies that emit or reflect light in this part of the spectrum. Visible light allows us to study these objects' structure, composition, and dynamics. Visible light is the most familiar part of the spectrum and the basis for classical astronomy. It allows astronomers to study the structure of stars and galaxies and their composition and dynamics. Infrared (IR) traces cool objects like dust clouds, star-forming regions, and planets. Infrared light penetrates dust clouds that block visible light, making it ideal for studying the formation of stars and planets and observing the universe's cooler parts. Microwave observes the cosmic microwave background (CMB), cold interstellar gas, and molecules in space. Microwaves provide information about the early universe through the study of the CMB (Herranz & Vielva, 2010), the afterglow of the Big Bang Theory. The Big Bang Theory is the leading explanation for the origin of the universe (Jones & Lasenby, 1998), describing a rapid expansion that started from an extremely hot, dense state about 13.8 billion years ago. Over time, the universe has cooled and expanded into what we observe today. It also helps to study molecular clouds, where new stars are born (Peebles et al., 1996).

Radio waves trace cold hydrogen gas, pulsars, radio galaxies, quasars, and the cosmic microwave background. Radio waves can penetrate dust clouds and are not blocked by Earth's atmosphere, allowing for continuous observation. Radio waves have long wavelengths, which enables them to penetrate through dust clouds in space that would otherwise obscure observations in other wavelengths like visible or infrared light. This means that astronomers can observe regions such as the centres of galaxies, star-forming regions, or areas shrouded in cosmic dust using radio telescopes, where optical telescopes would be blocked. Radio waves are not dependent on sunlight, which allows radio telescopes to observe the universe 24 hours a day, regardless of whether it is day or night at the observing location on Earth. Radio astronomy is ideal for monitoring long-term phenomena such as pulsars, variable stars, and CMB. Therefore, in radio observations, "continuous" refers to the ability to observe celestial objects and phenomena without significant interruptions. Radio astronomy has led to the discovery of many exotic objects and phenomena, including pulsars and the structure of galaxies. Karl Jansky is credited with founding the field of radio astronomy by discovering electromagnetic radiation of extraterrestrial origin in the radio spectrum (Jansky, 1958).

© University of Venda

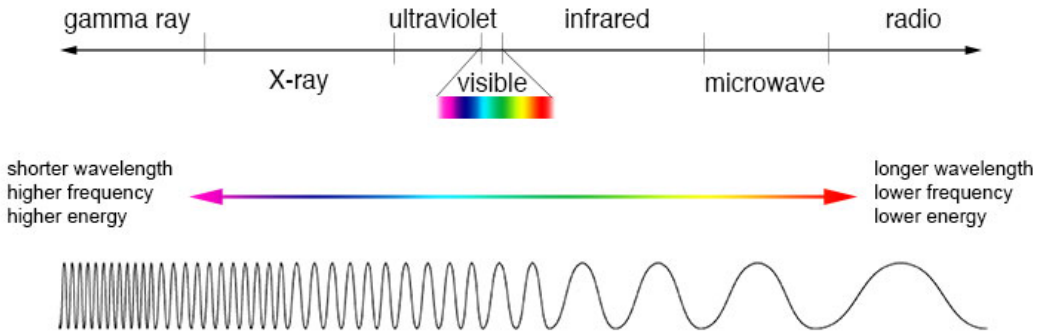


Figure 1.1: Electromagnetic spectrum comparison of wavelength, frequency, and energy. Whereas radio waves have the longest wavelengths, gamma rays have the shortest. Frequency is inversely related to wavelength, meaning shorter wavelengths have higher frequencies. Energy is directly related to frequency, so higher-frequency radiation (like gamma rays) corresponds to higher energy. (Credit: NASA's Imagine the Universe, referred to the The Electromagnetic Spectrum).

Astronomers often use data from multiple parts of the electromagnetic spectrum to get a complete picture of an astronomical object. For example, a galaxy can be studied in radio waves to understand its cold gas content, in infrared to see star formation regions, in visible light to study its stars, and in X-rays to observe energetic phenomena like black holes. Each type of electromagnetic radiation provides different information. For instance, the study of supernova remnants typically employs a multi-wavelength approach: X-rays are used to detect the hot gas produced by the explosion, visible light is used to trace the expanding shock wave, and radio waves help map the distribution of cold gas and cosmic rays. A prominent example is the supernova remnants SN 1987A, where X-ray, optical, and radio observations have been crucial in tracing the remnant's evolution (McCray & Fransson, 2016). In this thesis, we use electromagnetic radio waves emitted by the most extreme astrophysical phenomena in the universe. This introduction offers the background needed to comprehend the subsequent chapters of the thesis.

Advances in modern radio telescopes have significantly improved instantaneous sensitivity across wide fields of view, enabling the detection of much fainter signals. As a result, contemporary radio surveys are uncovering a richer and more diverse view of the universe, largely populated by star-forming galaxies and the often overlooked radio-quiet active galactic nuclei (AGN) (Padovani, 2016). A dominant source of radio emission in both AGN and star-forming galaxies is synchrotron radiation—non-thermal emission produced by relativistic electrons spiraling in magnetic fields. In AGN, this radiation is powered by highly energetic jets from supermassive black holes, while in star-forming galaxies, including the Milky Way, it dominates the radio continuum below $\nu \sim 30\,\mathrm{GHz}$ (Condon & Ransom, 2016). Synchrotron radiation also spans a broad spectral range, from the optical emission of the Crab Nebula supernova remnant (Hester, 2008) to the

*https://images.app.goo.gl/Tb2Fa9xNKukcYz8W7

© University of Venda

optical and X-ray emissions of many quasars (Blandford & Königl, 1979), and is often associated with shock waves of varying velocities—from relativistic shocks in AGN, gamma-ray bursts, and microquasars to slower flows in supernova remnants (Cécere et al., 2016). Jets, which form through the accretion of material in rotating systems, play a pivotal role in astrophysical environments. They are key to studying star formation, as they emerge from dense, obscured regions and are detectable via their distinct kinematic signatures (Mohan et al., 2022). These jets range from ultra-relativistic in high-energy phenomena (Blandford et al., 2019) to non-relativistic in protostars (Lee et al., 2007) and brown dwarfs (Palau et al., 2014), helping to regulate accretion by removing excess angular momentum (Blandford & Payne, 1982).

1.2 Radio astronomy

Karl Jansky is acknowledged as the pioneer of radio astronomy for his groundbreaking discovery of electromagnetic radiation of extraterrestrial origin within the radio spectrum (Orchiston & Sullivan, 2005). While working at Bell Laboratories in the early 1930s, Karl Jansky discovered electromagnetic waves from outer space using a rotatable antenna system. This discovery, initially presented in 1933 (Jansky, 1958), demonstrated that radio waves from outer space were reaching Earth, thus opening a new avenue for astronomical observations beyond the visible spectrum. His groundbreaking work, completed in December 1932, identified radio waves coming from the centre of our galaxy (the Milky Way galaxy), opening up a new field of astronomy. The significance of Jansky's discovery, which allowed scientists to study celestial objects through radio waves, greatly expanded the observable electromagnetic spectrum. This groundbreaking discovery marked the birth of radio astronomy (Reich & Wielebinski, 2002).

Radio astronomy is a field of astronomy that examines celestial objects by detecting and analysing the radio waves they emit (Westerhout, 1953). Unlike optical astronomy, which observes light in the visible spectrum, radio astronomy focuses on the electromagnetic spectrum's radio frequency range, which spans from 3 kHz to 300 GHz. However, most astronomical observations are conducted above 30 MHz due to ionospheric interference at lower frequencies. Radio waves are electromagnetic radiation, like visible light, but with much longer wavelengths. Objects that emit radio waves include pulsars, discovered in 1967 by Jocelyn Bell Burnell (Bell Burnell, 2017); pulsars are highly magnetised, rotating neutron stars that emit beams of electromagnetic radiation (Young, 2011). Other well-known objects observed at radio wavelengths are quasars. Radio astronomy has been crucial in discovering and studying quasars, which are incredibly luminous active galactic nuclei (AGN) powered by supermassive black holes (Rees, 1978).

© University of Venda

1.3 Radio Telescopes

Radio telescopes are large parabolic antennas that collect radio waves from space. They focus the incoming waves onto receivers, which then amplify the signals for analysis. The Very Large Array (VLA) is among the most famous radio telescopes (Perley et al., 2009). In recent years, radio astronomy has expanded with the construction of new, more sensitive radio telescopes such as MeerkAT, ASKAP, LOFAR and the MWA, the precursors to the Square Kilometre Array (SKA) (Labate et al., 2022), which aims to be the world's largest radio telescope when completed. Radio astronomers often use arrays of radio telescopes working together in a technique called interferometry to increase resolution. The angular resolution of a radio telescope increases as the baseline increases. The next generation of radio telescopes often have a wide field of view, allowing them to scan large portions of the sky simultaneously. The dimension of a "large portion of the sky" depends on the specific radio telescope and its field of view (FoV). For MeerKAT, the field of view (FoV) depends on the observing frequency. At 1.4 GHz, the primary beam has a full width at half maximum (FWHM) of approximately 1 degree (Jonas, 2018). This section will briefly outline one of the radio telescopes (MeerKAT) and introduce the critical surveys conducted with them, as these surveys are crucial for studying transient phenomena.

1.3.1 MeerKAT Radio Telescope

MeerKAT is a radio telescope array located in the Northern Cape of South Africa. The name "MeerKAT" is an acronym derived from Meer ("more" in Afrikaans) and KAT, which stands for Karoo Array Telescope (Camilo, 2018). The telescope is part of the larger Square Kilometre Array (SKA) project, an international effort to build the world's largest and most sensitive radio telescope, which is planned to be one of the most powerful radio telescope arrays in the world (Jonas, 2018). The site was chosen for its low population density, minimal radio frequency interference, and the ability to conduct radio observations with low background noise. The construction of MeerKAT began in 2012 and became operational in July 2018. Figure 1.2 shows the MeerKAT radio telescope.

© University of Venda



Figure 1.2: MeerKAT radio telescope. (Credit: South African Radio Astronomy Observatory (SARAO), referred to MeerKAT radio telescope).

MeerKAT operates in the frequency range of 580 MHz to 4 GHz, covering a wide spectrum in the radio frequency domain, using three different receivers: UHF band (0.58 GHz - 1.015 GHz), L band (0.9 GHz - 1.67 GHz), and S-band (1.75 GHz - 3.5 GHz) (Jonas, 2018). MeerKAT is designed to address a range of scientific questions, including the study of neutral hydrogen in distant galaxies, the formation and evolution of galaxies, and the detection of radio pulsars and transient events (de Blok et al., 2018).

The MeerKAT telescope delivers high-quality, wide-field images with rapid survey capabilities, allowing for in-depth exploration of the radio transient sky across various timescales, from just a few seconds to several years. This capability allows for unbiased surveys of the radio sky, leading to the discovery of transient and variable sources that may have been missed by targeted searches at other observing frequencies (Rowlinson et al., 2022). ThunderKAT is a project dedicated to image-plane radio transients on MeerKAT (Fender et al., 2017) and is described more in Section 1.6 of this introduction. The primary goal of ThunderKAT, established in 2010 and continuing today, focused on discovering, identifying, and studying high-energy astrophysical processes by analysing their radio emissions, often complemented by observations across multiple wavelengths.

*https://www.sarao.ac.za/gallery/meerkat/#2018

© University of Venda

1.4 Radio interferometry

Interferometry significantly enhances the resolution of radio telescopes by combining signals from multiple antennas. A brief overview of radio interferometry is provided here. This technique in radio astronomy combines signals from multiple antennas to simulate a larger antenna, significantly improving both resolution and sensitivity. The angular resolution (θ) can be represented mathematically as:

$$\theta \approx \frac{\lambda}{D}, \tag{1.1}$$

where λ is the observing wavelength, D is the diameter of the telescope in meter (m) and θ resolution in radians.

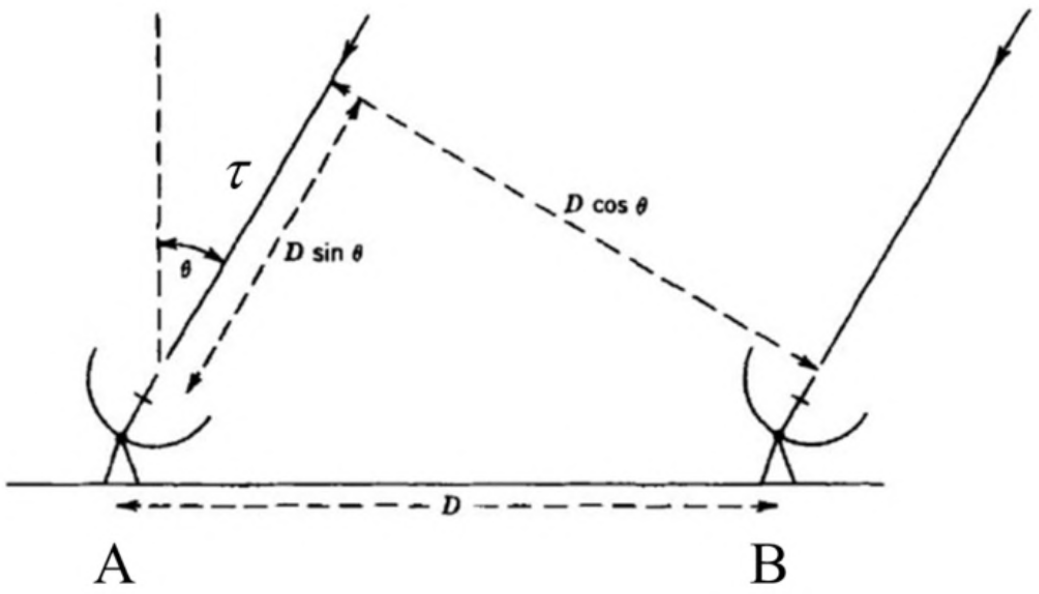


Figure 1.3: Two antennas (labelled A and B), separated by a distance D, both observing a plane wave (incoming radio signal) from a distant cosmic source at an angle θ, represent the time delay between antenna A and antenna B, this setup adapted from (Thompson et al., 2017).

As mentioned, radio interferometry combines signals from multiple antennas to achieve the following: (a) High resolution: Angular resolution depends on the maximum baseline (distance between antennas). MeerKAT's 8 km maximum baseline provides a resolution equivalent to a 17 km dish. (b) Sensitivity: Total collecting area determines faint-source detection. MeerKAT is the largest and most sensitive radio telescope in the southern hemisphere, with 64 dish-shaped

© University of Venda

individual antennas, each with a diameter of 13.5 m. The process involves radio interferometry: (a) Signal capture: Each dish observes the same cosmic source simultaneously. (b) Correlation: A central processor combines signals pairwise, measuring time delays from geometric path differences and interference patterns (fringes). (c) Earth rotation synthesis: As Earth rotates, baseline orientations change, filling gaps in spatial frequency coverage.

Now, with radio interferometry, instead of building one massive dish, we simulate a giant aperture by using many smaller dishes spread over a large distance. The interferometer's resolution depends on the largest distance between two antennas, which is the maximum baseline, so from Equation 1.1 we replace D with $B_{\max}$ the resolution formula becomes:

$$\theta \approx \frac{\lambda}{B_{\max}}, \tag{1.2}$$

When two antennas observe a source, they produce fringes (interference patterns), and the fringe spacing tells us about the resolution. Smaller fringe spacing equals higher resolution, and that happens when the baseline is longer. As you add more antennas and baselines and let the Earth rotate (filling the uv-plane), you effectively simulate a giant aperture. In single-dish, a resolution is given by Equation 1.1 and in interferometry, we don't have one big dish, but we synthesize a big one by using the baseline D instead, it becomes Equation 1.2, So from Figure 1.3 the baseline D is the physical distance between the two antennas.

Figure 1.3 shows a basic setup where two antennas are placed in an east-west direction. They are separated by a distance D, called the baseline, and both observe the same cosmic source (Thompson et al., 2017). The incoming wave reaches antenna B before it reaches antenna A is called the geometric delay. The path difference between the signals at A and B is $\Delta L = D \sin\theta$, where ΔL is the path difference. This path difference causes a geometric time delay given by:

$$\tau_g = \frac{\Delta L}{c} = \frac{D \sin\theta}{c}, \tag{1.3}$$

where τ_g is the geometric time delay and c is the speed of light. The time delay introduces a phase difference between the received signals, which is measured by the correlator in the interferometer. The geometric time delay arises because a wavefront arriving from a source at angle θ travels a longer path to reach one antenna compared to the other. This causes the signal at one antenna to lag behind the other by a time τ_g, which translates to a phase shift in the received signal.

The phase difference (ϕ) introduced by a geometric time delay τ_g between two antennas is given by the relationship

$$\phi = \omega\tau = 2\pi\nu\tau, \tag{1.4}$$

where ω is the angular frequency and ν is the frequency of the observed radio signal. This phase difference arises because the signal reaches one antenna slightly earlier than the other, due to

© University of Venda

the physical separation between them and the angle of incidence of the incoming wave. The correlator in the interferometer measures this phase shift, which encodes information about the direction and structure of the radio source. Accurate knowledge of τ_g , and hence ϕ, is essential for aligning signals correctly and recovering meaningful visibility data. Substituting Equation 1.3 into the phase expression, the phase difference becomes:

$$\phi = \frac{2\pi D \sin\theta}{\lambda}, \tag{1.5}$$

where $\lambda = \frac{c}{\nu}$ is the wavelength of the signal, with c representing the speed of light and ν the frequency of the observed radio wave. The correlator multiplies the two antenna signals and averages them over time. It is sensitive to this phase difference ϕ, and this is how it determines the visibility (complex correlation) between the antennas. The correlator effectively measures how in-phase or out-of-phase the signals are due to the geometric delay, which is directly controlled by the baseline, the angle, and the wavelength.

1.5 Interstellar Scintillation

Scintillation describes the variations in observed flux densities of radio sources. This is caused by scattering in our galaxy's ionized interstellar medium (ISM). It's analogous to the twinkling of stars or radio waves caused by the turbulent ISM. Stars appear to twinkle because their light passes through Earth's atmosphere, where turbulence causes fluctuations in brightness and position (Habibi et al., 2013). Rapid Interstellar Scintillation (ISS) has been observed in the quasar PKS 1257-326. This quasar exhibits large and rapid intra-hour variations in its received flux density at centimetre wavelengths due to scattering in the local Galactic ISM (Bignall & Hodgson, 2011). Radio variable and transient sources typically indicate extreme astrophysical environments, which may include intense magnetic activities, explosions, accretion processes, and extrinsic propagation effects caused by inhomogeneities in the ionized interstellar medium (ISM) (Murphy et al., 2013). Radio waves can travel through dust and gas without obstruction, making radio observations a valuable tool for accurately detecting events like core-collapse supernovae, tidal disruption flares, and potentially Type Ia supernovae. In addition to intrinsic variability, external factors can also influence these observations (Driessen et al., 2022).

Refractive and diffractive effects lead to scintillation as the signal passes through clumpy and turbulent intervening material, which causes variations in electron density on different length scales. These delays in the signal can result in destructive or constructive interference when the waves recombine (Stinebring et al., 1996). Refractive interstellar scintillation occurs due to electrons along the line of sight, with the timescale and variability amplitude being affected by the Galactic latitude of the AGN (Hancock et al., 2019). AGNs display variability across the electromagnetic spectrum, often exhibiting flares in their flux density curves. Studying these variations across different AGN types provides insight into the physical mechanisms driving

© University of Venda

these events. In particular, AGN flares can occur over timescales ranging from days to months, primarily due to shocks in the jets formed as material accretes onto the central supermassive black hole (Hovatta et al., 2008).

1.6 The MeerKAT Large Survey Projects

As highlighted in (Woudt et al., 2018), ThunderKAT also has memoranda of understanding with many other large survey projects on MeerKAT. The Hunt for Dynamic and Explosive Radio Transients with MeerKAT (ThunderKAT) is the image-plane transients program for the MeerKAT telescope. Its primary objective was first established in 2010. Its goal is to discover, identify, and study high-energy astrophysical processes through their radio emissions, often in conjunction with observations across other wavelengths (Woudt et al., 2018). ThunderKAT aims to explore a wide range of astrophysical phenomena, including supernovae, gamma-ray bursts, and X-ray binaries, by monitoring changes in the radio sky. The survey seeks to understand the mechanisms behind radio transients, contributing to our knowledge of high-energy astrophysical processes and the lifecycle of stars.

One of the significant discoveries associated with this survey is the detection of a unique neutron star, PSR J0901-4046, with an ultra-long spin period of 76 seconds (Caleb et al., 2022). This discovery was made possible through a collaboration between ThunderKAT and the More Transients and Pulsars (MeerTRAP) project dedicated to identifying and studying transient radio sources. The neutron star in question exhibits characteristics of both pulsars and magnetars, with its radio emission being detectable only 0.5% of its rotation period. This implies that many similar, slowly spinning sources might exist undetected in our galaxy. The discovery provides new insights into the evolution of neutron stars and their magnetic properties, suggesting a possible connection to ultra-long period magnetars and fast radio bursts.

Other MeerKAT Large Survey Projects are Looking at the Distant Universe with the MeerKAT Array (LADUMA; Holwerda et al. 2011), The MeerKAT International GHz Tuned Extragalactic Exploration Survey (MIGHTEE; Jarvis et al. 2018), and MeerKAT HI Observations of Nearby Galactic Objects: Observing Southern Emitters (MHONGOOSE; de Blok et al. 2018). For a comprehensive list of all the projects for MeerKAT, refer to Jonas (2018). This study will focus mainly on the MHONGOOSE Large Survey Projects (LSP); MHONGOOSE is among the LSPs involved in searching for transients. It offers 6 to 8 pointings per deep field, making it an excellent tool for detecting faint extragalactic transients from weeks to months.

© University of Venda

1.7 Radio emission

Radio emission is the release of energy in the form of radio waves, a type of electromagnetic radiation with wavelengths longer than infrared light and frequencies spanning approximately 3 kHz to 300 GHz, at frequencies lower than 3 kHz, electromagnetic waves transition from the radio spectrum to the Extremely Low Frequency (ELF) and Very Low Frequency (VLF) bands, which are below the standard radio range (Barr, 1998). These emissions can originate from various natural and artificial sources on Earth and in space (Guedel, 2002).

The continuum radio emission from the Milky Way is primarily produced by two physical mechanisms. The first is thermal (free-free) emission, which originates from the interactions of thermal electrons within ionised gas. The second is synchrotron emission, generated when high-energy electrons spiral around magnetic field lines in the Galaxy, emitting radiation as they accelerate a form of so-called "braking radiation" (Large, 1963).

The emission processes at radio wavelengths are mostly non-thermal. These are typically divided into two subcategories: incoherent and coherent emission mechanisms. The distinction between them is often reflected in the brightness temperature of the emitting object. This quantity is quite intuitive for (optically thick) thermal emission mechanisms, where the brightness temperature is equal to the temperature of the emitting body. Sections 1.7.1 and 1.7.2 explain incoherent and coherent emission mechanisms, the associated radio transients, and the methods used to study them.

1.7.1 Coherent emission

The coherent sources, often referred to as "fast transients", have played a crucial role in astrophysical discoveries. Typically, these events occur on short timescales of about a few seconds or less. Coherent emission is not restricted by the maximum brightness temperature, allowing easy detection on much shorter timescales. The brightness temperature of synchrotron emission is constrained to $T_B \leq 10^{12}$K due to energy losses from inverse Compton scattering (Kellermann & Pauliny-Toth, 1969). If an observed source exceeds T_B, a coherent radiation mechanism is likely responsible (Güdel, 2002). The brightness temperature is then defined as follows:

$$T_B = \frac{c^2}{2k_B\nu^2} I_\nu, \tag{1.6}$$

where T_B = Brightness temperature (K), c = Speed of light (3.0×10^8 m·s^{-1}), k_B = Boltzmann constant (1.38×10^{-23} J·K^{-1}), ν = Observing frequency (Hz), I_ν = Specific intensity (W·m^{-2}·Hz^{-1}·sr^{-1}) (Tsang & Kirk, 2007).

Coherent radio emission, with its much higher brightness temperature than incoherent synchrotron emission, has been instrumental in demonstrating the existence of neutron stars. Ex-

© University of Venda

amples of associated transients include Pulsars and fast radio bursts (FRBs). Radio pulsars' very high brightness temperature at 10^{24}–10^{31} K implies that the emission is coherent (Cordes, 1979). FRBs are ultrafast radio transients that typically last milliseconds. A huge brightness temperature is a characteristic property of FRBs (Ghisellini & Locatelli, 2018).

1.7.2 Incoherent emission

The incoherent sources, often called "slow" transients, play a significant role in various astrophysical events. On time scales longer than a second, incoherent radio transients are suggested to exist and emit via synchrotron radiation(Condon & Ransom, 2016). All explosive events in astrophysics are related to incoherent synchrotron emission caused by particle acceleration and ambient magnetic field compression due to ejections at a velocity faster than the sound speed in the area. These occurrences vary in intensity, from star flares with moderate luminosity to the strongest events in the universe linked to relativistic jets from supermassive black holes in active galactic nuclei and gamma-ray bursts, the collapse of a massive star to a black hole (Woosley, 1993).

Both general considerations (Metzger et al., 2015) and empirical evidence (Pietka et al., 2015) demonstrate that when incoherent synchrotron radiation is emitted, the brightness temperature is constrained, resulting in longer characteristic timescales (days/years) for the more luminous transient events. These highly luminous events can be detected at great distances (and, therefore, have high volumetric rates). Common examples of incoherent radio astronomy emissions include synchrotron radiation, produced by relativistic electrons spiralling around magnetic field lines. This is common in jets from AGN and supernova remnants (Zheleznyakov et al., 2000). Associated transients are Supernovae, AGN flares, and gamma-ray bursts (GRBs), as they involve energetic particle acceleration that produces synchrotron radiation.

Incoherent synchrotron events are linked to nearly all forms of explosive kinetic feedback and particle acceleration in the Universe, ranging from relativistic jets to supernova explosions. In a steady state, their emission is constrained by a brightness temperature limit of $T_B \leq 10^{12}$ K. The most luminous events, which can be observed at cosmological distances, exhibit slow variations over timescales that typically span days to years. This duration often exceeds that of standard observations, so variability is commonly assessed by comparing images taken at different epochs (Fender et al., 2015). Figure 1.4 illustrates various categories of transient sources based on classifications adopted from the research conducted by (Caleb et al., 2024). For a more comprehensive discussion of these transient sources, refer to (Pietka et al., 2015), where different groups are examined in greater detail.

© University of Venda

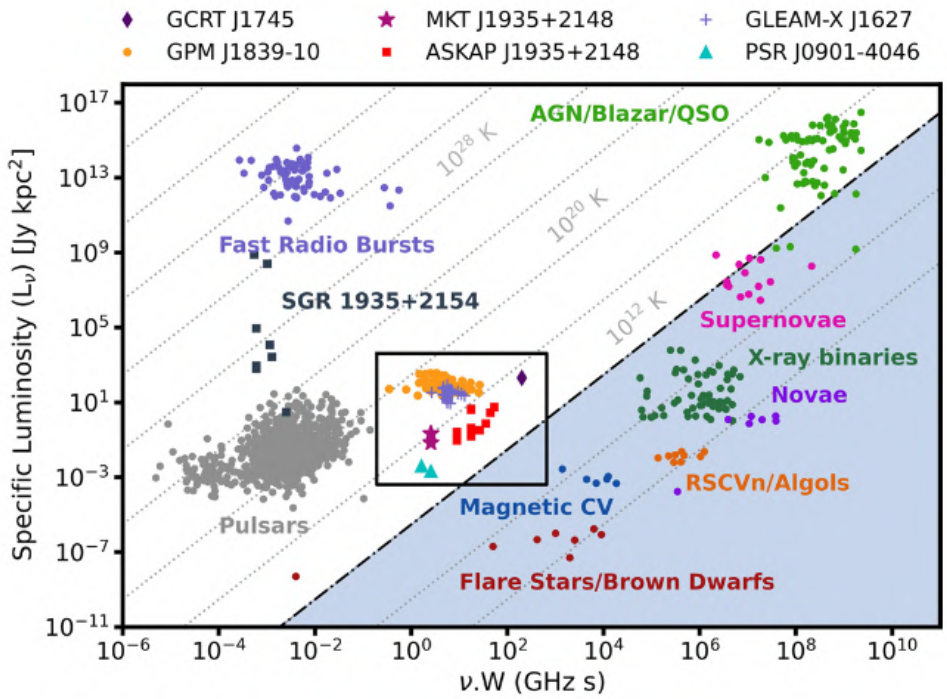


Figure 1.4: The luminosity of various transient sources as a function of their width (W) and frequency (ν). The diagonal lines represent a constant brightness temperature. The brightness temperature of 10^{12} K distinguishes coherent emission mechanisms from incoherent ones, with incoherent emitters occupying the shaded lower-right region. The long-period sources shown in the box appear to cluster together, as indicated by the box. However, this box is only for visual emphasis and does not imply any physical significance (Caleb et al., 2024).

Figure 1.4 shows the radio transient phase space. This phase space illustrates the luminosity of various transient phenomena as a function of the product of the transient duration and observing frequency. The dashed diagonal lines represent lines of constant brightness temperature. Above a brightness temperature of 10^{12} K, the background of Figure 1.4 is white, as these transients are all produced by coherent emission processes. The exceptions to this rule of thumb are the active galactic nuclei (AGN) and gamma-ray bursts (GRBs) in the top right of Figure 1.4. As the derivation that yields the 10^{12} K limit does not include relativistic effects, Doppler boosting can push the apparent brightness temperature of these intrinsically incoherent processes above the 10^{12} K limit. This occurs when emission regions are moving at relativistic speeds. Both transients are investigated in the image plane observations with various integration timescales and in the time domain with high time resolution (milliseconds or less) (Driessen et al., 2020). Star and stellar system flares are one kind of radio transient that is anticipated to be discovered during image plane transient searches (see, e.g. (Osten et al., 2016) for a summary).

Coherent and incoherent emission mechanisms refer to fundamentally different physical processes

© University of Venda

by which electromagnetic radiation is generated. Incoherent emission arises from large populations of particles radiating independently, for example, synchrotron emission from relativistic electrons spiral around magnetic field lines (Benford & Tzach, 2000). This type of emission is common in many astrophysical sources such as supernova remnants and active galactic nuclei (AGN). Coherent emission, in contrast, involves particles radiating in phase. Three known examples of coherent emission in radio astronomical sources are: plasma emission, electron cyclotron maser emission (ECME) and pulsar radio emission (Melrose, 2017).

1.8 Radio transients

Radio transients are events that are not constant but change significantly in brightness or appear/disappear entirely (Driessen, 2020). Radio transients serve as markers for astrophysical occurrences that are explosive and highly energetic, making transient surveys an essential tool for studying the dynamic universe. There is growing interest among researchers in searching for transient sources in the radio sky due to the development of increasingly sensitive radio telescopes with excellent UV- and sky-coverage, such as MeerKAT (Camilo, 2018) the Australian SKA Precursor (ASKAP; Johnston & et al 2007) and the future Square Kilometer Array (SKA; Hoare et al. 2015). When fully operational, the SKA will be one of the most powerful radio telescopes ever constructed, potentially revolutionising our understanding of the transient universe. So far, many types of transient sources have been discovered, varying on timescales from milliseconds to years. The development of advanced radio telescopes and interferometric arrays made possible by technological improvements has allowed astronomers to perform sensitive and high-resolution studies. Nevertheless, utilising radio imaging to conduct commensal transient surveys may require substantial processing power, data storage, and time (Fijma et al., 2024).

Longer-duration transients, lasting from hours to decades, such as fading supernovae, typically emit incoherent radiation from thermal electrons. In contrast, short-duration transients, occurring on timescales of seconds or less, must be coherent in nature, as their emission is too intense to be explained by individual electrons radiating independently. While variable sources exhibit periodic brightening and fading, often superimposed on a stable flux, transients are usually singular events that diminish once the emission mechanism ceases. Both fast and slow transients are powered by some of the most energetic processes in the Universe (Petroff et al., 2019). This section will outline different kinds of radio transients.

1.8.1 Various kinds of radio transients

1. Fast Radio Bursts (FRBs).

   According to Driessen et al. (2024), FRBs are short, bright, coherent radio transients that last for milliseconds. Most FRBs appear as one-off events, though some have been observed

© University of Venda

to repeat. Their transient nature and brief duration make it difficult to localise non-repeating FRBs precisely within a few arcseconds. The first detections of FRBs "Lorimer burst" (also known as FRB 010724; Lorimer et al. 2007) were made in surveys for radio pulsars, rapidly rotating neutron stars that emit beams of radio emission from the open magnetic field lines at their magnetic poles.

Observationally, FRB sources are classified into two categories: (apparently) no repeating (which appear to emit only a single burst) or repeating sources (which have been observed to emit multiple bursts) (Yamasaki et al., 2024). On average, repeater bursts are observed to be longer in duration and narrower in bandwidth than bursts seen from non-repeating sources (Pleunis et al., 2021). It is unclear if this observed difference represents an intrinsic difference in the two populations or if it is caused by a propagation effect related to distinct source environments. Niu et al. (2022) reported the detection and localization of the repeating FRB 20190520B, which is co-located with a compact, persistent radio source and associated with a dwarf host galaxy exhibiting a high specific star formation rate. Similarly, Chime/Frb Collaboration et al. (2023) presented the discovery of 25 new repeating fast radio burst (FRB) sources identified among CHIME/FRB events detected between 30 September 2019 and 1 May 2021. In contrast, Bhandari et al. (2023) reported the discovery of the apparently non-repeating FRB 20210117A using the Australian Square Kilometre Array Pathfinder (ASKAP), which was also localized to a dwarf galaxy.

2. Pulsars.

   Radio pulsars are rotation-powered neutron stars that emit coherent radio beams produced by highly relativistic particles in regions above their magnetic poles. Their spin periods (P) range from milliseconds to tens of seconds. Their radio emission is expected to fade as they age and slow down. Pulsars are categorised into various sub-classes, such as rotating radio transients (RRATs; Caleb et al. 2022). Normal radio pulsars emit radio waves along magnetic field lines near their magnetic poles. As the pulsar rotates, these beams sweep across our line of sight, allowing radio telescopes to detect them as periodic pulses (Mikhailov & van Leeuwen, 2016). Since the first radio pulsar was discovered in 1968 (Hewish et al., 1968), advancements in high-time-resolution astronomical observations have expanded our ability to study a wide variety of astrophysical phenomena, now collectively referred to as radio transients (Bezuidenhout et al., 2023).

   One notable discovery was the ultra-long-period radio-emitting neutron star PSR J0901–4046, which exhibits spin properties distinct from those of known spin-powered and magnetic-decay-powered neutron stars. This neutron star has an exceptionally long spin period of 75.88 seconds (Caleb et al., 2022).

3. Gamma-Ray Bursts (GRBs).

© University of Venda

GRBs are intense flashes of gamma rays originating from cosmic sources. They occur approximately once per day and typically last less than a minute, representing some of the most powerful explosive events in the Universe (Gehrels & Mészáros, 2012). GRBs were first discovered in the late 1960s by the Vela satellites, which were monitoring compliance with the Nuclear Test Ban Treaty between the United States and the Soviet Union (Klebesadel et al., 1973). A major breakthrough in understanding GRBs, particularly their distances, energy scales, environments (Berger, 2014), and progenitors—came with the discovery of afterglows from long GRBs in 1997 (Costa et al., 1997). The distribution of GRB durations shows two distinct peaks: one around 0.3 seconds and another near 30 seconds, with a trough at approximately 2 seconds. GRBs are categorized based on this duration—those lasting less than 2 seconds are classified as short GRBs, while those exceeding 2 seconds are termed long GRBs. Recent observations have confirmed that long GRBs can result from the collapse of massive stars, where the core collapses into a compact object such as a black hole (MacFadyen & Woosley, 1999). Additionally, at least some short GRBs originate from the mergers of compact binary systems, such as two neutron stars or a neutron star and a black hole (Kumar & Zhang, 2015).

4. Active Galactic Nuclei (AGN).

   AGN are powerful astrophysical sources that are driven by accretion onto supermassive black holes in galaxies (Padovani et al., 2017). They are known to exhibit flux variability throughout the electromagnetic spectrum and on all observable timeframes (Ricci & Trakhtenbrot, 2023). By examining the variability differences among various types of AGN, we gain insights into the underlying physics that drives these events (Hovatta et al., 2008). The established AGN paradigm involves a central supermassive black hole surrounded by an accretion disk, or more broadly, optically thick plasma, which emits intensely in the UV and possibly soft X-ray wavelengths. In certain systems, highly relativistic outflows of energetic particles along the poles of a rotating black hole, accretion disk, or torus generate collimated radio-emitting jets, which produce extended radio sources. These AGNs are referred to as radio-loud due to their relatively strong radio emission. In contrast, AGN lacking such collimated jets—resulting in weaker, though still detectable, radio emission—are known as radio-quiet (Ulrich et al., 1997).

   AGNs are known for their high temporal flux variability, which can provide important details about their complicated accretion and plasma outflow physical processes (Park & Trippe, 2017). Several studies have shown that different types of AGNs, from Seyfert galaxies (Lawrence et al., 1987) to quasars (Kelly et al., 2009) and radio-bright AGNs (Hovatta et al., 2007), exhibit widespread aperiodic variability across multiple wavebands. AGNs possess a variety of intriguing properties. These include: (1) They exhibit very high luminosities (up to $L_{\rm bol} \approx 10^{48}\,{\rm erg\,s^{-1}}$), making them the most powerful non-explosive sources in the Universe, and thus visible at extremely high redshifts (Padovani et al., 2017);

© University of Venda

(2) They have small emitting regions in most bands, typically on the order of a milliparsec, as indicated by their rapid variability, which suggests high energy densities(Ulrich et al., 1997); (3) They exhibit a strong evolution in their luminosity functions, reflecting significant changes in their brightness over cosmic time (Merloni & Heinz, 2013); (4) The detectable emission across the entire electromagnetic spectrum which means that AGNs are being discovered in all spectral bands, from radio to gamma rays.

5. Supernovae.

   When a massive star ($\geq 8\,M_{\odot}$) reaches the end of its life, it may undergo a core-collapse supernova (CCSN) explosion. Recent studies suggest that not all massive stars explode; particularly those with initial masses above $30\,M_{\odot}$ may instead collapse directly into black holes, resulting in so-called failed CCSNe (Wirth et al., 2024). Supernovae are strong explosions from big stars that have reached the end of their life cycle. During the explosion, a huge amount of energy is released in various wavelengths (Dallal & Azzam, 2021). In a typical burst, the radiation emitted by a supernova can outshine the entire galaxy in which it resides over a brief period. The first historical record of a supernova dates back to 185 CE, as observed and documented by the Chinese (Zhao et al., 2006). Since then, several supernovae have been observed in our galaxy, with the most luminous being SN 1006, which occurred in the southern constellation Lupus (Stephenson, 2010). Since the 1940s, it has become evident that there is a wide variety of supernova (SN) types (for an overview, see; da Silva 1993). The first type, known as a Type I supernova, is of thermonuclear origin and is distinguished by the absence of hydrogen lines in its spectrum. The second category, Type II supernova, is characterised by the presence of strong hydrogen lines in its spectrum (Dallal & Azzam, 2021).

   The modern study of supernovae encompasses various aspects, including their use as distance indicators, as well as other potentially observable phenomena such as neutrino bursts, gravitational waves, and the emissions resulting from a white dwarf collapsing directly into a neutron star (Woosley & Weaver, 1986). Supernovae play a crucial role in the dynamical and morphological evolution of the Universe. As primary sources of the elements that constitute existence, they are key agents in both stellar and galactic evolution (Burrows, 2000). Most supernova explosions mark the death of a massive star, resulting in the formation of neutron stars and black holes, while also ejecting solar masses of heavy elements into the surrounding environment (Burrows & Vartanyan, 2021).

6. Stellar transient.

   Stellar radio sources encompass a variety of phenomena, including thermal and non-thermal magnetic coronae, transition regions, and chromospheres. They also include stars shedding winds, colliding-wind binaries, pre-main sequence stars with disks and radio jets, as well as embedded young objects that are primarily visible through their radio and millimetre-

© University of Venda

wave emission (Güdel, 2002). Additionally, a prominent group of thermal or non-thermal sources just above the main sequence includes various classes of pre-main sequence stars, such as classical and weak-lined T Tauri stars. Pre-main sequence (PMS) stars and, more broadly, young stellar objects (YSOs) form a diverse group of stellar radio sources. Significant progress has been made in understanding these objects since the last "Radio Stars" Conference (Andre, 1996). Since the launch of the EINSTEIN mission in 1978, it has been established that young stellar objects (YSOs) are strong emitters of X-rays (Glassgold et al., 2005).

Flare stars are a subset of active stars, constituting a significant portion of the stellar population. Stellar flares are the radiation emitted during a magnetic reconnection event (Benz & Güdel, 2010). The primary products of these flares, high-energy electrons and ions, can be spatially resolved in hard X-rays (HXRs) and gamma rays, as seen on the Sun. Soft X-rays (SXRs) are also observed from most stars, including young stellar objects. Stars generate energetic bursts of electromagnetic radiation due to a sudden release of magnetic energy into their atmospheres. These bursts, known as flares, can occur over a wide range of timescales, from just seconds to several days. (Kowalski, 2024). For a comprehensive review of stellar flaring activity across the Hertzsprung-Russell diagram and its characteristics, see (Pettersen, 1989).

© University of Venda

1.9 Aim and Objectives

The main aim of this study is to conduct a commensal search for astrophysical variables and transients in the wide field of view of the MeerKAT observations using MeerKAT data from the MHONGOOSE MeerKAT large survey project (de Blok et al., 2018) concentrated on the fields of NGC1566, NGC 5068 and NGC 1371, over 10 epochs per field. The study aims to characterise the transient and variable radio skies on times scales of days to months, at previously unexplored sensitivity limits. Specific objectives of the study:

1. Discover new radio variables and transients through commensal searches in MHONGOOSE data.
2. Move from archival transient searches towards discovery in "real-time" as new MeerKAT fields are observed (search for new objects in very recent data).
3. Characterise the transient and variable radio sources on a time scale of days to months.
4. Optimise the commensal transient search strategy based on the standard SARAO SDP (science data processing) images.

This search aims to be as inclusive as possible by targeting both incoherent and coherent radio emissions, thereby identifying a wide range of transient phenomena regardless of their emission mechanisms. It is designed to be blind and untargeted, scanning the entire field of view in each image cube for variability rather than focusing solely on known sources. The term "archival" refers to searches in already available historical data that has been calibrated and stored. In contrast, "real-time" is used aspirationally to describe a shift toward low-latency analysis-detecting variability in new data within days of its release from the Science Data Processor (SDP), rather than waiting years. The chosen time scales, spanning from days to months, are driven by the natural cadence of the MHONGOOSE observations, which typically include about ten epochs per field.

The MHONGOOSE survey, while originally designed to study the distribution and kinematics of neutral hydrogen (HI) in nearby galaxies (de Blok et al., 2018), provides data that are exceptionally well-suited for radio transient and variability studies. This suitability has been explicitly recognised by the ThunderKAT project (Woudt et al., 2018), the image-plane transient programme of MeerKAT. ThunderKAT incorporates a commensal search strategy that actively targets transient and variable phenomena using data from other MeerKAT Large Survey Projects (LSPs), including MHONGOOSE. Specifically, the ThunderKAT team outlined the following goals for their MHONGOOSE-based transient survey: This LSP will provide 6 - 8 pointings per deep field, providing an excellent resource to look for faint (extragalactic) transients over time scales of weeks to months (Woudt et al., 2018).

© University of Venda

University of Venda
Creating Future Leaders

Chapter 2

Transient Pipeline and Data processing

This chapter provides an overview of the Transients Pipeline, outlining its key concepts and the various stages of processing images. Showing how the Transient Pipeline works provides the necessary context to understand each stage of the process. This will offer a comprehensive understanding of how the pipeline operates and its role in handling the scientific data from the MeerKAT radio telescope. It also includes a detailed description of the SARAO Science Data Processor (SDP) images, focusing on how it handles primary beam correction of images. Additionally, the data used in this study will be outlined, and the method will be explained here following previous studies conducted by other researchers.

2.1 Transients Pipeline

The Transients Pipeline detects sources above a user-defined threshold in a set of astronomical images, generating light curves for each unique source and calculating statistics for each one (Andersson et al., 2023). There are two ways in which these sources can be identified. Firstly, sources that were not previously observed appear at a location in recent observations. This is because no source was observed in that location during previous observations. Secondly, sources observed in multiple epochs and exhibiting significant variations in their light curves are known as variables (Swinbank et al., 2015). Figure 2.1 illustrates an overview of the Transients Pipeline. The methods and stages involved, as described in this figure, will be detailed in the following sections.

1. The main memory stores the image cube as a sequence of two-dimensional images, each corresponding to a specific frequency. The TraP utilises an in-memory image representation that is independent of the disk's data storage format.

© University of Venda

2. An evaluation process is applied to every image to determine its quality. This process aims to filter out data that falls below the acceptable quality standards so that it is not used for further analysis. It's important to note that any data rejected by the quality control process is still documented, along with the reason for its rejection.

3. The image cube is independently subjected to source-finding and measurement on each plane. Elliptical Gaussians are used to parameterise sources that meet significant criteria.

4. A procedure called "association" is performed, wherein the latest measurements are categorised as updates to the light curves of known sources or as new sources that were previously undetected.

5. A new list is created, containing sources that are supposed to be present in the image but weren't detected by the previous source-finding process. The identified sources' parameters are fitted and recorded using the same source measurement code at each fixed position, and the corresponding light curves are updated accordingly.

6. The code used for measuring the source remains constant and is utilised for fitting and documenting the source parameters at each of the monitoring positions specified by the user. The corresponding light curves are then adjusted accordingly based on the updated parameters.

7. The aggregate properties of each astronomical source are determined from its light curve in the database. These properties include a weighted mean position, flux density, and variability indices, which measure the magnitude and significance of the light curve's variability.

© University of Venda

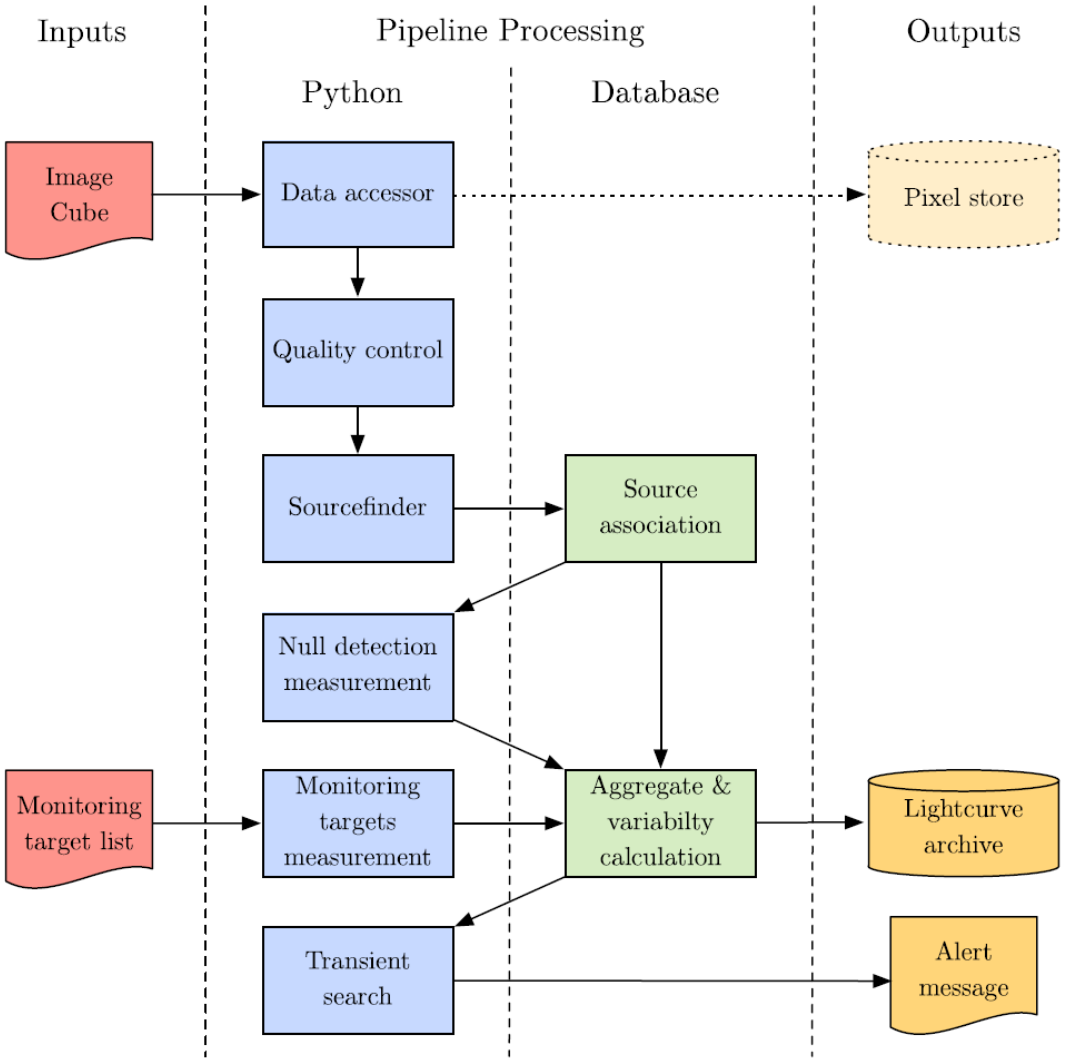


Figure 2.1: An overview of the Transients Pipeline, the flow of data as an image "cube" is processed, creating an archival light curve database and, if applicable, transient alert messages (Swinbank et al., 2015).

© University of Venda

Sections 2.1.1 to 2.1.5 provide an overview of the Transients Pipeline logical arrangement, highlighting the key phases of the pipeline, along with the algorithms utilised by each stage.

2.1.1 Quality control

During both the imaging process and the real-time imaging pipeline, the Transients Pipeline expects to generate excessive images for processing. Some of these images may not meet the required standards for effective transient searches due to high radio frequency interference (RFI) or poor calibration solutions, resulting in images filled with noise or artefacts that could be incorrectly identified as transients. To tackle this problem, a quality control procedure is implemented to identify and reject images that do not meet specific criteria through a series of tests. If an image is of low quality, it can be easily identified by analysing the noise level. When the measured noise level significantly differs from the expected value, it indicates issues with the observation or its calibration. Values that are either too low or too high can indicate issues with the observation or calibration (van Haarlem et al., 2013). In addition, assessing the image quality within the TraP involves considering the properties of the restoring beam used to create the images. With around three pixels across its minor axis, proper beam sampling is crucial to achieve an appropriately sampled image. Failure to sample the beam correctly can increase noise and artefacts (Swinbank et al., 2015).

2.1.2 Check for proximity to bright radio sources

Luminous objects near the target are not accurately subtracted during the "demising" process (van der Tol et al., 2007), which can lead to residual structures or increased noise in the final images. This issue is typically observed near the Sun and Jupiter (de Bruyn et al., 2009). To mitigate these effects, the Transients Pipeline excludes images with smaller angular separation between the target field and a bright source than a user-defined threshold.

2.1.3 Source detection and measurement

The Transients Pipeline employs its own source detection and measurement system, known as “source finder” which was custom developed. While some of its algorithms are based on those used in SExtractor software (Bertin & Arnouts, 1996), they have been significantly reworked and expanded. One notable enhancement is the ability to perform least-squares fitting of detected sources with elliptical Gaussians. Additionally, the Transients Pipeline system offers a thorough approach to handling the correlated noise properties of radio images. Radio images contain complex background and noise characteristics. The noise in the image is correlated across it due to the nature of the imaging process. It is necessary to identify pixels above the RMS noise to detect the source, which requires careful modelling of the background and noise maps (Swinbank et al., 2015). The first step is to divide the image into a rectangular grid whose dimensions are specified by the user. The grid cell dimensions should be significantly larger than the extended

© University of Venda

sources visible in the image but fine enough to trace background variations. The next step is to estimate the background and RMS in each grid cell through iterative clipping around the median to reject source pixels. While performing this task, it is crucial not to bias the result by rejecting source-free pixels and to consider the noise correlation scale.

2.1.4 Source association

A unique identification is assigned to each astronomical source identified within a specific set of images through an entry in the "running catalogue". This catalogue is utilised to merge information about the source obtained from individual image measurements, including its position, variability details, and more, connecting a sequence of measurements conducted in individual images. Its light curve is comprised of the complete set of measurements associated with a particular running catalogue entry. Additional information on various types of associations is provided in (Swinbank et al., 2015). The detection of a source that was expected to be seen in an image based on its appearance in previous images of the same area, where it had a higher flux density than the detection threshold for the current image, is referred to as "null detection". After the association process (Section 4.4 of Swinbank et al. 2015, generate a list of sources that fulfil the following requirements:

1. Exists in the running catalogue of known sources; it has been previously observed in any frequency band.

2. Has not identified any source linked to the current image.

For each entry in the running catalogue, at least one individual measurement corresponds to the current image. Other measurements may also correspond to images that likely represent observations at different times or frequencies.

2.1.5 Variability metrics

After associating the sources, each entry in the running catalogue corresponds to a multi-frequency light curve representing a specific source. The properties of these light curves can be examined to identify transient and variable sources. For every source, the flux density is measured at a specific frequency, labelled ν, with an uncertainty of σ_v. Using these values, the flux density is defined as the coefficient of variation over N measurements, which is the ratio of the mean flux density to the sample standard deviation s. The variability statistic parameter (V_ν) is then defined as follows:

$$V_\nu = \frac{s}{\overline{I_\nu}} = \frac{1}{\overline{I_\nu}} \sqrt{\frac{N}{N-1}\left(\overline{I_\nu^2} - \overline{I_\nu}^2\right)}, \tag{2.1}$$

The meaning of weight $w_\nu = \frac{1}{{\sigma_\nu}^2}$, the importance of the flux density variability can also be expressed. Making use of the familiar reduced-χ^2 expression in conjunction with the weighted

© University of Venda

mean flux density, ξ_{I_ν}. The expression for (η_ν) is then defined as follows:

$$\eta_\nu = \frac{1}{N-1}\sum_{i=1}^{N}\frac{(I_{\nu,i}-\xi_{I_\nu})^2}{\sigma^2_{\nu,i}}. \tag{2.2}$$

V_ν and η_ν are computed and saved for each light curve whenever a new measurement is added for the source (Swinbank et al., 2015). V_ν and η_ν can be used to determine the statistical significance and the amplitude of variation, respectively. It is expected that η_ν will correlate with average flux density, and the brightest sources will have the smallest statistical uncertainties. Variability metrics allow for tracking changes in a source's variability characteristics over time, as they are saved for each association. This is especially helpful for sources that have demonstrated behavioural evolution over time.

The Transients Pipeline (TraP) calculates a key variability parameter called the reduced weighted χ^2, which is obtained by fitting a constant brightness. This parameter measures the variability of sources based on their flux density measurements across different epochs and observing frequencies. To determine the relative variability of the source's flux density, the coefficient of variation V_ν is calculated as the ratio of the standard deviation of the flux density measurements (s) to the average flux density of the source $\bar{I}$. An example is illustrated in Figure 2.2 where the Gaussian distribution was used to model the distribution of stable sources, considering outliers as candidate variable sources. Variable candidates were sources that showed more significant variability than the 1.5σ offset from the (η_ν and V_ν) distributions (Rowlinson et al., 2022). Criteria based on the 1.5σ thresholds determined for each observing frequency were used to identify variable sources. To characterise these sources, the plot of η_ν against V_ν was plotted to show the distribution of sources indicating how the data looks in terms of population refer to Figure 2.2. For this research 2σ was used for either V_ν or η_ν and variable candidates were sources that showed more significant variability than the 2σ offset from the (η_ν and V_ν).

The variability of the candidate sources was verified by visual inspection and comparison with nearby sources. This involved confirming the variability of sources based on their variability parameters and their behaviour across different observing epochs. Radio images and light curves were visually inspected to identify potential variable or transient sources. Figure 2.3 provides examples of various classifications (Andersson et al., 2023). Stable sources are unresolved point sources whose light curves are considered flat within uncertainties. The Extended Blob classification is designed to identify resolved, extended sources regardless of their variability. Variability not inherent to the source can be introduced by changes in the point spread function (PSF) size and angle between epochs, so any subject deemed resolved is classified as an Extended Blob—using the local sky figure to compare the source size to the PSF shown in the lower left corner. The Artefact classification identifies spurious, non-astrophysical sources that may appear in our images. The Transient or Variable classifications, on the other hand, focus on the sources

© University of Venda

we are specifically searching for—point sources characterized by variable light curves.(Andersson et al., 2023).

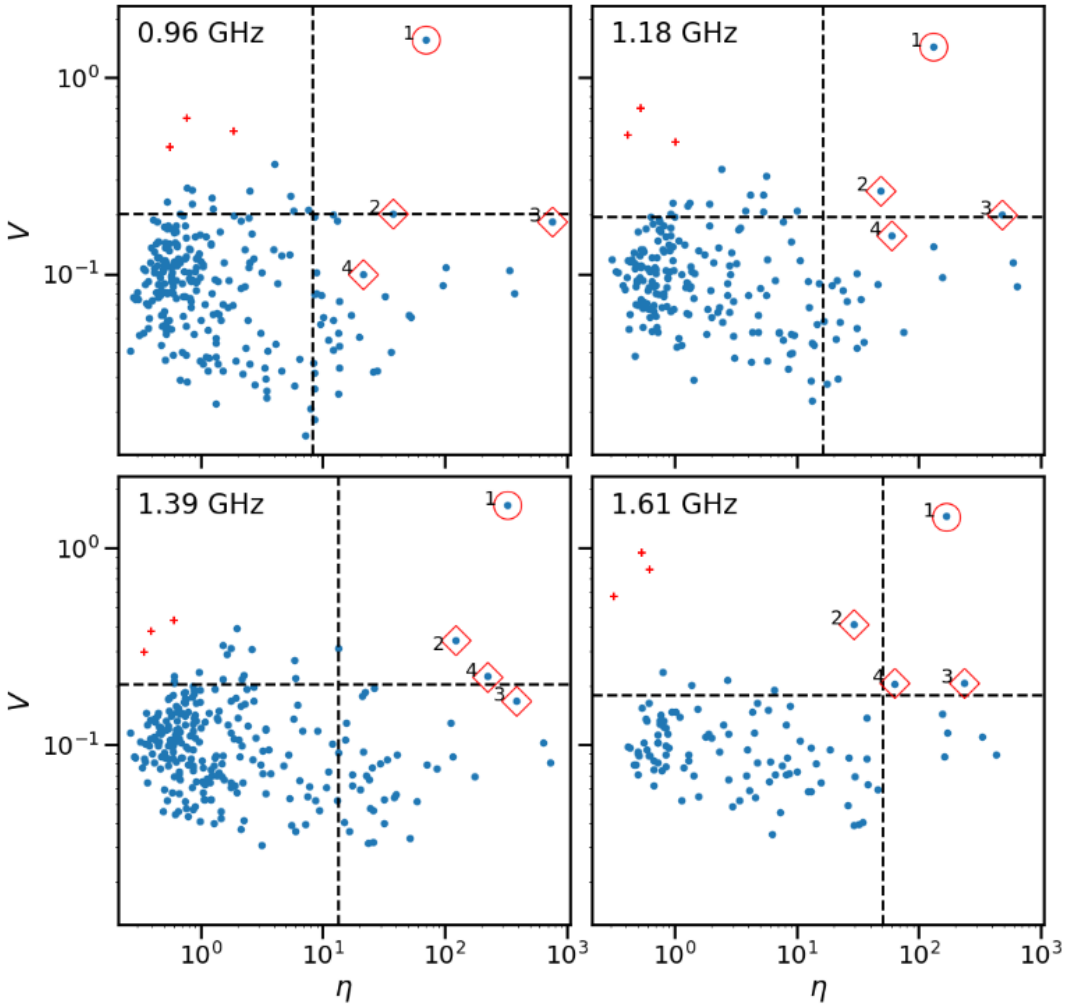


Figure 2.2: The distributions of the two variability parameters, η_ν and V_ν, are shown for all unique sources detected in the MAXI J1820+070 field across the four observing frequencies. The dashed black lines indicate the 1.5σ thresholds used to filter these parameters.(Rowlinson et al., 2022).

Figure 2.2 shows four variable sources identified in the MAXI J1820+070 field. The XRB MAXI J1820+070 is highlighted with a red circle, while the remaining three variable sources are marked with red squares. These variable candidates are listed in the lower part of (Table 5; Rowlinson et al. 2022), along with their variability parameters at each observing frequency. All four sources are associated with previously known objects, and variability is confirmed by visual inspection and comparison to nearby sources. The red plus symbols indicate variable candidates identified

© University of Venda

in the transient search presented in Section 3.1 of Rowlinson et al. (2022).

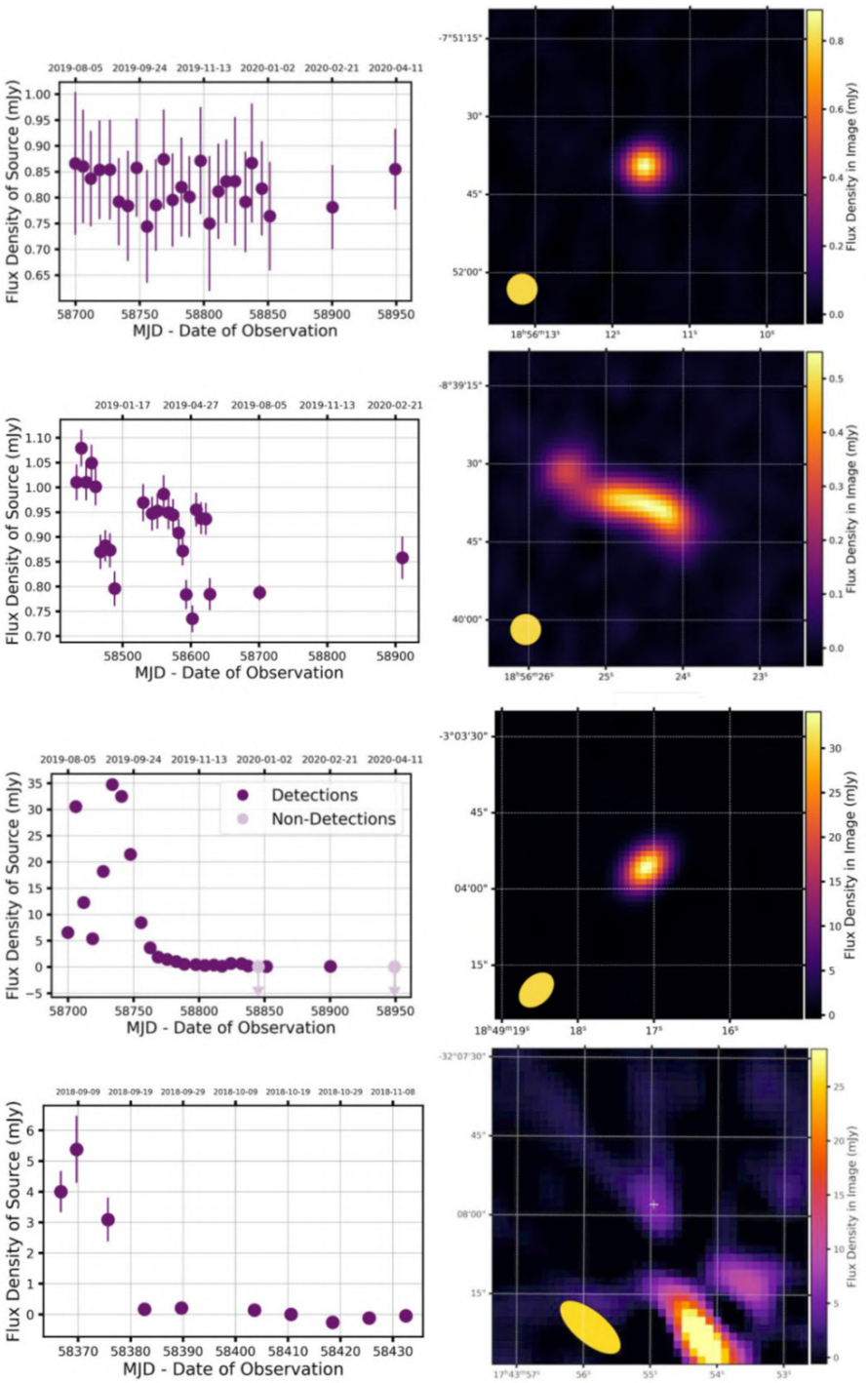


Figure 2.3: The Zooniverse workflow categorises four types of observations, each represented by a light curve and an image. This classification is adapted from (Andersson et al., 2023).

© University of Venda

2.2 Data

The data used in this study were collected as part of the MeerKAT HI Observations of Nearby Galactic Objects – Observing Southern Emitters (MHONGOOSE; de Blok et al. 2018), a MeerKAT Large Survey Project aimed at conducting a deep survey of the neutral hydrogen distribution in a sample of 30 nearby galaxies. All of these galaxies are located within 30 Mpc, meaning that the MeerKAT L-band beam would provide a spatial resolution of 1 kpc at the distance of the target galaxies. MHONGOOSE was awarded a total observation time of 1650 hours, equally divided among 30 galaxies, or 55 hours per galaxy. Each galaxy is further divided into 10 tracks of 5.5 hours (de Blok et al., 2024). My study aims to use images produced from the MHONGOOSE survey to search for radio transient and variable sources spanning time scales from one month to over 1 year. Specifically, this search was conducted on three galaxy fields: NGC 1566, NGC 5068 and NGC 1371. These fields were selected primarily based on data availability and completeness at the time of the study.

The study utilised the 4K continuum SDP images, which were automatically generated by the data pipeline of the SARAO. SDP images are generally used for quality assurance and are not subject to robust calibrations; full details on SDP are discussed in Section 2.3. However, the advantage is that they are available immediately after the observation is concluded, potentially allowing for the discovery of image-domain transients in near-to-real time. In this project, we are testing the use of SDP images for transient detection and benchmarking them against transient searches in the calibrated continuum images from the MHONGOOSE project, derived from the simultaneous narrow-band continuum data. Many studies have proven that these images can be used for science, as demonstrated in several papers in the MeerKAT ADS library. Two of the "radio transient" studies demonstrating the use of SDP images for transient searches were conducted by master's students from the University of Cape Town (Moses Mlangeni, 2024; "The discovery and characterization of astrophysical transients with MeerKAT" and the University of Amsterdam (Nathan Peters, 2023).

Table 2.1: Details of the observations for the NGC 1566, NGC 5068, and NGC 1371 galaxy fields in the MHONGOOSE Large Survey Project.

Parameters	**NGC 5068**	**NGC 1566**	**NGC 1371**
No. of images	10	10	10
Date of observation	03/04/2021 - 13/03/2022	21/10/2020 - 2/11/2020	31/07/2022 - 09/01/2023
No. of images rejected	0	0	0
Frequency (GHz)	1.2839	1.2839	1.2839
Image size (Pixels)	6136	6136	6136
Diameter in degrees	1.999	1.999	1.999

© University of Venda

2.3 The SARAO Science Data Processor (SDP)

This section provides a brief overview of SDP pipelines*. The pipeline is designed to facilitate real-time data processing directly from the correlator. As a result, once the data is processed, it cannot be reprocessed using different settings. The primary goal of these pipelines is to generate Quality Assessment (QA) metrics that provide insights into the reliability and accuracy of the observational data. This is crucial for ensuring that the scientific community can trust the data products generated for further research and analysis. The pipelines include advanced imaging capabilities, such as a spectral imager that produces FITS images for each channel in observations. The design emphasises speed and efficiency, allowing for the rapid production of images from extensive observational data.

2.3.1 Imaging Process Overview

The SDP receives visibility data directly from the MeerKAT correlator in real time. This data is then processed through various pipelines that run sequentially to produce different data products, including images. The SDP supports both continuum and spectral imaging. Continuum imaging has been operational since November 2019, while spectral imaging began in January 2020. The spectral imager produces single-channel FITS images for each channel in the observation, capable of handling up to 32,000 channels, provided that the observations meet specific criteria (e.g., duration and calibration requirements). The imaging pipeline utilises a hybrid approach combining W-stacking and W-projection techniques for gridding and de-gridding, which are essential for reconstructing the sky brightness distribution from the visibility data.

The design prioritises imaging speed, enabling the production of a significant number of images within a short timeframe (e.g., 32,000 images from an 8-hour observation in approximately 5 hours). The imaging process incorporates calibration solutions derived from the continuum pipeline, which are applied to ensure accuracy. Primary beam correction is performed using a simple spherical model to account for the antenna's response across the field of view. The final output includes data products such as primary beam-corrected images, spectral images, and quality assessment reports. These products are crucial for researchers to evaluate the quality and characteristics of the observed data.

2.3.2 Primary Beam Correction Process

The SARAO Science Data Processor (SDP) handles primary beam correction using a straightforward approach that employs a simple spherical model. This correction is crucial for ensuring that the images from visibility data accurately reflect the true brightness distribution of astronomical sources. The SDP utilises a spherical model to represent the primary beam of the MeerKAT

*https://skaafrica.atlassian.net/wiki/spaces/ESDKB/pages/338723406/SDP+pipelines+overview

© University of Venda

telescope. This model accounts for how the telescope's antennas respond to incoming signals from different directions in the sky. The primary beam correction is applied during the imaging process. Specifically, the SDP divides the raw continuum image by the primary beam attenuation pattern. This step effectively corrects for the variations in sensitivity across the field of view, which can lead to distortions and inaccuracies in the final image if left uncorrected. The correction process is integrated into the imaging pipelines of the SDP. Primary beam correction has been operational since mid-April 2020 as part of the continuum imaging. This ensures that the images produced reflect the actual flux density of sources, mitigating potential imaging artefacts caused by an incorrect primary beam model. Currently, the SDP does not perform any merging post-imaging channels. Each image is produced as an individual FITS file, allowing users to access primary beam-corrected images directly from the archive without additional processing steps. The SDP also generates quality assessment metrics alongside the corrected images. These metrics help users to evaluate the quality of the observations and the effectiveness of the primary beam correction applied.

2.4 Flux errors due to calibration

The SARAO SDP performs automated calibration, and the resulting flux density uncertainties are not explicitly propagated in the final image products. However, several measures within the pipeline aim to minimize calibration-related flux errors and ensure reliable flux density measurements:

1. The SDP relies on observations of well-established primary calibrators (e.g., PKS B1934–638) to set the absolute flux scale. These calibrators have well-known flux density models that help anchor the flux scale to a physically meaningful reference.

2. After calibration and imaging, the SDP generates a range of QA metrics, such as calibration solution stability (gain amplitudes/phases over time), Signal-to-noise ratio of calibrators, Image noise levels, Beam characteristics. These are reviewed to determine whether the calibration was successful and whether the flux scale is trustworthy.

3. To correct for spatially dependent sensitivity, the pipeline applies a primary beam model to the images. This ensures that flux densities across the field are not biased due to antenna response falloff, though the model is simplified and may not capture all frequency-dependent effects.

4. Flux calibration uncertainties are typically on the order of $\sim$ 5–10%, depending on the quality of the calibrator observations and stability of the gain solutions.

Although the SDP pipeline does not explicitly provide flux uncertainties for each image, errors due to calibration are minimised through regular calibrator observations and are estimated to

© University of Venda

be at the level of $\sim$ 5–10%. Any claimed variability in flux density must exceed this threshold to be considered significant (Mauch et al., 2020).

2.5 Ilifu and IDIA

Ilifu cloud computing resource ilifu, which is a collaboration between the Cape Peninsula University of Technology, Stellenbosch University, Sol Plaatje University, the University of Cape Town, and the University of the Western Cape. Contributions to the ilifu facility come from the Data Intensive Research Initiative of South Africa (DIRISA), the Computational Biology division at UCT, and the Inter-University Institute for Data Intensive Astronomy (IDIA). IDIA is a partnership of academic institutions aimed at developing tools, infrastructure, and expertise for data-intensive astronomy. It provides access to the computational environment needed to work with massive datasets and supports the development of software like CARTA.

2.5.1 Visual inspection

This study utilised the Cube Analysis and Rendering Tool for Astronomy (CARTA; Comrie et al. 2021), a visualisation tool designed for inspecting and analysing astronomical images and spectral data cubes. Manual inspection of images using CARTA on the ilifu computing cluster played a key role in refining image quality before running the Transients Pipeline (Trap) on the Ilifu computing cluster for transient and variability analysis. A total of 10 images of the fields of NGC 1566, NGC 5068, and NGC 1371 were visually inspected in CARTA using a 99.5% linear scale to enhance visibility. All images passed the quality check and are suitable for scientific analysis. Examples of the validated sampled images are shown in Figure 2.4. The primary beam was corrected for NGC 1371 and NGC 5068 by the MeerKAT team.

© University of Venda

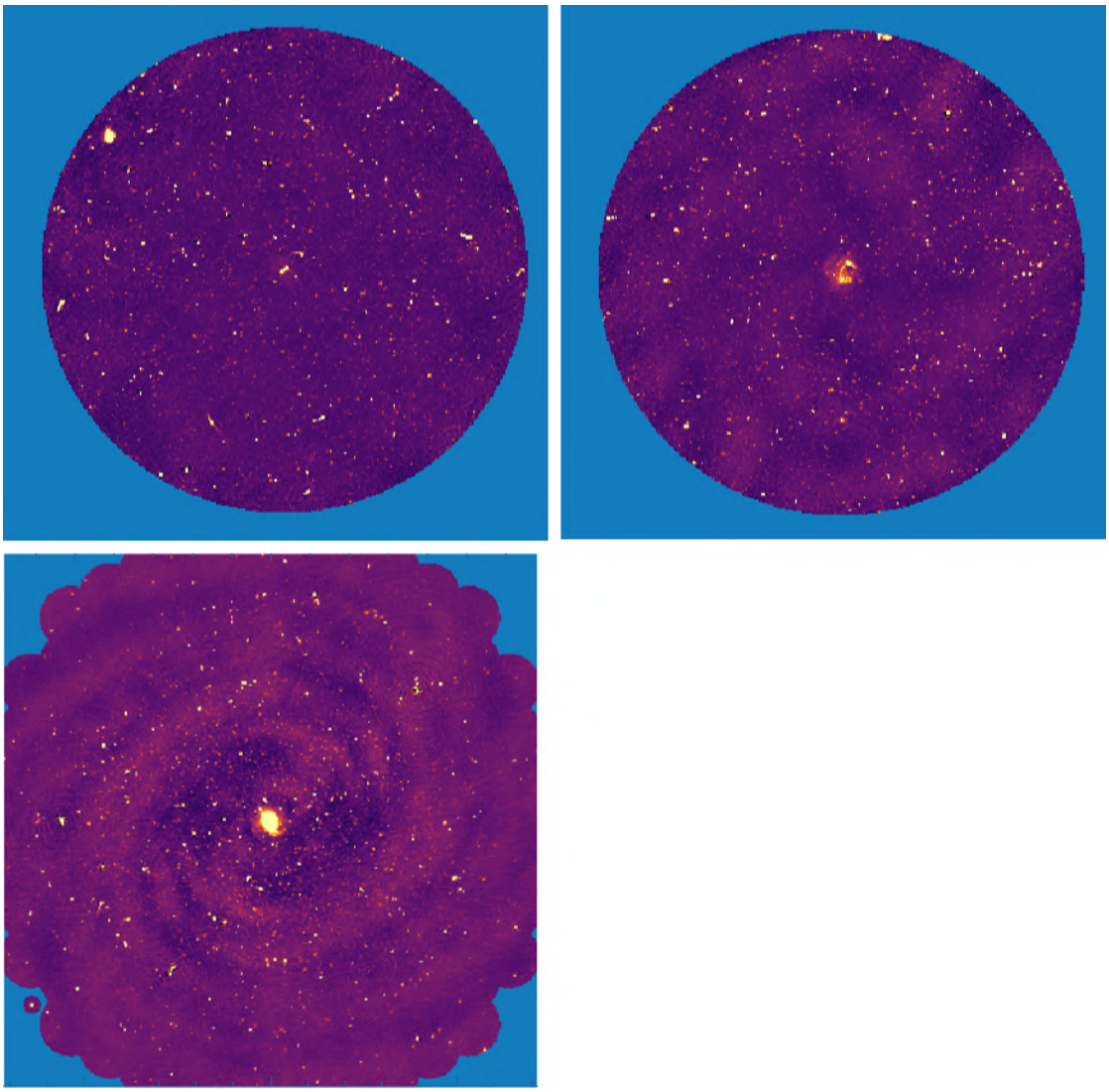


Figure 2.4: The sample of images that passed visual inspection. The first panel on the top left shows an image from NGC 1371, the top right panel is from NGC 5068, and the bottom panel displays the image from NGC 1566.

2.6 Method

In Section 2.1, where the Transients Pipeline (TraP) is initially defined, it is important to note that while the pipeline was originally designed for use with LOFAR data, it is adaptable for use with data from other radio telescopes as well (Swinbank et al., 2015). The data used were SARAO SDP images, which were automatically generated by the SARAO data pipeline. No additional calibration or primary beam correction was performed on images, as this had already been completed by the MeerKAT team (de Blok et al., 2024). The images were run through the

© University of Venda

Transient Pipeline with certain parameters that have been set on TraP see Table 2.2. The data were used as it is. The data are stored in the ilifu cloud computing facility, which is supported by contributions from IDIA.

Identifying transient and variable sources involved several key steps, as outlined in Chapter 2. TraP provides adjustable settings for optimal transient searches, although most of the survey's requirements were met using the default configurations. Table 2.2 displays some of the input parameters employed in TraP, with several other parameters set within the Trap tool. Most TraP parameters are kept at their default values; see TraP parameters* for the list of all parameters.

Table 2.2: The parameters used within the TraP.

Parameter	**Value**
detection_threshold	8σ
extraction_radius	2000 pixels
force_beam	True
New_source_sigma_margin	1
elliptical_x	2
beamwidths_limit	1

1. The `Force_beam`, TraP sets all source fits to True if all sources match the restoring beam's size, shape, and orientation. In this case, TraP keeps these parameters constant.
2. The parameter `new_source_sigma_margin` is essential to detect false positives caused by fluctuations around the detection threshold. It was set to 1, which provides a margin of error expressed as a multiple of the root mean square (rms) of the previous best image.
3. The defined extraction radius, which is the distance in pixels within which TraP searches for candidates, was set to 2000 pixels. Therefore, TraP rejects any candidates located beyond 2000 pixels from the centre of the image. In commensal transient surveys, this radius typically aligns with the primary beam size, as the telescope's highest sensitivity is in this region.
4. The `detection_threshold` setting was determined, measured as a multiple of the rms noise (8σ).
5. Any images with a significantly elliptical restoring beam (i.e., $\frac{\mathbf{B}_{\text{major}}}{\mathbf{B}_{\text{minor}}} > 2$) are excluded from the analysis using the `elliptical_x parameter`. This parameter is utilised to filter out lower-quality images during the analysis.
6. The parameter `beamwidths_limit` manages the range, in units of the restoring beam, from a recently detected source. The source association algorithm uses this range to search for associations.

*https://tkp.readthedocs.io/en/latest/userref/config/job_params_cfg.html

© University of Venda

This study is based on previous research that utilised the Transient Pipeline to search for transient and variable sources, including the work of (Rowlinson et al., 2022) and (Driessen et al., 2020), Who analysed the distributions of variability parameters (η_ν and V_ν) and visually inspected radio images and light curves to identify transient or variable sources. In my case, this was done in three galaxies: the NGC 5068, NGC 1566 and NGC 1371 fields. A scatter plot of η_ν versus V_ν was generated, as shown in Figure 3.1. These dimensionless variability metrics, first introduced by Swinbank et al. (2015), were calculated for each detected source using the Transient Processing pipeline (TraP). Any source with variability parameters exceeding 2σ in either V_ν or η_ν was flagged as potentially variable.

Two key parameters that TraP generates help identify variable sources: the reduced weighted chi-square (χ^2) of a fit that assumes constant brightness (represented by the symbol η_ν) and the coefficient of variation $V = \frac{s}{\langle I \rangle}$. The symbol ($s$) represents the standard deviation of the flux density measurements, while $\langle I \rangle$ denotes the average flux density of the source, as defined in (Swinbank et al., 2015), the TraP detects sources that exceed a user-defined threshold in a series of astronomical images, generates light curves for each unique source, and computes various statistical properties to characterise them.

After successfully running the TraP on the three galaxies—NGC 5068, NGC 1566, and NGC 1371—the pipeline produced results based on the predefined parameters (see; Table 2.2). For each light curve in the database, a set of aggregate properties is calculated to characterize the astronomical source. These include the weighted mean position, flux density, and various variability indices that measure both the magnitude and significance of the observed variability.

2.7 Counterparts across different wavelengths

Multi-wavelength astronomy is the study of astronomical objects using observations across different parts of the electromagnetic spectrum. Since celestial objects emit radiation at various wavelengths (radio, infrared, optical, ultraviolet, X-ray, gamma-ray), analysing them across multiple wavelengths provides a more complete picture of their physical properties and processes. This section will give an overview of different databases and multi-wavelengths that were searched for the potential variable and transient sources identified in this study.

For all sources that show a Gaussian distribution above the 2σ threshold for either V_ν or η_ν, they are considered as variable candidates. Multi-wavelength analysis was used on the selected sources for further examination. The radio position for the candidates was used to search for their counterparts. VizieR catalogues (Ochsenbein et al., 2000) are an astronomical databases that provides access to a vast collection of astronomical catalogues and surveys across multiple wavelengths. It was used to identify optical counterparts for different sources using candidate

© University of Venda

coordinates. The Gaia DR3 Catalogue (Gaia Collaboration et al., 2023), which is available via VizieR, was used to help identify optical counterparts of radio sources. Parallax and proper motion data help distinguish between Galactic and extragalactic radio sources. Additionally, SIMBAD (Wenger et al., 2000) and The Dark Energy Survey (DES; Choi 2021) were also used to identify optical counterparts and DES to show the optical snapshot of potential candidates. NED Database (Helou et al., 1991) was searched for counterparts; NED provides a unified resource for extragalactic objects (galaxies, AGNs, quasars, etc.) by integrating data across multiple surveys and multi-wavelength (radio, optical, IR, X-ray, etc.). It includes positions and photometry, as well as spectral energy distributions (SEDs).

© University of Venda

University of Venda
Creating Future Leaders

Chapter 3

Results for the NGC 5068 field

NGC 5068 is a nearby, $d = 5.2$ Mpc barred spiral galaxy. It is an active star-forming galaxy of intermediate stellar mass ($M_* = 2.29{\times}10^9 M_\odot$) located well within the scatter of the star formation main sequence (Healy et al., 2024). NGC 5068 consists of 10 different epochs, and the observations were conducted between 03 April 2021 and 13 March 2022. The right ascension (J2000.0) of the galaxy is 13h 18m 54.81s, and the declination of the galaxy is (J2000.0) $-21°2'20.8''$. The galaxy hosts a well-established population of Wolf-Rayet (W-R) stars—helium-burning remnants of massive O stars with powerful stellar winds (Grasha et al., 2022).

This chapter presents the analysis results of the NGC 5068 galaxy. It begins with the distribution of variability parameters in Section 3.1. The light curves and snapshot images of variable sources detected using TraP are then examined in Sections 3.2 and 3.3. Finally, Section 3.5 details the search for multi-wavelength counterparts; each identified source is discussed in detail along with their characteristics.

3.1 Variability parameters η_ν and V_ν

Figure 3.1 presents a plot of two statistical variability parameters: η_ν (on the x-axis) against V_ν (on the y-axis). The values of η_ν and V_ν were calculated $\eta_\nu = 171.41$ and $V_\nu = 0.22$. A total of 4378 sources with variability metrics were identified, each assigned a unique running catalogue number. The sources investigated are located above the diagonal solid black line in the plot. 12 confirmed variable sources were found in this field, represented by different colours and shapes (see Table 3.1 for colours and shapes of the sources). The analysis focused on these sources because they have high values of η_ν and V_ν. These sources could represent genuine variability or transient events, making them significant in the context of this study. The green sources represent those for which no further investigation was done. Instead, the radio images and light curves for these sources were visually inspected across 10 epochs in the field as shown in Figures

© University of Venda

3.3 and 3.4 together with their light curve in Figure 3.2. The visual inspection revealed stable unresolved point sources showing no significant variations within the light curve an example of this source is shown in Figure 3.2. The black sources below the diagonal line were not investigated at all. No transient sources were detected for this galaxy; 12 variable sources were found. Their radio images showed a point source, not an extended source, at every epoch, and the light varied.

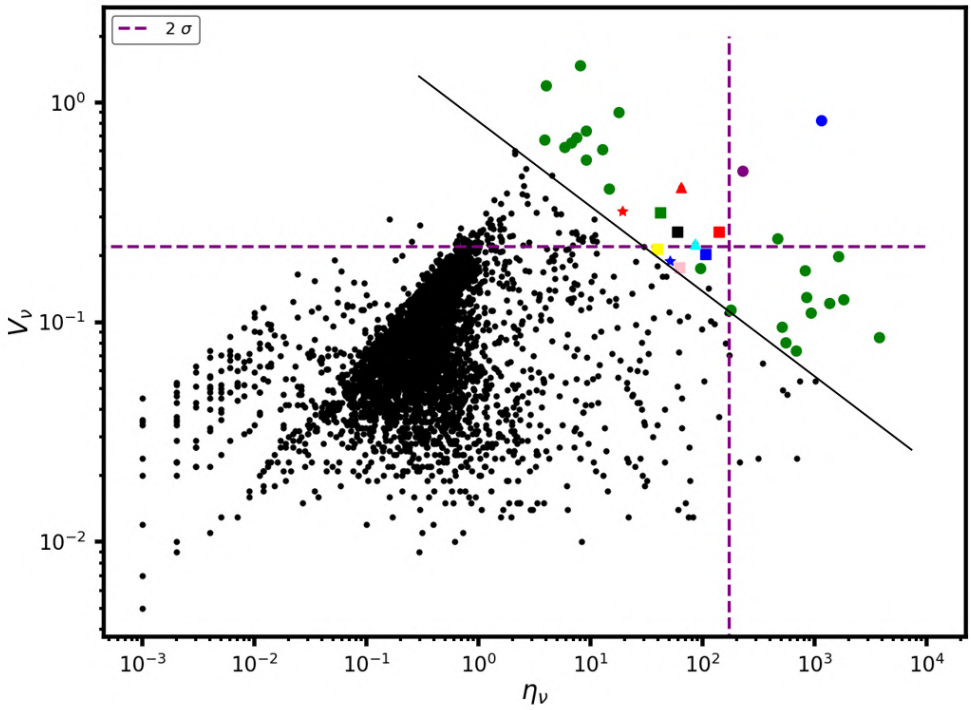


Figure 3.1: Distribution of two variability metrics, V_ν and η_ν. The dashed purple lines show the 2σ thresholds used for filtering these parameters, the thresholds are $V_\nu = 0.22$ and $\eta_\nu = 171.41$. Different colours represent 12 variable sources, and black sources were not investigated.

© University of Venda

Table 3.1: Characteristics of 12 variable sources identified in Figure 3.1, including their ID, position (RA and DEC), variability metrics, colour, and shape.

ID	RA (hh:mm:ss.s)	DEC (dd:mm:ss.s)	η_ν	V_ν	Colour	Shape
74654	13h17m54.4s	$-20°55'04.4''$	1141.19	0.827	blue	o (circle)
75133	13h17m11.6s	$-20°57'26.2''$	228.67	0.490	purple	o (circle)
73087	13h19m47.7s	$-21°12'28.1''$	140.06	0.260	red	s (square)
73395	13h19m27.0s	$-20°38'05.9''$	105.85	0.210	blue	s (square)
74898	13h17m34.9s	$-21°00'01.6''$	85.40	0.230	cyan	^ (triangle up)
74455	13h18m11.1s	$-21°28'31.2''$	64.48	0.410	red	^ (triangle up)
75267	13h16m51.8s	$-20°56'35.1''$	62.58	0.180	pink	s (square)
73326	13h19m30.9s	$-20°58'01.2''$	59.43	0.260	black	s (square)
73612	13h19m09.0s	$-21°16'27.8''$	51.25	0.190	blue	* (star)
75046	13h17m20.3s	$-21°02'53.5''$	41.83	0.310	green	s (square)
72807	13h20m10.6s	$-21°10'31.0''$	39.24	0.220	yellow	s (square)
74685	13h17m52.1s	$-21°13'27.3''$	19.28	0.320	red	* (star)

© University of Venda

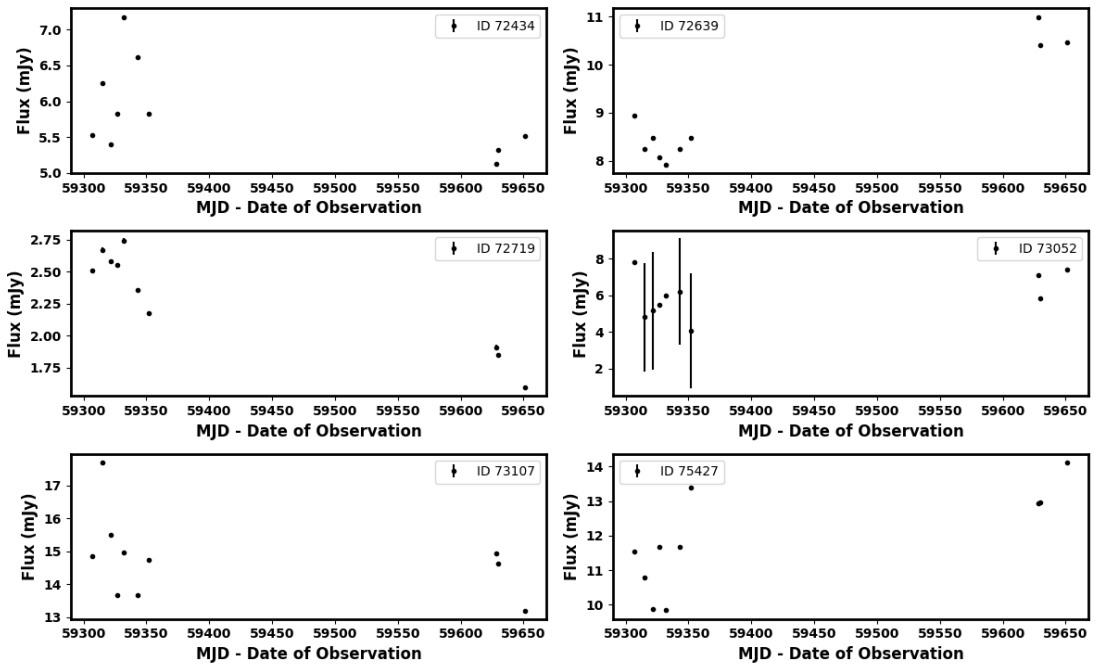


Figure 3.2: Light curves of some selected green sources identified in Figure 3.1, corresponding to unique IDs 73107, 72639, 73052, 72434, 75427, and 72719. These light curves show no significant variability, suggesting that the sources remained stable throughout the observation period. In some light curves, the error bars were too small to be visible on the light curves.

© University of Venda

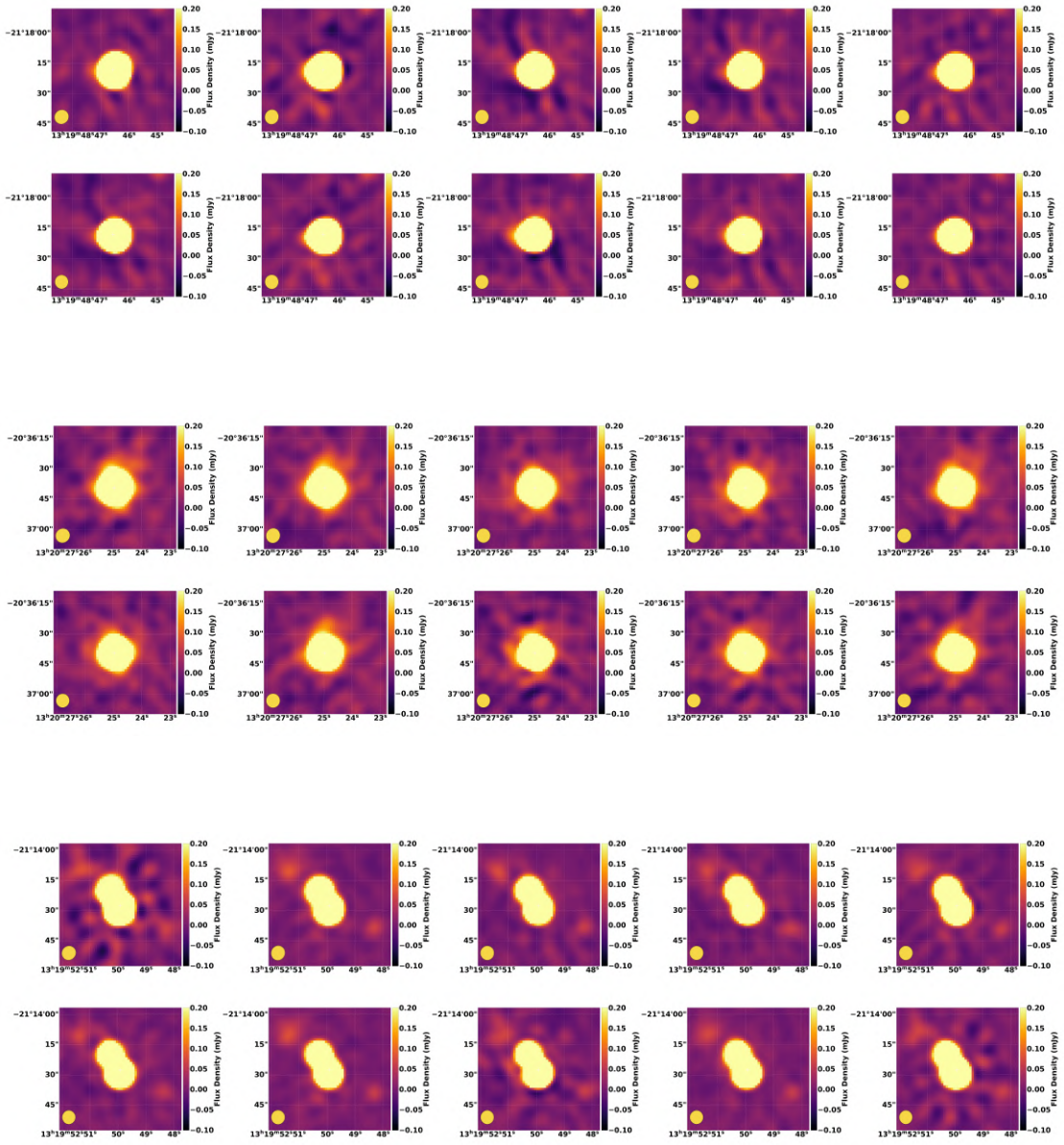


Figure 3.3: The radio snapshot images of green sources identified in Figure 3.1 where in their corresponding light curves are shown in Figure 3.2. The first panel represents SRC72434; the middle panel corresponds to SRC72639; the bottom panel represents SRC72719. All the images are scaled to the same flux density range of -0.10 to 0.20 milliJansky (mJy) on a linear scale. The yellow circle in the lower-left corner of each image indicates the point spread function (PSF). Flux remains constant throughout the whole 10 epochs.

© University of Venda

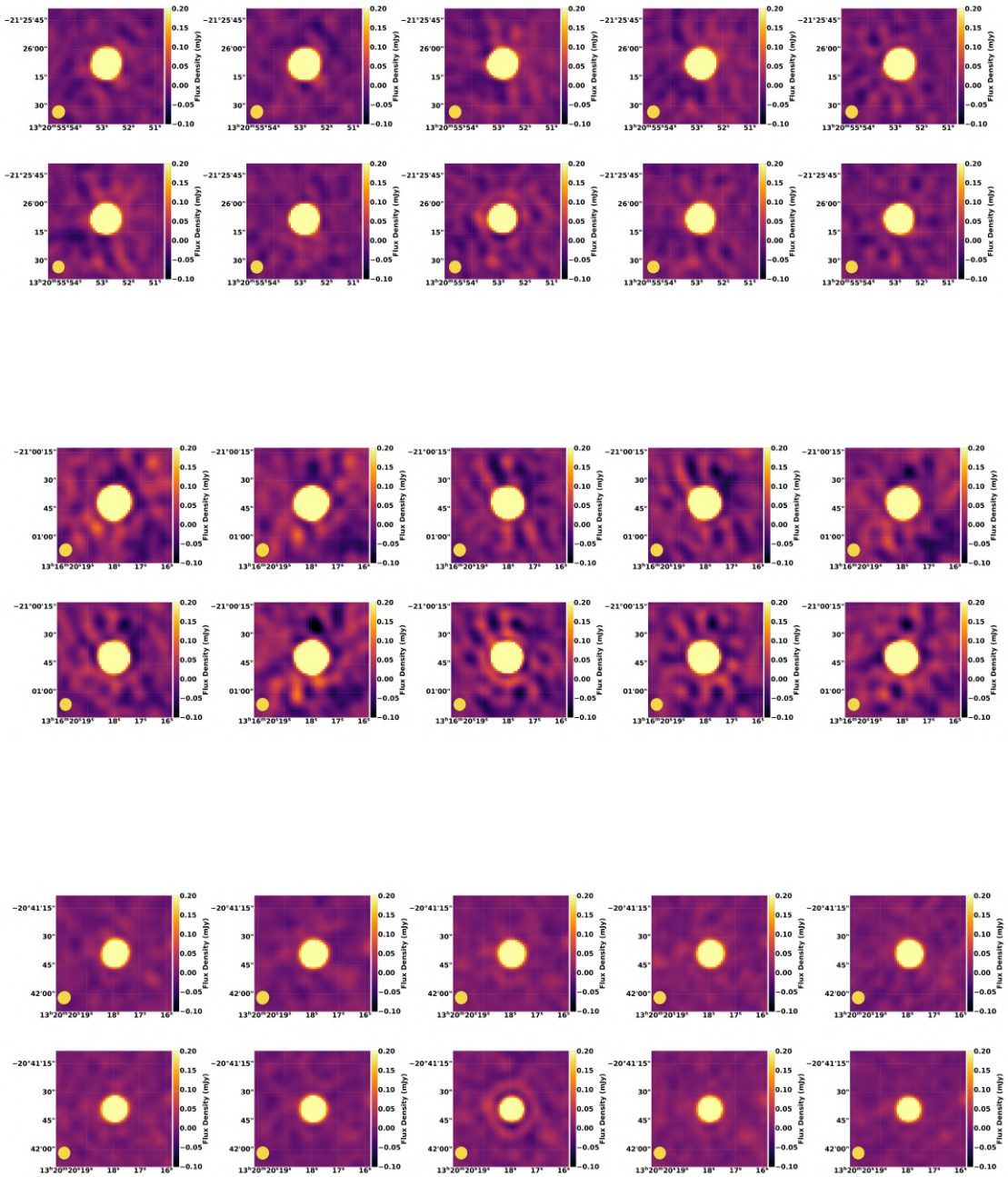


Figure 3.4: Snapshot of radio images of selected green sources from Figure 3.1, with their corresponding light curves shown in Figure 3.2. The first panel displays SRC73052, the middle panel shows SRC73107 and the last panel represents SRC75427. Every image has been linearly scaled to the same flux density range: (-0.10 to 0.20) mJy. The yellow circle in the lower-left corner shows each image's PSF. For the entire ten epochs, flux stays constant in each panel.

© University of Venda

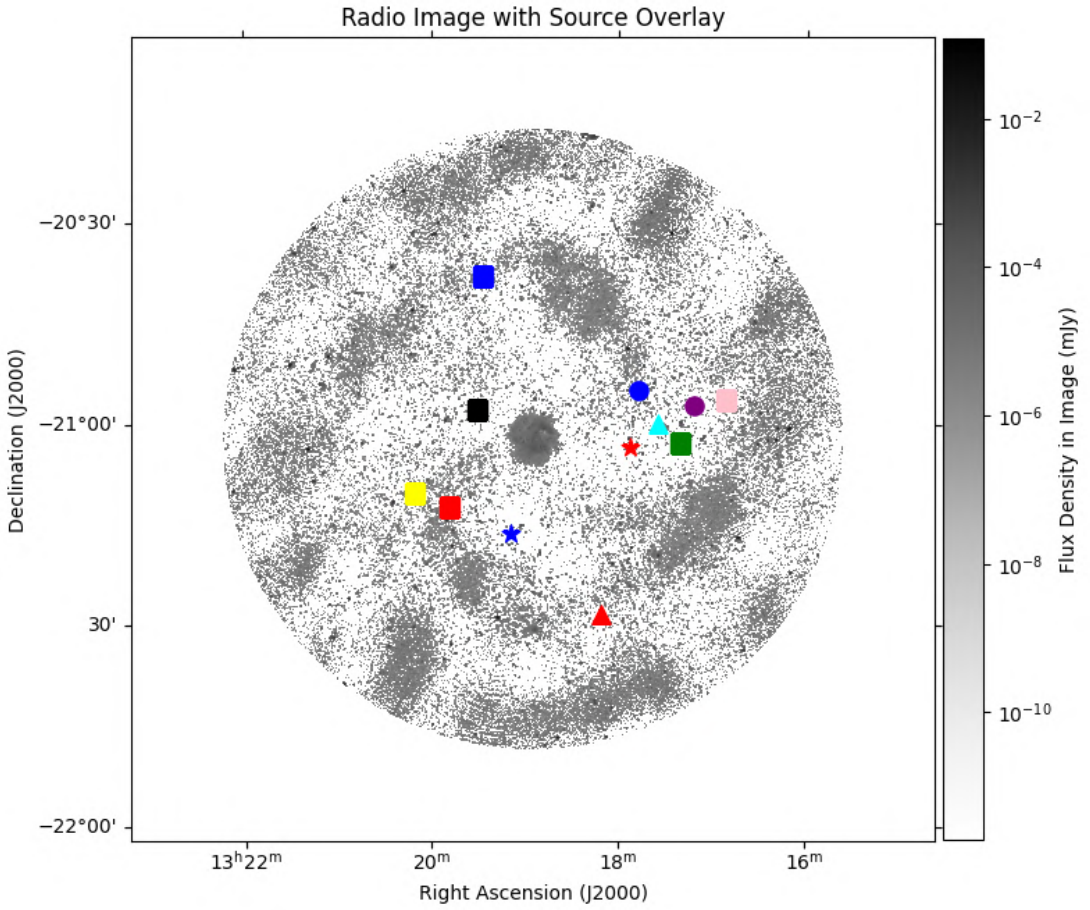


Figure 3.5: MeerKAT SDP image with source overlay of the field of NGC 5068. The sources marked in different shapes and colours denote 12 variable sources as listed in Table 3.1.

© University of Venda

3.2 Light curves of variables sources

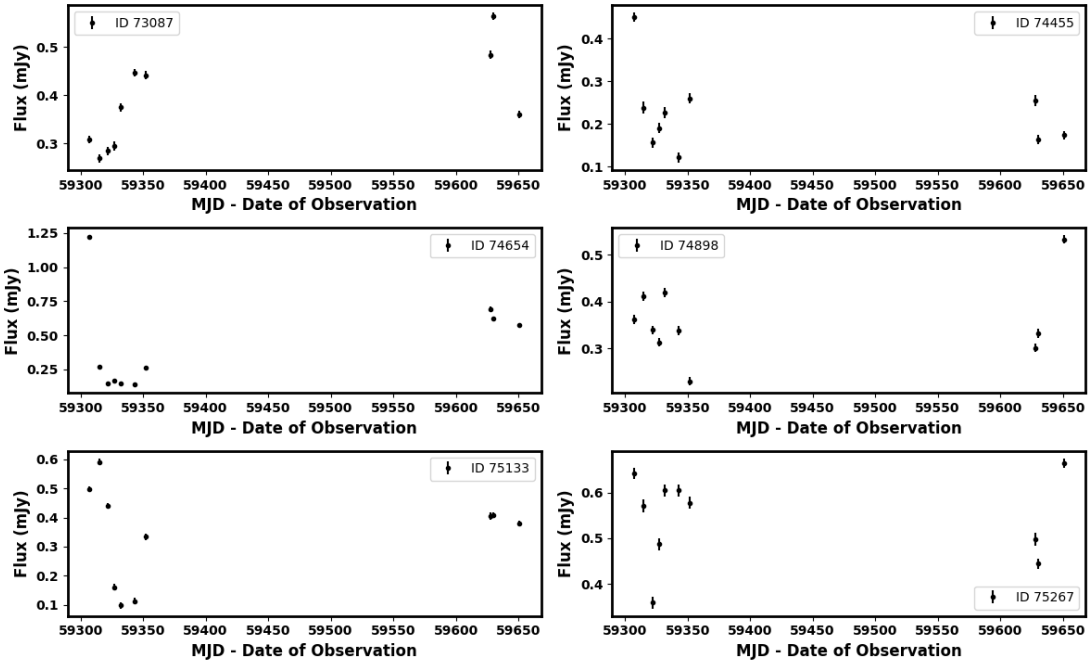


Figure 3.6: Light curves of variable sources located above the diagonal solid line in Figure 3.1, corresponding to unique IDs 73087, 74455, 74654, 74898, 75133, and 75267. In some light curves, flux density uncertainties are too small to be visible on the light curves.

The radio light curves presented in Figures 3.6 and 3.7 illustrate the flux density over time of variable sources identified in Figure 3.1, revealing significant variability among all observed sources. Each plot corresponds to a distinct source, identified by its unique ID shown in Table 3.1. These sources exhibit noticeable changes in flux density over time. Each source is discussed in detail in Section 3.5.

© University of Venda

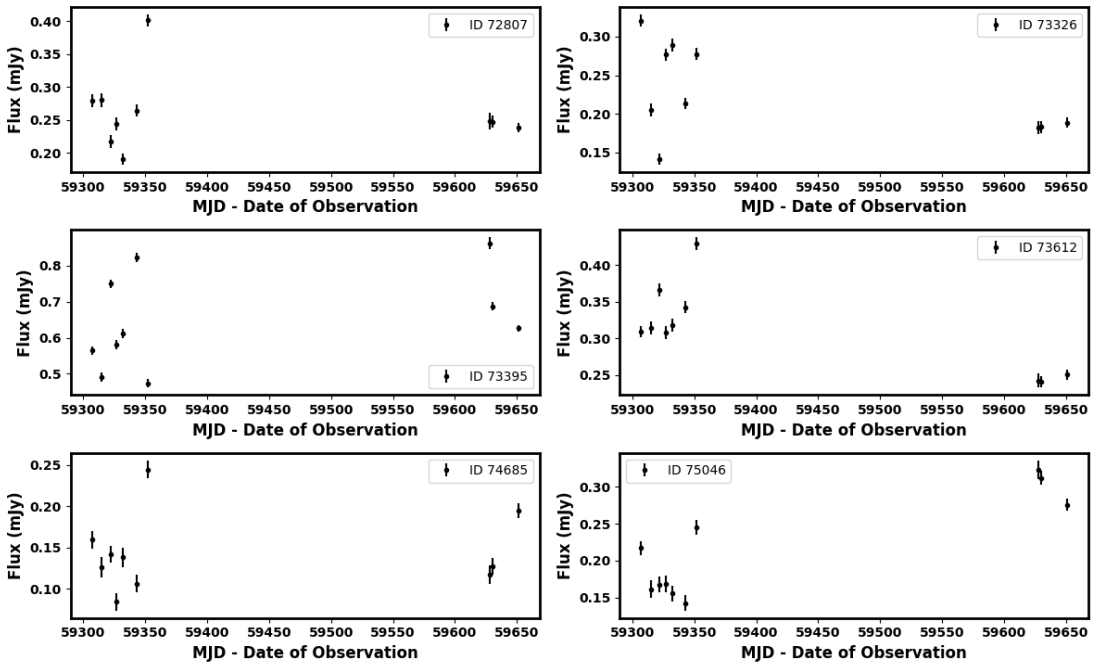


Figure 3.7: Light curves of variable sources located above the diagonal solid line in Figure 3.1, corresponding to unique IDs: 72807, 73326, 73395, 73612, 74685 and 75046. In some light curves, flux density uncertainties are too small to be visible on the light curves.

3.3 Snapshots of variable sources identified in NGC 5068

This section shows a series of radio images identified in Figure 3.1, displayed in the grid, which shows a point source that illustrates a significant variation in brightness in different epochs. The images are organised from upper left to upper right in chronological order. Each image is scaled linearly to the same flux density in mJy for each source per panel. There are differences in flux between epochs. In every image, the synthesised beam may be found in the lower left corner. Recall that changes in size and angle between epochs likely introduce nonintrinsic variability (Andersson et al., 2023). Point Sources: This observation suggests the source is unresolved, indicating it is a point source rather than an extended object. The point source's brightness fluctuations across different epochs imply it is a variable radio source. This variability could result from changes in intrinsic luminosity or interactions with the surrounding medium. Extended Sources: Extended variations are caused by changes in the PSF and a source larger than the beam (lower left). Transient/Variable classifications are the ones we are specifically searching for, representing point sources with variable light curves.

© University of Venda

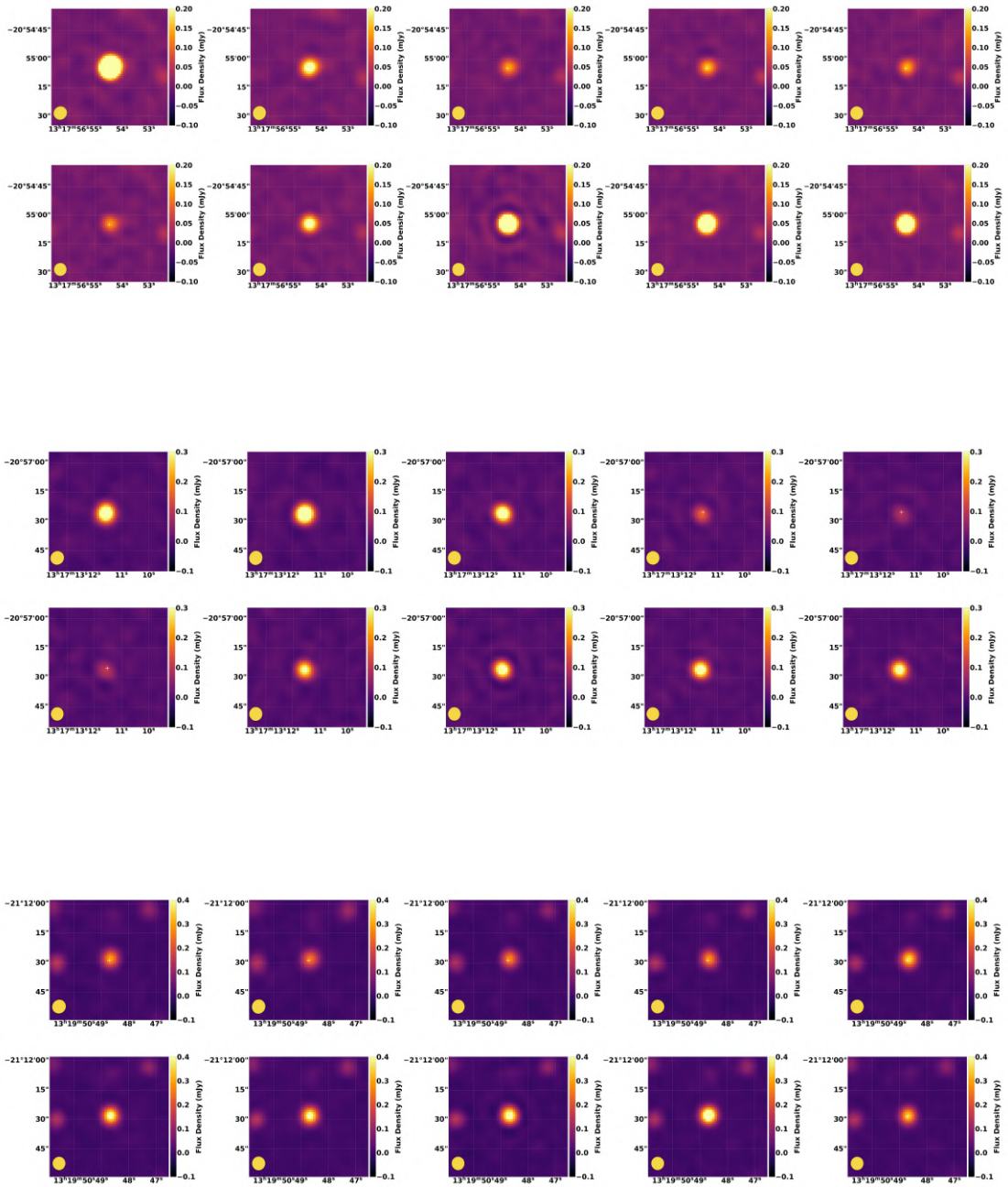


Figure 3.8: Radio image snapshots showing each source across ten observed epochs. The first panel represents SRC74654, with a flux density range of -0.10 to 0.20 mJy. The middle panel corresponds to SRC75133, with a flux density range of -0.10 to 0.30 mJy, while the bottom panel represents SRC73087, also within a flux density range of -0.1 to 0.4 mJy. The yellow circle in the lower-left corner of each image indicates PSF. Flux variations are observed across epochs.

© University of Venda

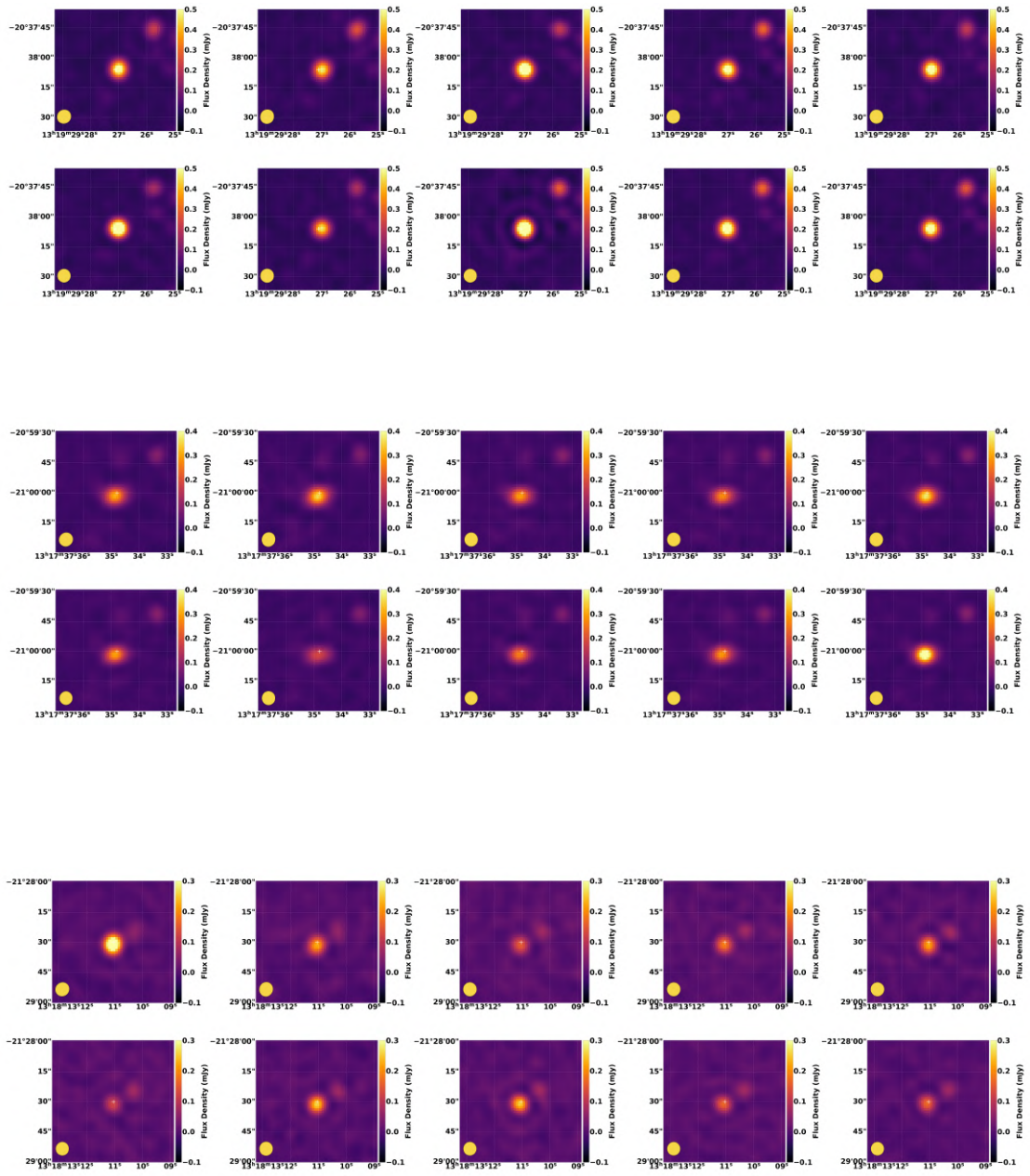


Figure 3.9: Snapshots of radio images from ten observed epochs, each panel displays each source. SRC73395 is represented by the first panel, which has a flux density range of -0.1 to 0.5 mJy. SRC74898 is represented by the middle panel, which has a flux density range of -0.1 to 0.4 mJy. SRC74455 is represented by the bottom panel, which has a flux density range of -0.10 to 0.30 mJy. The yellow circle in the lower-left corner shows each image's PSF. There are differences in flux between epochs.

© University of Venda

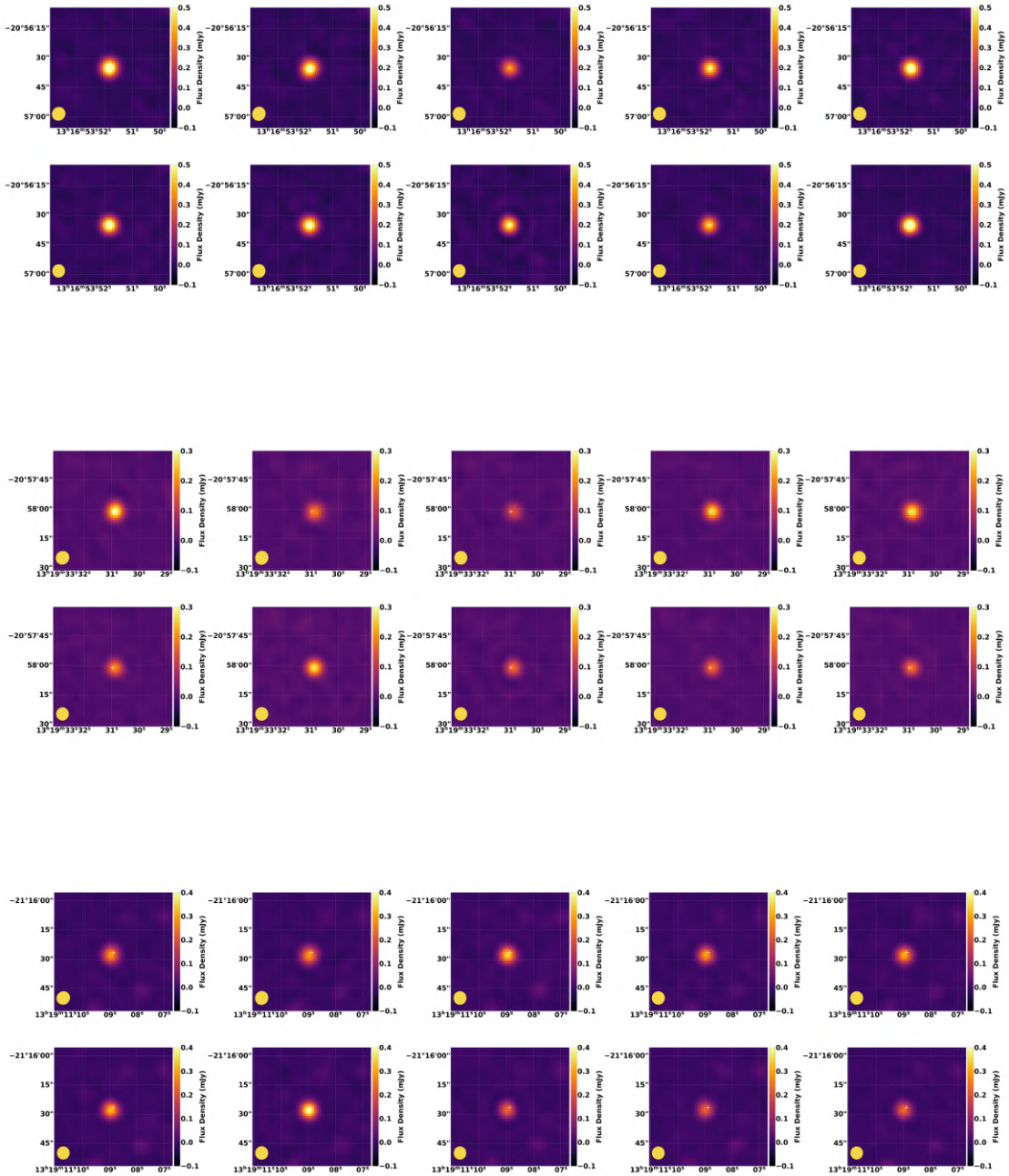


Figure 3.10: Radio images snapshots from ten epochs that display each source per panel. The first panel, which has a flux density range of -0.1 to 0.5 mJy, is for SRC75267. With a flux density range of -0.10 to 0.30 mJy, the middle panel represents SRC73326, while the bottom panel represents SRC73612, whose flux density range is -0.1 to 0.4 mJy. Each image displays the PSF as a yellow circle in the lower-left corner. Across epochs, flux fluctuations are seen.

© University of Venda

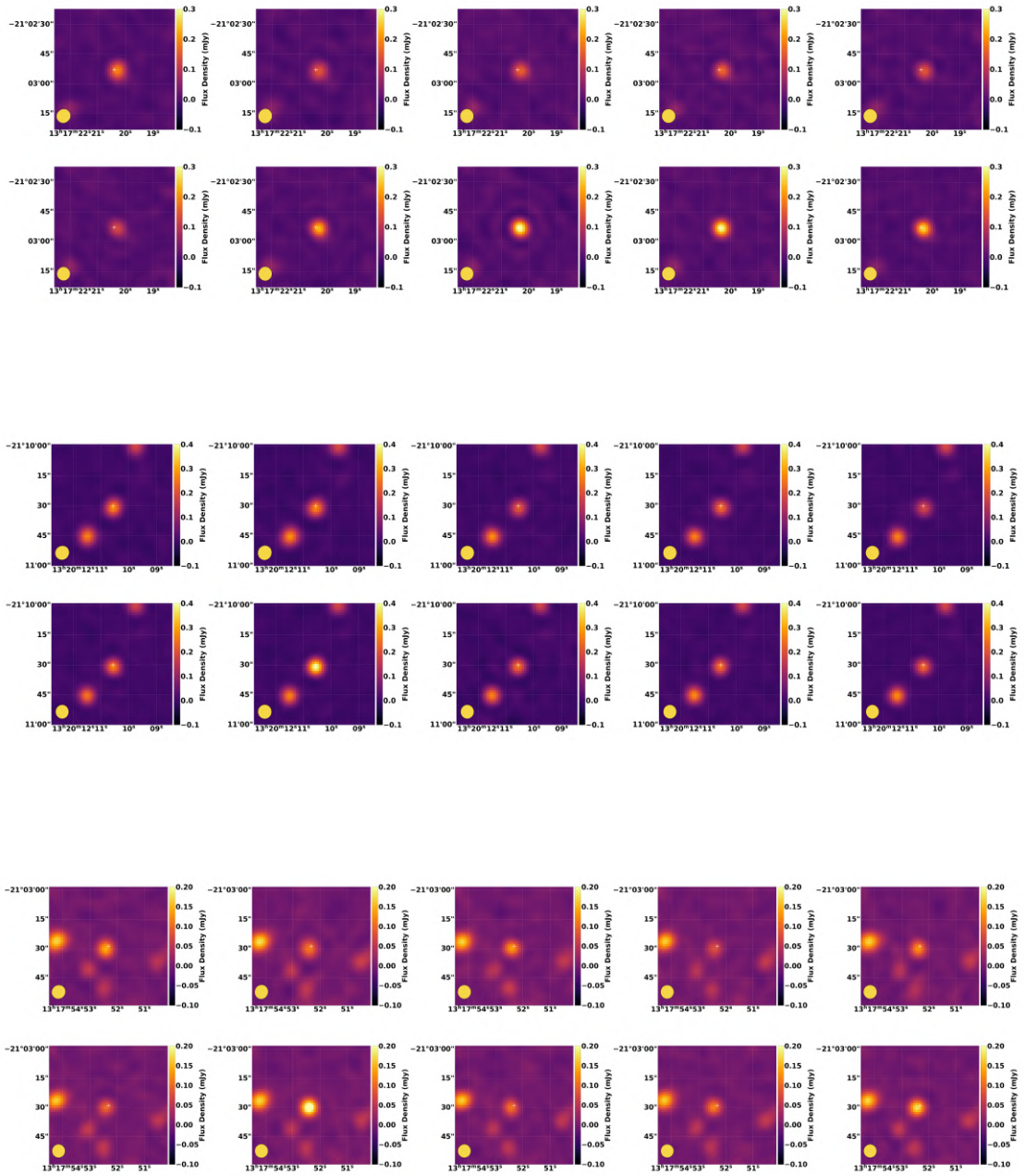


Figure 3.11: Radio image snapshots from ten epochs, each displaying a different source per panel. The first panel represents SRC75046 with a flux density range of -0.10 to 0.30 mJy. The middle panel corresponds to SRC72807, with a flux density range of -0.1 to 0.4 mJy, while the bottom panel shows SRC74685, ranging from -0.10 to 0.20 mJy. The yellow circle in the lower-left corner of each image indicates the PSF. Flux variations are observed across epochs.

© University of Venda

3.4 Correlation of flux density and variability parameter η and V

Figure 3.12 presents the relationship between flux density and the variability parameters η and V for sources in the NGC 5068 galaxy dataset. The parameters η and V are useful for assessing the statistical significance and amplitude of variations in flux, respectively. We generally expect η to correlate with the average flux density because the brightest sources typically exhibit the smallest statistical uncertainties. Similarly, we anticipate an inverse correlation between V and $\bar{F}$, as we are more likely to detect minor variations in the brightest sources. However, it's important to note that errors in flux calibration can sometimes cause an overestimation of statistical significance in bright sources (Swinbank et al., 2015).

In Figure 3.12, the left panel shows η versus flux, and the right panel shows V versus flux. As expected, η tends to increase with increasing flux, indicating that fainter sources generally have higher statistical uncertainties. The plot also reveals a trend where V decreases with increasing flux, supporting the idea that we are more sensitive to smaller variations in brighter sources. The distribution in the plots suggests that while these relationships generally hold, there are instances where calibration errors or other factors may cause deviations, particularly for bright sources.

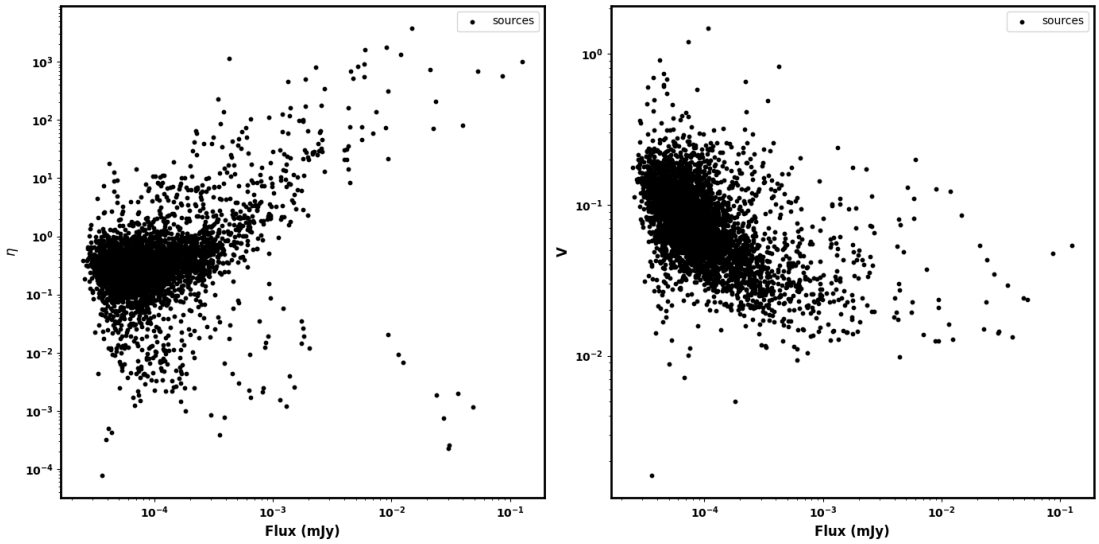


Figure 3.12: The correlation between the flux density and the variability parameters. The left panel shows η vs Flux (mJy), whereas the right panel shows V against flux (mJy).

© University of Venda

3.5 Counterparts across different wavelengths

Counterparts at different wavelengths were searched by examining several catalogues in the VizieR database (Ochsenbein et al., 2000). The Dark Energy Survey (DES; (Choi, 2021)), known for its significantly deeper optical imaging, was used, along with other databases and catalogues such as Simbad (Wenger et al., 2000), Gaia (Gaia Collaboration et al., 2023), NED (Helou et al., 1991), AllWISE Source Catalog (Wright et al., 2019), and PanSTARRS (Chambers & Pan-STARRS Team, 2016). The objective was to follow up on selected sources in multi-wavelength, enabling a comprehensive comparison and validation of the findings. For NGC 5068 galaxy, no counterpart was found in the Dark Energy Survey (DES) DR1 catalogue, as shown in Table 3.2. The R-band magnitude of the source is recorded as "N/A," indicating the absence of a detected counterpart. The Pan-STARRS Catalogue (Optical/Near-Infrared) wavelength was used to show the optical images shown in Figures 3.13 to 3.14 and discussed in Section 3.5.

Table 3.2: Summary of the characteristics of the 12 variable sources, including their Source ID, RA, DEC, variability indices η_ν and V_ν, and peak flux measurements with uncertainties, highlighting their variability and flux ranges.

ID	RA (hh:mm:ss.s)	DEC (dd:mm:ss.s)	η_ν	V_ν	Peak flux (mJy)	Peak flux error (mJy)	R (mag)
74654	13h 17m 54.4s	$-20°55'04.4''$	1141.19	0.83	1.2194	0.0068	N/A
75133	13h 17m 11.6s	$-20°57'26.2''$	228.67	0.49	0.5912	0.0070	N/A
73087	13h 19m 47.7s	$-21°12'28.1''$	140.06	0.26	0.5637	0.0045	N/A
73395	13h 19m 27.0s	$-20°38'05.9''$	105.85	0.20	0.8624	0.0093	N/A
74898	13h 17m 34.9s	$-21°00'01.6''$	85.40	0.23	0.5328	0.0049	N/A
74455	13h 18m 11.1s	$-21°28'31.2''$	64.48	0.41	0.4499	0.0065	N/A
75267	13h 16m 51.8s	$-20°56'35.1''$	62.58	0.18	0.6653	0.0060	N/A
73326	13h 19m 30.9s	$-20°58'01.2''$	59.43	0.26	0.3207	0.0045	N/A
73612	13h 19m 09.0s	$-21°16'27.8''$	51.25	0.19	0.4297	0.0048	N/A
75046	13h 17m 20.3s	$-21°02'53.5''$	41.83	0.31	0.3227	0.0075	N/A
72807	13h 20m 10.6s	$-21°10'31.0''$	39.24	0.22	0.4009	0.0052	N/A
74685	13h 17m 52.1s	$-21°13'27.3''$	19.28	0.32	0.2443	0.0064	N/A

In this study, we refer to individual sources using the prefix “SRC” followed by their unique identification number (e.g., SRC74654). This convention is adopted for clarity and consistency when referencing sources detected in our analysis.

3.5.1 SRC74654

SRC274654 is located at RA 13h17m54.4s and DEC $-20°44'04.4''$. The radio light curve is shown in Figure 3.6. It shows clear variability, and it is worth noting that the uncertainty in the flux density measurements is too small to be visible on the light curve, ranging from 0.0040 to 0.0068 mJy. The light curve starts with a high flux density of 1.2194 mJy and drops to its lowest

© University of Venda

flux density (0.1419 mJy) and then rapidly increases. SRC74654 is the brightest source. The radio cutout images in Figure 3.8 confirm these observations, the first panel represents the radio source SRC74654. There is a variation change in brightness from epoch to epoch; it started as a very bright source, then dimmed and returned to being bright again.

The Simbad database was searched for counterparts using the source radio coordinates, but no known associations were found. Additionally, no counterpart was identified in the DES as indicated in Table 3.2. There is no R (mag) of the source "N/A". However, The ALLWISE source catalogue indicated the source associated with: WISEA J131754.40-205504.4 object type Infrared source, separation arcminutes (0.002) (Cutri et al., 2013).

3.5.2 SRC75133

SRC75133 is located at RA 13h17m11.6s and DEC $-20°57'26.2''$. The radio light curve in Figure 3.6 shows a clear variability with a peak flux of 0.5912 mJy and flux density measurement uncertainties ranging from 0.0048 to 0.0070 mJy, too small to be visible on the light curve. In the radio image presented in Figure 3.8, the middle panel represents the SRC75155. Observe a change in brightness from epoch to epoch; the source begins as very bright, dims, and then brightens again.

The Simbad database was searched using the source coordinates, but no known associations were found. Similarly, no counterpart was identified in the DES, as indicated in Table 3.2, where the R-band magnitude (R mag) for the source is listed as "N/A". However, the ALLWISE source catalogue did indicate an association with the object WISEA J131711.57-205726.7, classified as an infrared source with a separation of 0.011 arcminutes (Cutri et al., 2013).

3.5.3 SRC73087

SRC73087 is located at RA 13h19m47.7s and DEC $-21°12'28.1''$. The radio light curve is shown in Figure 3.6. It exhibits clear variability; flux density measurement uncertainties range from 0.0040 to 0.0052 mJy which are too small to be noticeable on the light curve, with a maximum peak flux density of 0.5637 mJy and minimum flux density of 0.2691 mJy. The radio cutout images in Figure 3.8, the last panel represents the radio source SRC73087. A change in brightness is observed across different epochs; the source initially appears dim but then brightens and shows significant fluctuation.

The Simbad database was searched using the source coordinates, but no known counterpart was found for this target. No counterpart was detected in Pan-STARRS, and no associated source in the DES. The ALLWISE source catalogue identifies an infrared source, WISEA J131948.68-211227.2, with a distance of 0.014 arcminutes (Cutri et al., 2013).

© University of Venda

3.5.4 SRC73395

SRC73395 is located at RA 13h19m27.0s DEC $-20°38'05.9''$. The light curve of SRC73395 shows clear radio variability, within a flux range of 0.8624 - 0.4734 mJy, as shown in Figure 3.7. Flux density measurement uncertainty ranges from 0.0056 to 0.0093 mJy, which is too small to be visible on the light curve. In the radio cutout image in Figure 3.9, the first panel represents the radio source SRC73395. It reveals a change in brightness across different epochs and shows significant variation in the radio image.

The source coordinates were used to search Simbad, but no counterpart was found. Similarly, no counterpart was identified in RACS, and the DES also shows no associated source. However, a match was found in the ALLWISE catalogue of an infrared source, WISEA J131948.68-211227.2, with a distance of 0.004 arcminutes (Cutri et al., 2013).

3.5.5 SRC74898

SRC74898 is located in RA 13h17m34.9s and DEC $-21°00'01.6''$. Figure3.6 shows a radio light curve of the source. Flux density measurement uncertainties range from 0.0049 to 0.0060 mJy, which is too small to be noticeable on the light curve. A maximum peak flux density of 0.5328 mJy and minimum flux density of 0.2301 mJy. In the radio image in Figure 3.9, the middle panel represents the radio source SRC74898. It confirms observation and shows a variation in brightness across different epochs.

The Simbad database was searched using the source coordinates, but no known counterpart was found. Similarly, no counterpart was identified in the DES, as noted in Table 3.2, where the R-band magnitude (R mag) for the source is marked as "N/A", the peak flux for this source is 0.5328 mJy. However, the ALLWISE source catalogue lists an infrared source, WISEA J131734.46-210009.0, with a separation of 0.160 arcminutes (Cutri et al., 2013). A search within 0.2 arcminutes in Gaia data release 2 (Gaia DR2) (Gaia Collaboration et al., 2018) identifies the source 3506369553372670720.

3.5.6 SRC74455

SRC74455 is located in RA 13h18m11.1s and DEC $-21°28'31.2''$. A radio light curve with a visible error bar is shown in Figure 3.6. Flux density measurement uncertainties range from 0.0058 to 0.0078 mJy is too small to be noticeable on the light curve, with a maximum peak flux density of 0.4499 mJy and minimum flux density of 0.1209 mJy. The radio image in Figure 3.9, the last panel represents the radio source SRC74455. shows a variation in brightness across different epochs. The source starts bright and gradually dims over time, showing significant variation.

© University of Venda

The Simbad database was searched using the source coordinates, but no known counterpart was found. Similarly, no counterpart was identified in the DES. As shown in Table 3.2, this source's R-band magnitude (R mag) is listed as "N/A" and the peak flux is 0.4499 mJy. However, a source was found in the ALLWISE catalogue: WISEA J131811.08-212831.7, classified as an Infrared source. The separation between the ALLWISE source and our target is 0.010 arcminutes (Cutri et al., 2013). A search within 0.2 arcmin in the Gaia Data Release 2 (Gaia DR2) (Gaia Collaboration et al., 2018) yielded no associated sources.

3.5.7 SRC75267

SRC75267 is located in RA 13h16m51.8s and DEC $-20°56'35.1''$. A radio light curve with a visible error bar is shown in Figure 3.6. Flux density measurement uncertainties range from 0.0060 to 0.0084 mJy too small to be noticeable on the light curve, with a maximum peak flux density of 0.6653 mJy and minimum flux density of 0.3581 mJy. In the radio cutout image in Figure 3.10, the first panel represents the radio source SRC75267. shows a variation in brightness across different epochs.

Various multi-wavelength catalogues on Vizier were searched for counterparts, and the location was queried in Simbad, but no corresponding counterpart was identified. Similarly, the ALLWISE source catalogue revealed no source within a 0.2 arcminutes search radius.

3.5.8 SRC73326

SRC73326 is located in RA 13h19m30.9s and DEC $-20°58'01.2''$. A radio light curve in Figure 3.7, illustrates flux density measurement uncertainties ranging from 0.0037 to 0.0049 mJy, which are too small to be noticeable on the light curve, with a maximum peak flux density of 0.3207 mJy and minimum flux density of 0.1416 mJy. In the radio cutout image in Figure 3.10, the middle panel represents the radio source SRC73326. It confirms the variation in brightness across different epochs.

Various multi-wavelength catalogues on Vizier were searched, and the location was queried in Simbad, however, no corresponding counterpart was identified. Nevertheless, the ALLWISE catalogue shows a source identified as WISEA J131931.29-205759.5, an Infrared source with a separation of 0.138 arcminutes. Additionally, no matching object was found in the DES, where the R-band magnitude (R mag) for this source is listed as "N/A", and the peak flux recorded is is 0.3207 mJy as noted in Table 3.2.

3.5.9 SRC73612

SRC73612 is located in RA 13h19m9.0s and DEC $-21°16'27.8''$. A radio light curve in Figure 3.7, Shows flux density measurement uncertainties ranging from 0.0042 to 0.0054 mJy, too small to

© University of Venda

be noticeable on the light curve, with a maximum peak flux density of 0.4297 mJy and minimum flux density of 0.2409 mJy. In the radio cutout image in Figure 3.10, the last panel represents the radio source SRC73612. It confirms the variation in brightness across different epochs.

The Simbad database was searched using the source's coordinates, and no counterpart was found. Similarly, no counterpart was identified in the DES), where the R-band magnitude (R mag) for this source is listed as "N/A", and the peak flux is 0.4297 mJy in Table 3.2. However, a counterpart was found in the ALLWISE source catalogue.: WISEA J131908.99-211627.9, classified as an ultraviolet source with a separation of 0.011 arcminutes. A search within 0.2 arcminutes in the Gaia Early Data Release 3 (Gaia EDR3) (Gaia Collaboration et al., 2018) finds a counterpart associated with source 3506160096407981952.

3.5.10 SRC75046

SRC75046 is located at RA 13h17m20.3s and DEC $-21°02'53.5''$. When we look at its radio light curve (Figure 3.7), the flux density measurements have very tiny uncertainties, only ranging from 0.0048 to 0.0075 mJy. These are too small to be visible on the light curve. The source's brightness varies, with its maximum flux density reaching 0.3227 mJy and dipping to a minimum of 0.1423 mJy. Looking at the radio cutout image (Figure 3.11), the first panel represents the radio source SRC75046, and it visually confirms that the source's brightness changes over time.

The Simbad database was searched using the sources radio coordinates, and no known counterpart was found. Similarly, no counterpart was found in the DES, where the R-band magnitude (R mag) for this source is given as "N/A", and the peak flux is 0.3121 mJy see Table 3.2. However, a counterpart was identified in the ALLWISE source catalogue: WISEA J131720.29-210253.0, an infrared source with a separation of 0.007 arcminutes (Cutri et al., 2013). A search within 0.2 arcmin of (Gaia EDR3) produced no source associations.

3.5.11 SRC72807

SRC72807 is located at RA 13h20m10.6s and DEC $-21°13'27.3''$. When we look at its radio light curve (Figure 3.7), the flux density measurements have very tiny uncertainties, ranging from 0.0043 to 0.0075 mJy. These are too small to be visible on the light curve. The source's brightness varies, with its maximum flux density reaching 0.4009 mJy and dipping to a minimum of 0.1903 mJy. Looking at the radio cutout image (Figure 3.11), the middle panel represents the radio source SRC72807, visually confirming that the source's brightness changes over time.

Various multi-wavelength catalogues on VizieR were searched, and the location was queried in Simbad, but no corresponding counterpart was found. The ALLWISE source catalogue showed no sources within a 0.2 arcminutes search radius.

© University of Venda

3.5.12 SRC74685

SRC72807 is positioned at RA 13h17m52.1s and DEC $-21°13'27.3''$. The radio light curve (Figure 3.7) reveals flux density measurements with small uncertainties, ranging from 0.0052 to 0.0069 mJy, which are too small to be noticeable on the light curve. The source exhibits variability in brightness, with flux density peaking at 0.2443 mJy to a minimum of 0.0838 mJy. The radio cutout image (Figure 3.11), the last panel represents the radio source SRC74685, visually confirms this variation, illustrating the source's changing brightness over time.

The Simbad database was searched using the source's coordinates, and no known counterpart was found. Similarly, no matching object was identified in the DES, where the R-band magnitude (R mag) for this source is listed as "N/A", and the peak flux is 0.2443 mJy on Table 3.2. However, there was a counterpart found in the ALLWISE source catalogue: 2MASXi J1317524-210329, classified as an infrared source with a separation of 0.07 arcminutes (Jarrett et al., 2000). A search within 0.2 arcminutes in the ALLWISE source catalogue: WISEA J131752.27-210338.7 object type Infrared source, separation arcminutes (0.148) (Cutri et al., 2013).

© University of Venda

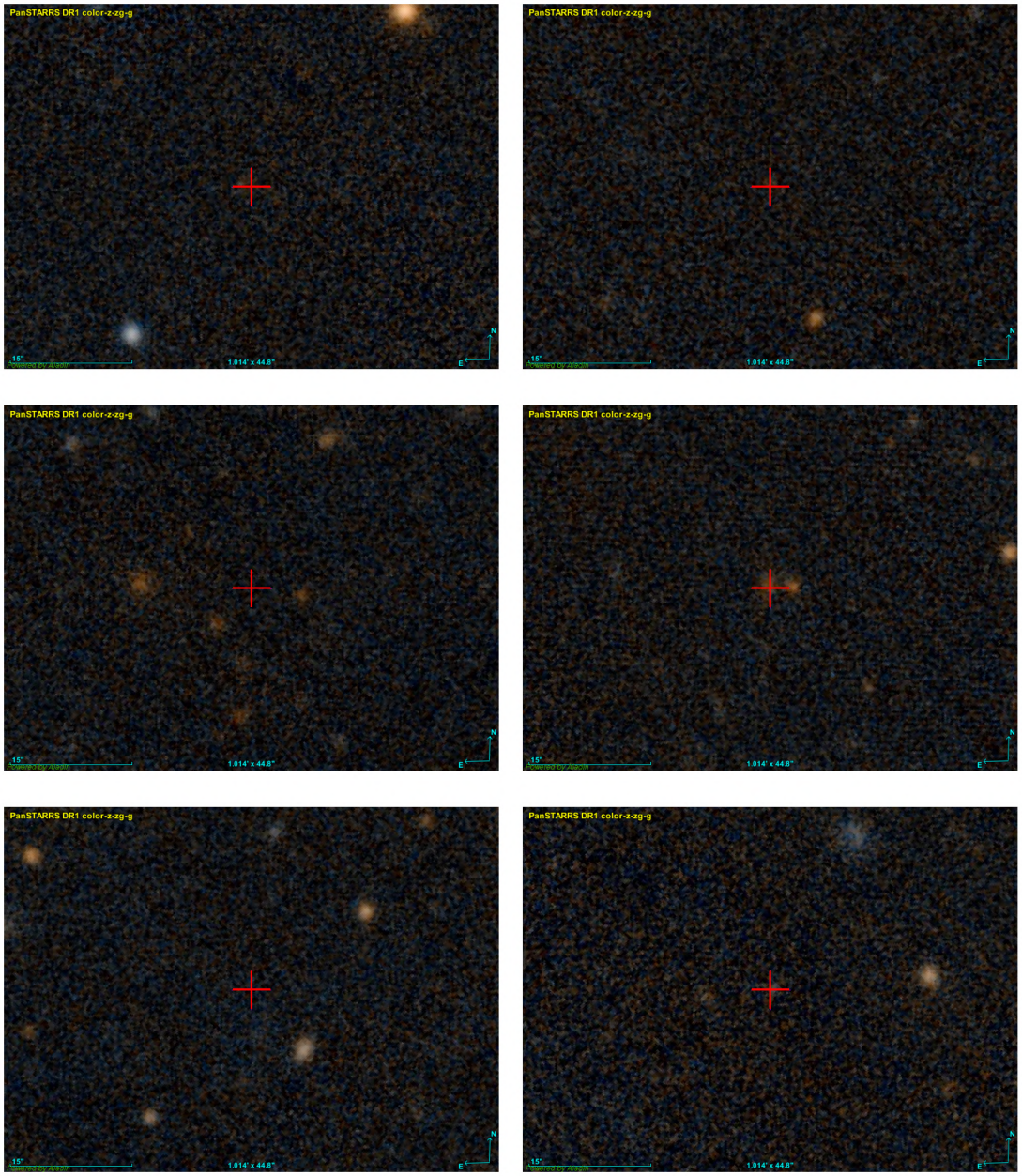


Figure 3.13: The panel presents optical images from the Pan-STARRS catalogue for the selected sources. The first panel on the left represents SRC74654, while the right panel shows SRC75133. The middle panel contains SRC73087 (left) and SRC73395 (right), and the final panel displays SRC74898 (left) and SRC74455 (right). Each source is marked at its central position with a red cross. The images measure 1 arcminute by 45 arcseconds, with arrows in the bottom right corner indicating the sky direction, where "N" denotes North and "E" denotes East.

© University of Venda

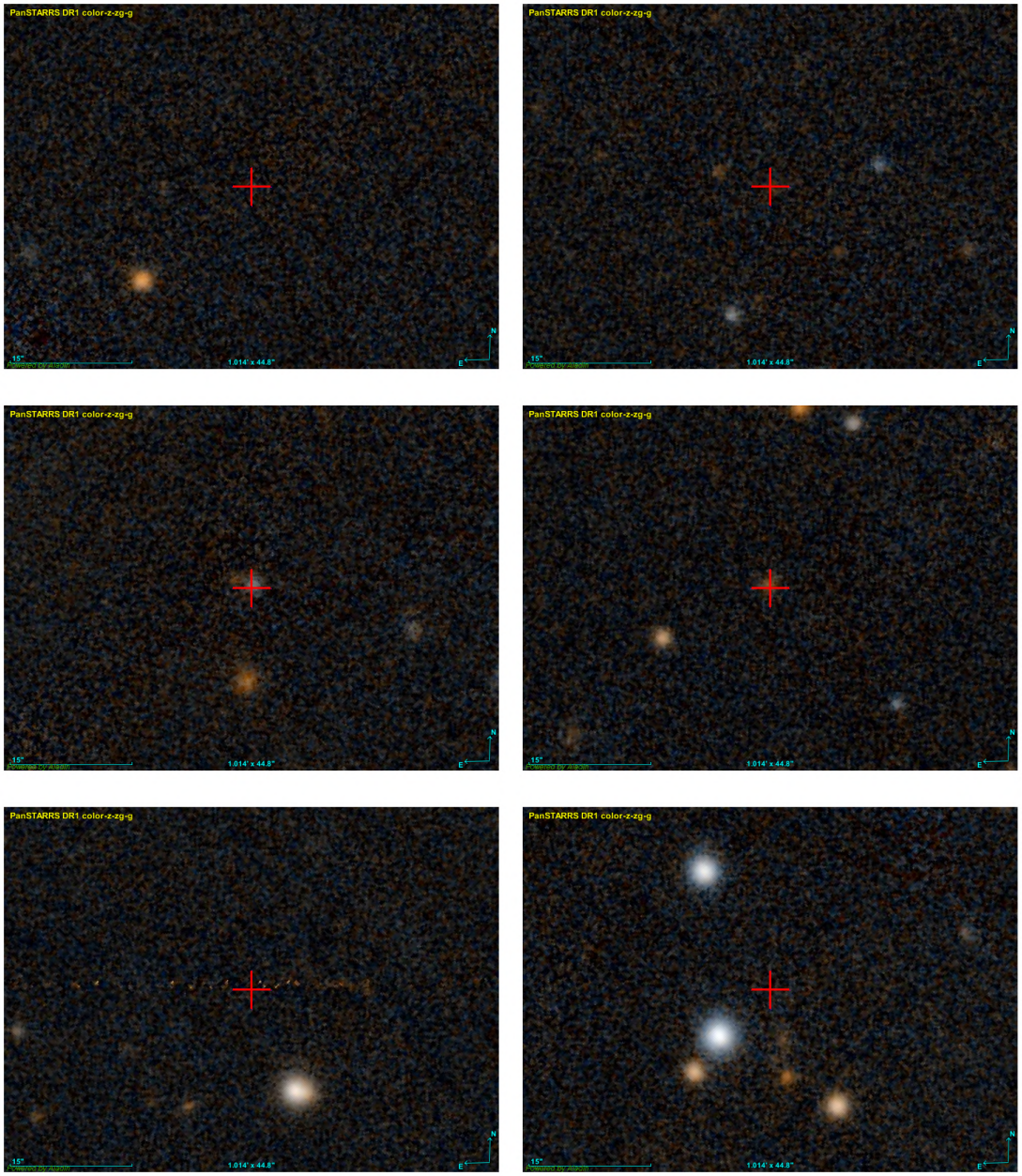


Figure 3.14: The first panel presents optical images from the Pan-STARRS catalogue, with SRC75267 on the left and SRC73326 on the right. The middle panel displays SRC73612 (left) and SRC75046 (right), while the final panel shows SRC72807 (left) and SRC74685 (right). Each source is marked at its central position with a red cross. The images measure 1 arcminute by 45 arcseconds, with arrows in the bottom right corner indicating the sky's orientation, where "N" denotes North and "E" denotes East.

© University of Venda

University of Venda
Creating Future Leaders

Chapter 4

Results for the NGC 1566 field

NGC 1566 is the brightest spiral galaxy in the Dorado group, located approximately 21 Mpc away (Kilborn et al., 2005). It is a nearly face-on $\mathtt{SAB}_{(s)ab}$ type spiral with a well-studied variable active nucleus. As one of the brightest ($V \approx 10.0\,\mathrm{m}$) and closest AGN-hosting galaxies in the Southern Hemisphere (Oknyansky et al., 2019), NGC 1566 serves as an important target for studies of active galactic nuclei and nuclear variability. NGC 1566 is a low-luminosity AGN classified as a Seyfert, though its exact classification between Seyfert 1 and Seyfert 2 varies in the literature (Combes et al., 2014). Its nuclear spectrum shifts between Seyfert 1 during active phases and Seyfert 2 during minimum activity (Ochmann et al., 2024). The galaxy exhibits typical Seyfert 1 features, including a bright central point source, relatively broad [FeII] line emission in the Broad Line Region, and variability on timescales of month. NGC 1566 consists of 10 different epochs, and the observations were conducted between 21 October 2020 to 02 November 2020. The right ascension (J2000.0) of the galaxy is 04h 20m 00.42s, and the declination (J2000.0) of the galaxy is $-54°56'16.1''$.

The analysis results of the NGC 1566 galaxy are shown in this chapter. It starts with the distribution of variability parameters in Section 4.1. Sections 4.2 and 4.3 then analyse the light curves and snapshot images of variable sources identified with TraP. The search for multi-wavelength equivalents is finally described in Section 4.5; each identified source is discussed in detail along with their characteristics.

4.1 Variability parameters η_ν and V_ν

Figure 4.1 shows a distribution of the two statistical variability parameters: η_ν (x-axis) and V_ν (y-axis). The calculated values were $\eta_\nu = 270.38$ and $V_\nu = 0.28$. A total of 4258 sources with variability metrics were identified, each assigned a unique running catalogue number. To characterise these sources, a plot of η_ν against V_ν was created to show the distribution of sources

© University of Venda

that illustrate how the data looks in terms of population. I used 2σ for either V_ν or η_ν and variable sources were defined as sources that showed more significant variability than the 2σ offset from the (η_ν and V_ν). The focus was on sources above the solid black diagonal line, where 11 sources represented by different colours and shapes were investigated and considered variable and transient sources. These sources, considered outliers, had high η_ν and V_ν values, suggesting possible variability or transient events. The sources marked in green were not investigated further, however, their radio images and light curves were visually inspected in 10 epochs, and their light curves are presented in Appendix B. Sources below the black diagonal line and marked in black were not investigated because the study by (Rowlinson et al., 2022) considered outliers as variable sources. Variable sources were sources that exhibited more significant variability than the 2σ offset from the (η_ν and V_ν) distributions. One transient source (SRC76717) and 10 variable sources were identified in this galaxy. Visual inspection of the light curve and images confirmed it as a transient source, and more details of sources' counterparts in multi-wavelength are discussed in Section 4.5. Their radio images showed a point source at each epoch, with brightness variations observed in their light curves.

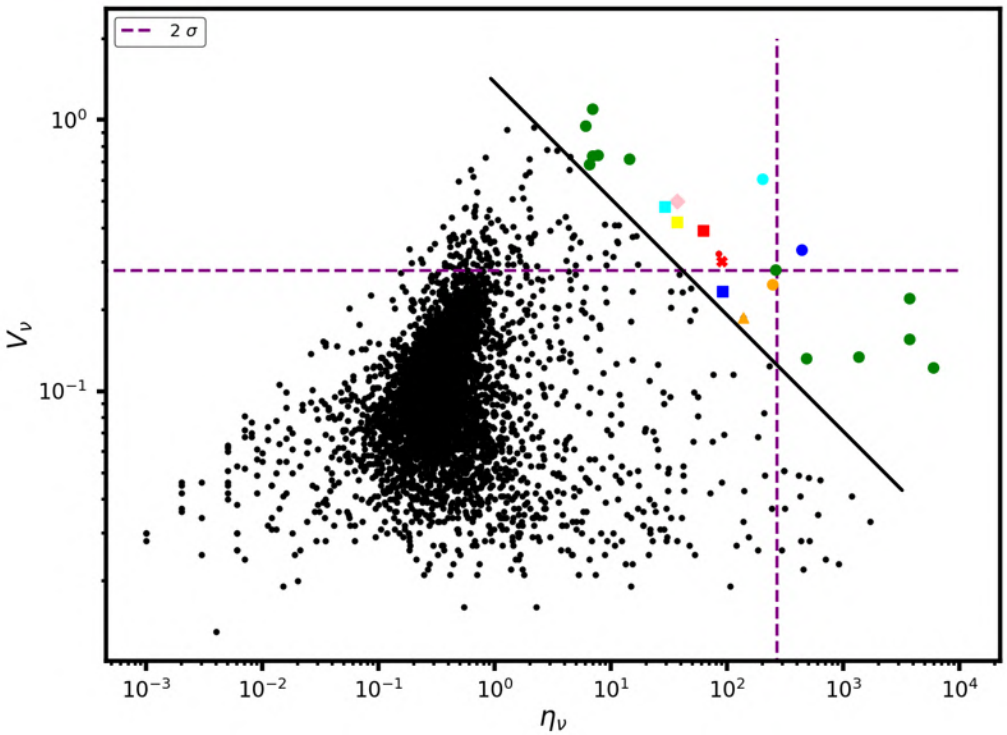


Figure 4.1: The variability parameters for all of the sources detected in the field NGC 1566, the different colours show the 10 variable sources and 1 transient marked by square which is cyan in colour for colour (see; Table 4.1). The black sources were not investigated. The dashed purple lines show the 2σ thresholds used for filtering these parameters, $\eta_\nu = 270.38$ for and $V_\nu = 0.28$.

© University of Venda

Table 4.1: Characteristics of variables and transient sources identified in Figure 4.1, including their ID, position (RA and DEC), variability metrics, colour, and shape.

ID	RA (hh:mm:ss.s)	DEC (dd:mm:ss.s)	η_ν	V_ν	Colour	Shape
79674	04h17m27.2s	$-55°13'07.8''$	438.21	0.33	blue	o (circle)
77927	04h20m28.6s	$-55°10'47.2''$	259.71	0.28	orange	o (circle)
78411	04h17m14.4s	$-54°39'23.4''$	89.69	0.30	cyan	o (circle)
79948	04h19m54.1s	$-55°23'13.6''$	200.40	0.61	orange	^ (triangle up)
76861	04h23m16.8s	$-55°03'21.3''$	91.63	0.23	blue	s (square)
79765	04h17m14.4s	$-54°39'23.4''$	89.69	0.30	red	x (cross)
77880	04h20m50.6s	$-55°14'29.9''$	84.13	0.32	red	o (circle)
79920	04h16m44.7s	$-54°45'34.4''$	61.99	0.39	red	s (square)
79328	04h18m12.3s	$-55°15'04.9''$	36.77	0.42	yellow	s (square)
79364	04h18m12.3s	$-55°04'08.2''$	36.92	0.50	pink	D (diamond)
76717	04h24m01.1s	$-55°12'22.5''$	29.13	0.48	cyan	s (square)

© University of Venda

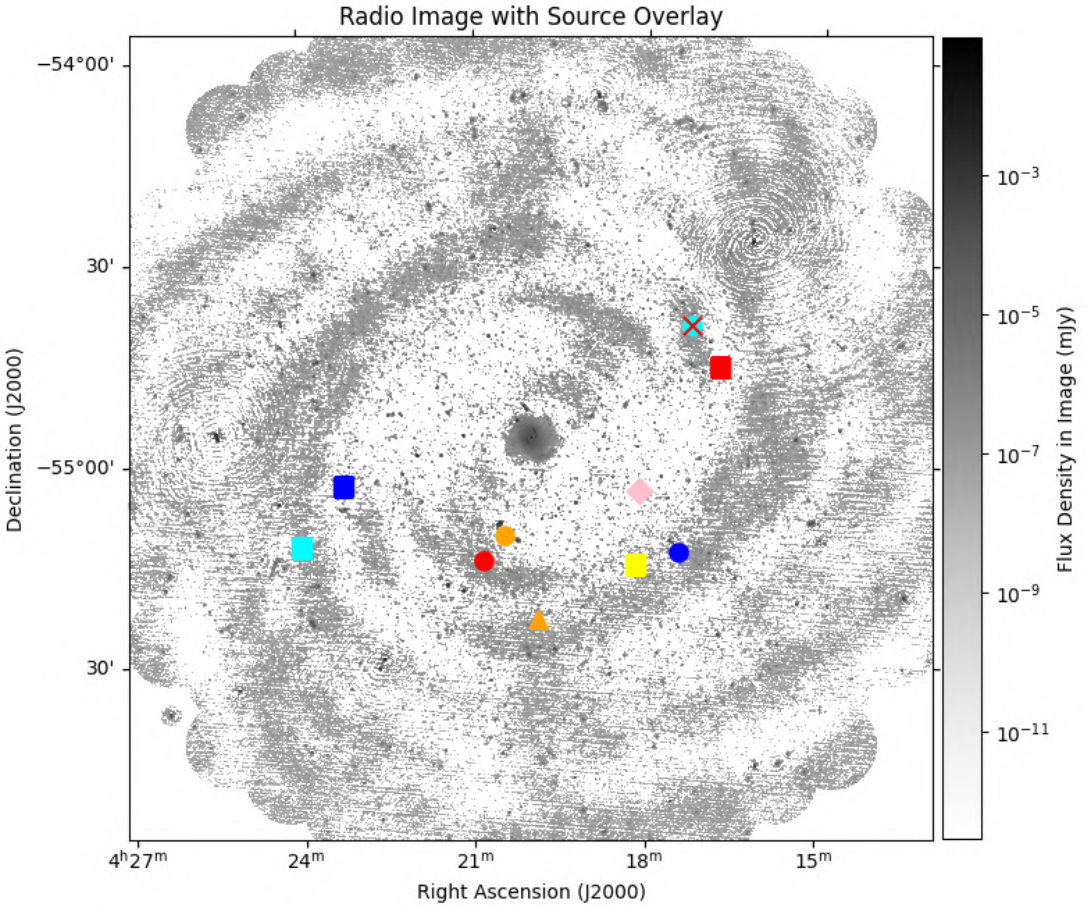


Figure 4.2: MeerKAT SDP image of the field of NGC 1566. The sources marked in different shapes and colours denote variable sources as listed in Table 4.1. One source is marked with a cross to show visibility because it is on top of another source.

© University of Venda

4.2 Light curves of transient and variable sources

The light curves presented in Figures 4.3 and 4.4 illustrate the flux density over time of the variable sources identified in Figure 4.1, revealing significant variability among all the observed sources. Each plot corresponds to a distinct source, identified by its unique ID shown in Table 4.1. The light curves indicate noticeable fluctuations in flux density. The observed variability in flux over time implies that these radio sources could be linked to active astrophysical phenomena, such as variable stars, AGN or transient events. Further investigation into these sources can include searching for other wavelength observations. The light curve of the transient source, SRC76717, is shown in Figure 4.3 marked as "ID 76717". Section 4.5 discusses more sources' details. Each source is discussed in detail in Section 4.5.

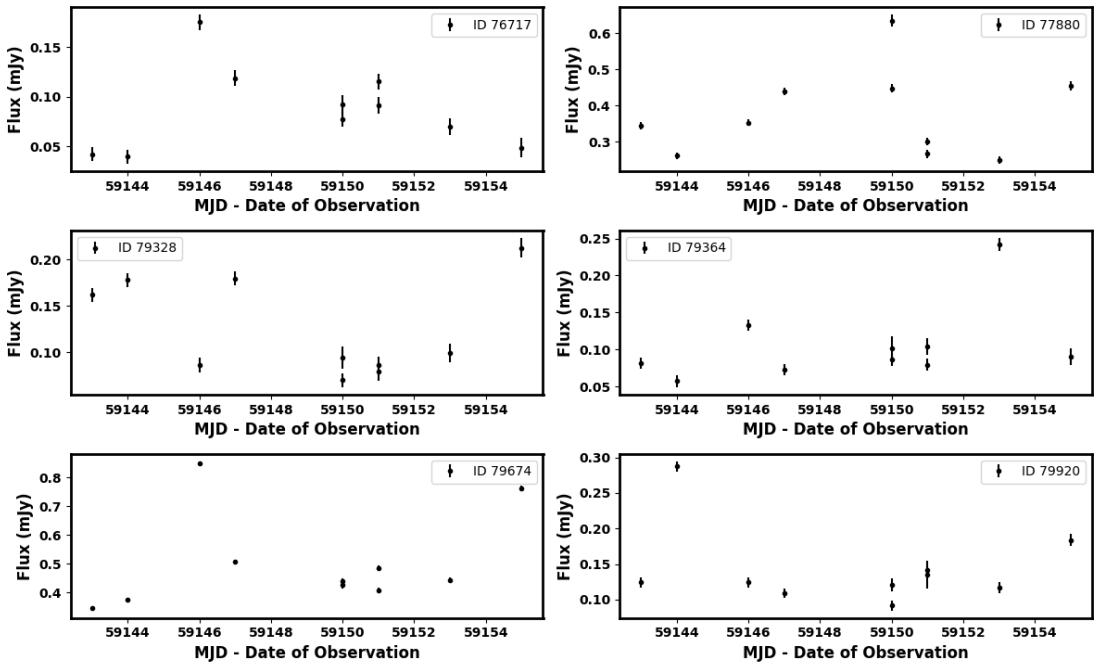


Figure 4.3: The light curves from TraP of variable sources identified in Figure 4.1, with unique IDs: 76717, 77880, 79328, 79364, 79674 and 97720. Uncertainty measurements are too small to be visible on some light curves. The flux is plotted in mJy along with the observation date in MJD.

© University of Venda

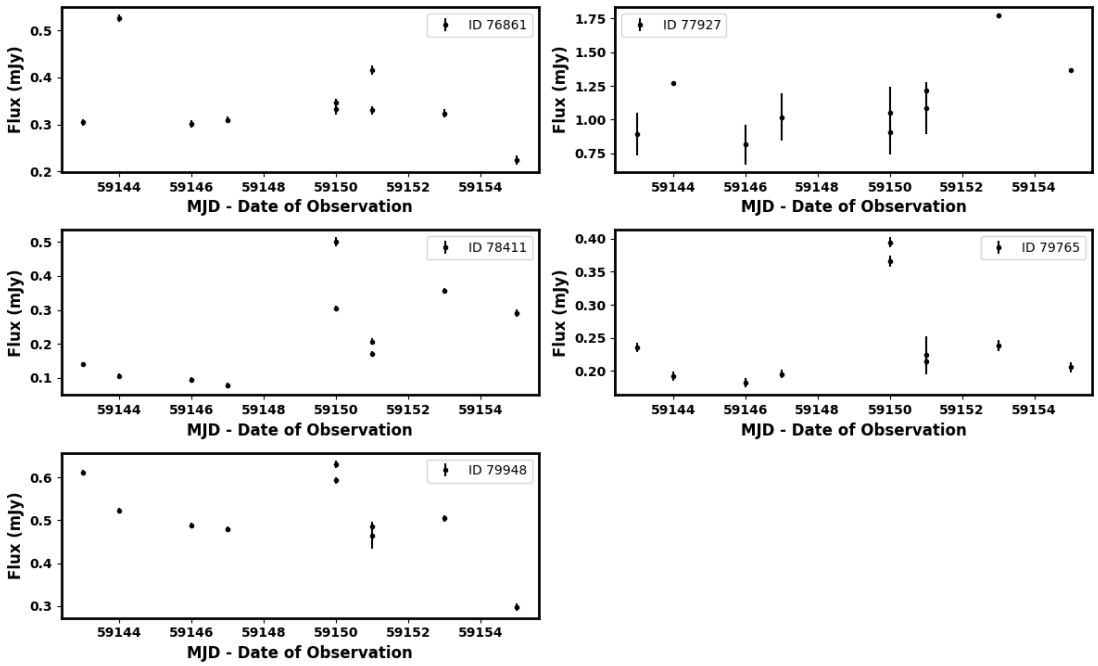


Figure 4.4: The light curves from TraP of variable sources identified in Figure 4.1, with their corresponding Unique ID sources 76861, 77927, 78411, 79765 and 79948. Uncertainty measurements are too small to be visible on some light curves. The flux is plotted in mJy along with the observation date in MJD. The brightest source is SRC77927, has a peak flux of 1.7690 mJy.

4.3 Snapshots of variable sources identified in NGC 1566

Figures 4.5 to 4.8 Show snapshot images of the 11 sources of transient and radio variables identified in Section 4.1 and also marked in Figure 4.1. The images are arranged chronologically from the top left to the right. Each image is scaled to the same flux density (mJy) per panel for a particular source on a linear scale. Flux variations are visible across epochs. The synthesised beam is located in the bottom left corner of all images. Point Sources: This observation suggests the source is unresolved, indicating it is a point source rather than an extended object. The point source's brightness fluctuations across different epochs imply it is a variable radio source. This variability could result from changes in intrinsic luminosity or interactions with the surrounding medium. Extended Sources: Extended variations caused by changes in the PSF and a source larger than the beam (lower left). True Transient Sources: Transient/Variable classifications are the ones we are specifically searching for, representing point sources with variable light curves. A transient source, identified as SRC76717, is presented in Figure 4.8, represented by the last panel. The flux of the source is observed to change from one epoch to the next. The source is discussed in more detail in Subsection 4.5.11.

© University of Venda

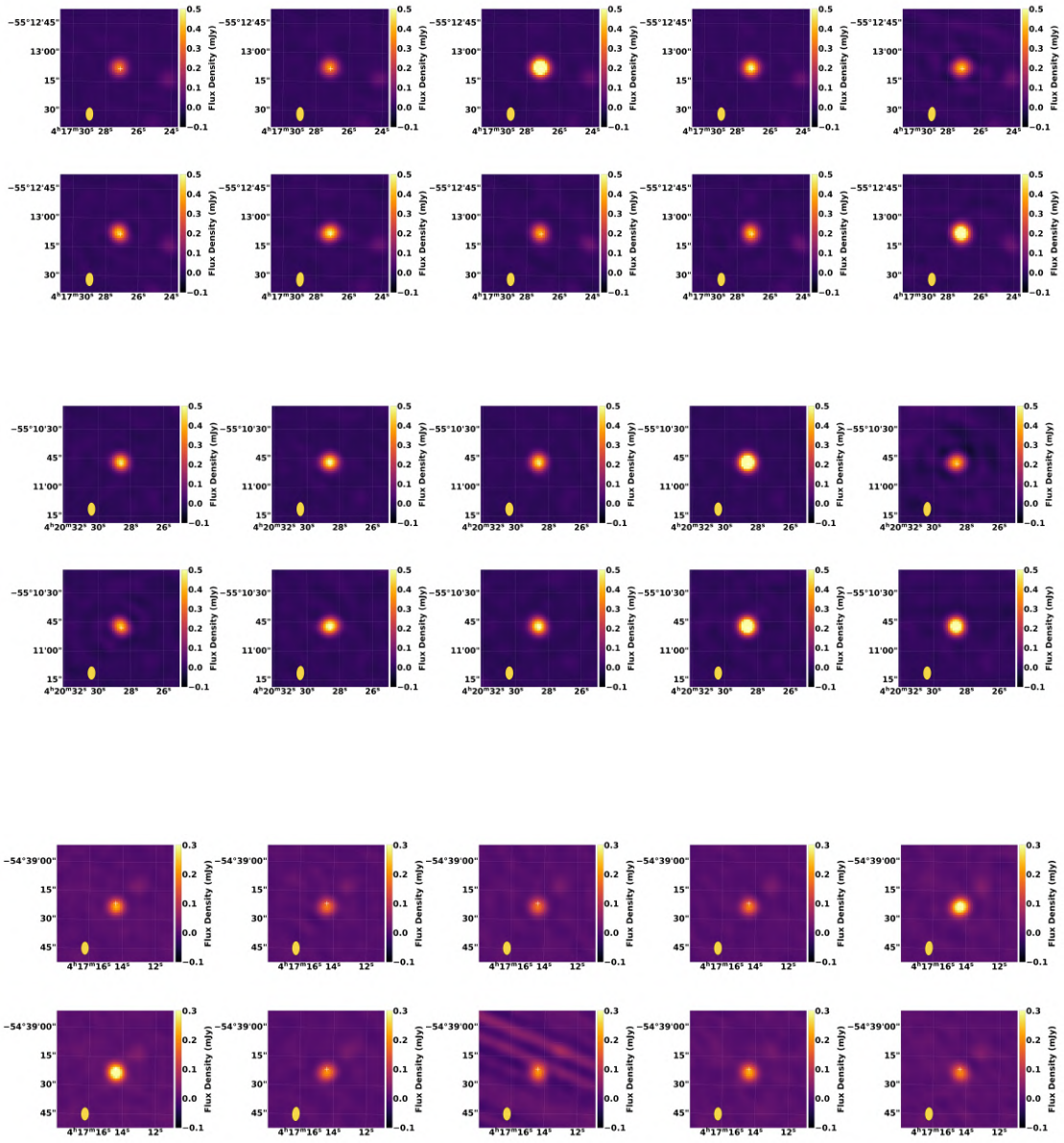


Figure 4.5: Snapshots radio images showing the evolution of each source over the observed ten epochs: The first panel correspond to SRC79674 flux density in image range from -0.1 to 0.5 mJy, the middle panel to SRC77927 where in flux density in image range from -0.1 to 0.5 mJy and the bottom panel to SRC78411 its flux density in image range from -0.10 to 0.30 mJy. The PSF is indicated by the yellow circle in each image in the lower-left corner.

© University of Venda

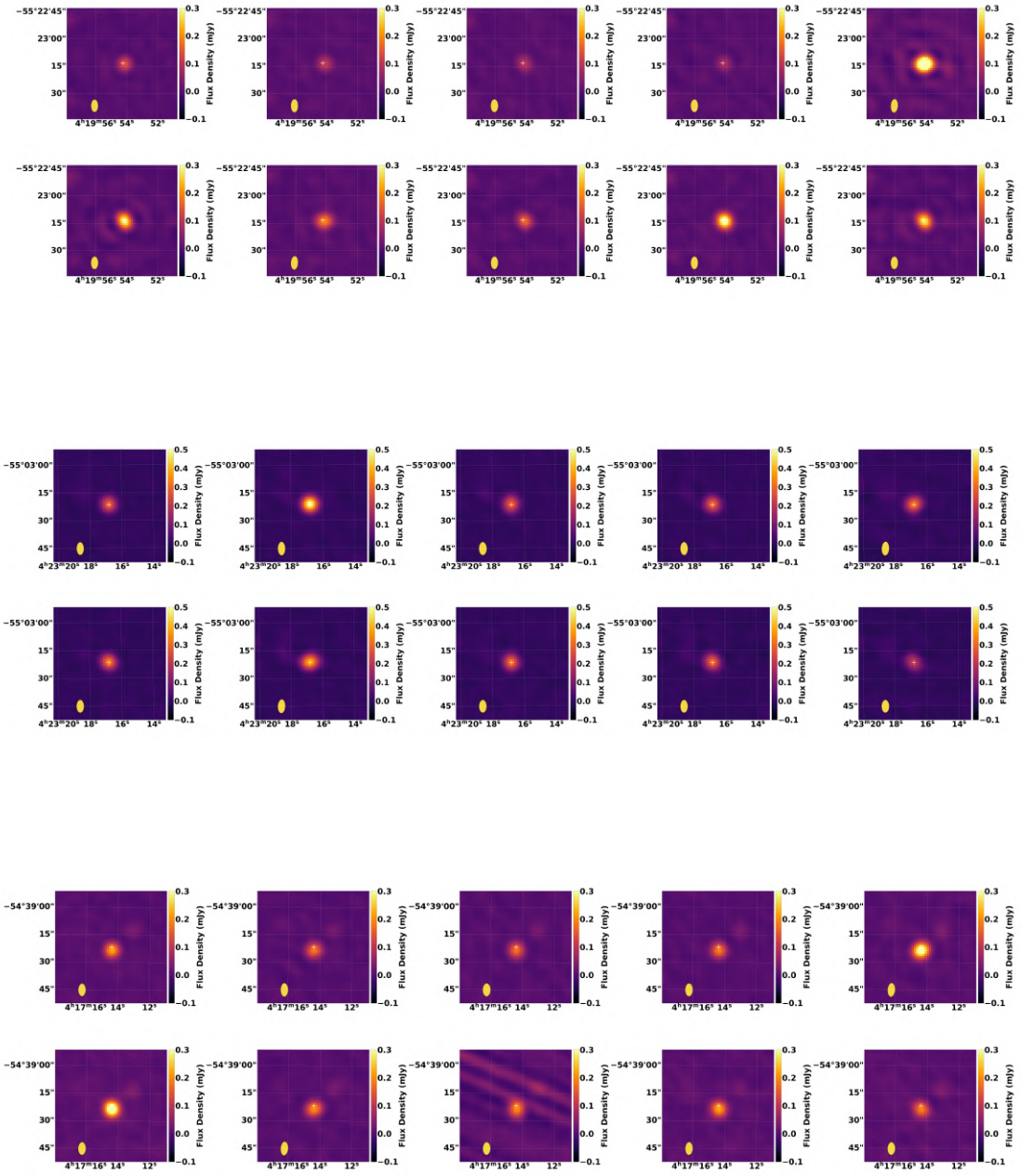


Figure 4.6: Snapshots of radio images showing the evolution of each source over the observed ten epochs: The first panel correspond to SRC79948 flux density in image range from -0.10 to 0.30 mJy, the middle panel to SRC76861 where in flux density in image range from -0.1 to 0.5 mJy and the bottom panel to SRC79765 its flux density in image range from -0.10 to 0.30 mJy. The PSF is indicated by the yellow circle in each image in the lower-left corner. The source can be seen varying in flux from epoch to epoch.

© University of Venda

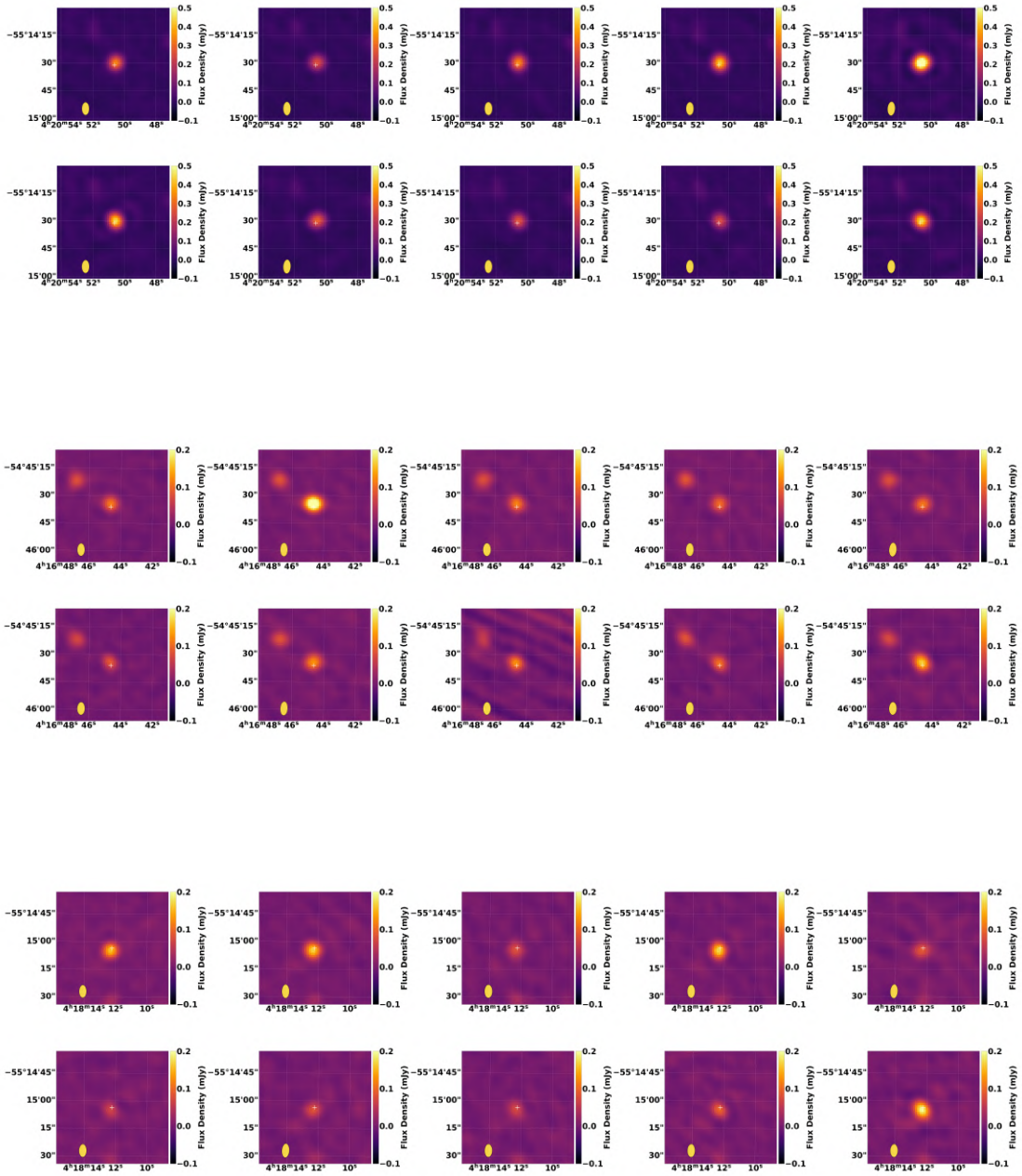


Figure 4.7: Radio image snapshots illustrating each source across the ten observed epochs: The first panel represents SRC77880, the flux density of in the image range from -0.1 to 0.5 mJy, the middle panel represents SRC79920 in the flux density image range of -0.10 to 0.20 mJy, and the bottom panel represents SRC79328 with the flux density in image range of -0.10 to 0.20 mJy. The yellow circle in each image's lower-left corner represents the PSF. The source's flux varies between consecutive epochs.

© University of Venda

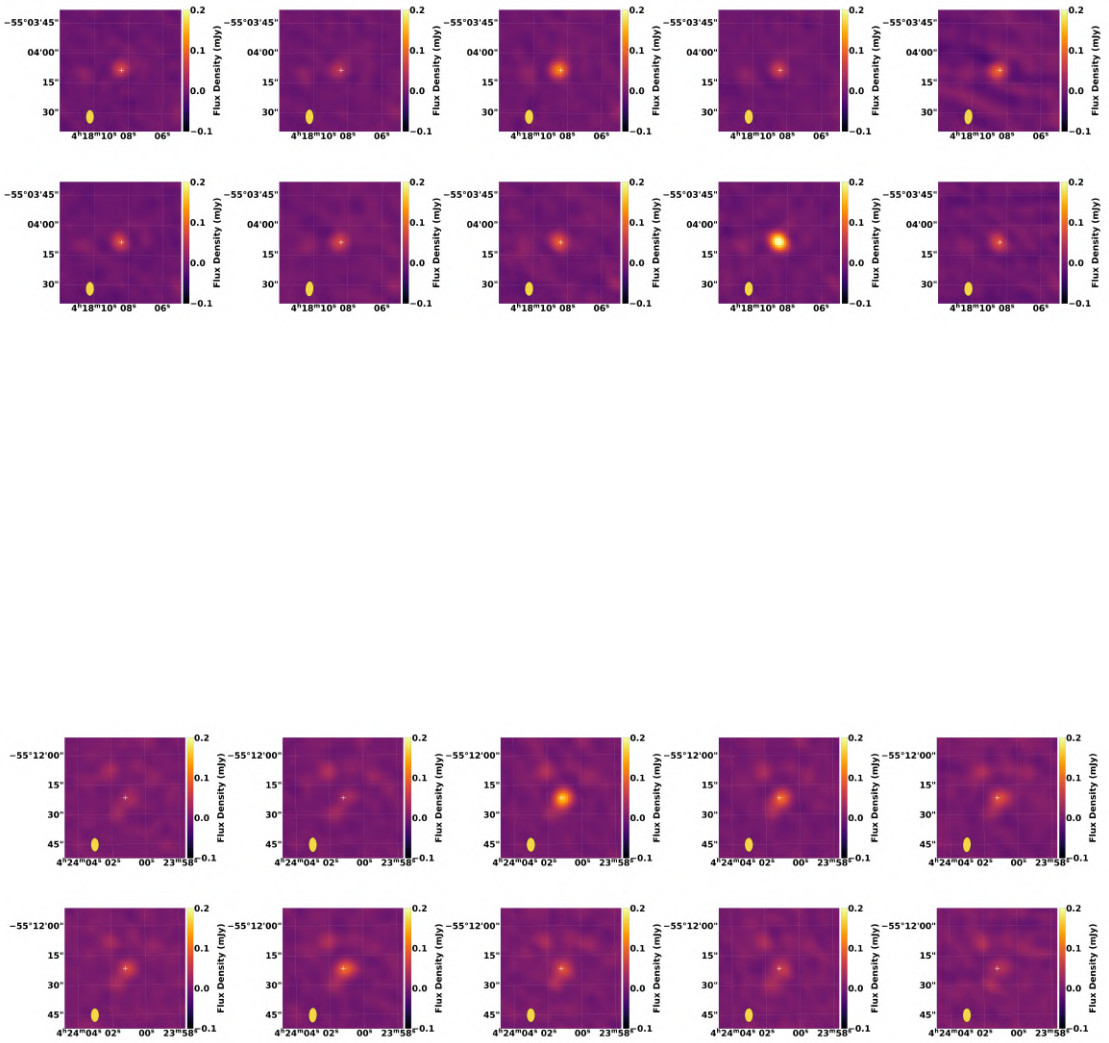


Figure 4.8: Radio images snapshots that demonstrate how each source has changed across the ten epochs that have been observed: First panel: SRC79364, the bottom panel: SRC76717, both flux density in image range is between -0.10 and 0.20 mJy. Each image's yellow circle in the lower-left corner indicates the PSF. The flux of the source is observed to change from one epoch to the next.

© University of Venda

4.4 Correlation of flux density and variability parameter η and V

Figure 4.9 shows the correlation between flux density and the variability parameters η and V for the sources in the dataset in the NGC 1566 galaxy. The left panel shows the relationship between flux density and η, while the right panel presents the correlation between flux density and V. It is evident from the figure that as the flux density increases, η also generally increases. This trend is expected since η represents the statistical significance of the flux variations, which tends to be higher for brighter sources due to their smaller relative uncertainties. In contrast, the right panel shows an inverse relationship between the flux density and V, the variability amplitude. As flux density increases, V tends to decrease, indicating that more significant variations are less likely in the brightest sources. However, this trend should be interpreted cautiously, as flux calibration errors could lead to overestimating the variability in bright sources. The figure supports the expected correlations between flux density and the variability parameters, highlighting that the brightest sources are typically associated with smaller statistical uncertainties and less pronounced variations in flux.

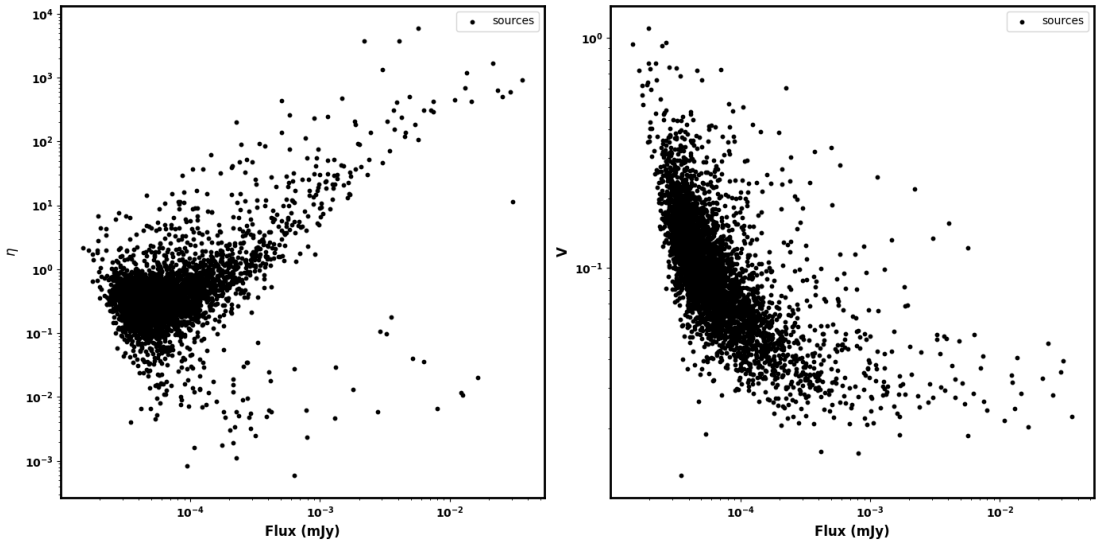


Figure 4.9: The correlation between the flux density and the variability parameters. The left panel shows η vs Flux (mJy), whereas the right panel shows V against flux (mJy).

© University of Venda

4.5 Counterparts across different wavelengths

Counterparts were searched across various wavelengths by examining multiple catalogues in the Vizier database (Ochsenbein et al., 2000). Specifically, we searched for counterparts in the Dark Energy Survey (DES; Choi 2021), Simbad (Wenger et al., 2000), Gaia (Gaia Collaboration et al., 2023), NED (Helou et al., 1991), AllWISE Source Catalog (Wright et al., 2019), and PanSTARRS (Chambers & Pan-STARRS Team, 2016). The DES catalogue is valued for its deeper optical imaging and was used to search for optical counterparts using radio source coordinates and record the R magnitude for the source in Table 4.2. The R magnitude was used to plot the radio flux density (in mJy) versus optical flux density (in mJy) as adapted from the study conducted by (Stewart et al., 2018) to provide an overview of the distribution of different classes of objects.

This approach aimed to collect relevant data for the potential sources, enabling a comprehensive comparison and validation of the findings. Figures 4.11 to 4.12 show the optical counterpart images from DES for the identified sources discussed in Section 4.5. Table 4.2 shows characteristics of 11 potential variable sources identified in Figure 4.1. For each source, the table provides the following information: the ID number, right ascension (RA) in hours, minutes, and seconds, declination (DEC) in degrees, arcminutes, and arcseconds, two variability parameters η_ν and V_ν. The R-band magnitude provides optical brightness and the observed peak flux values with uncertainties.

Table 4.2: Characteristics of 11 selected sources, including Source ID, RA, DEC, variability indices η_ν and V_ν, and observed flux values with uncertainties. The table provides an overview of the variability and flux range for each source.

ID	RA (hh:mm:ss.s)	DEC (dd:mm:ss.s)	η_ν	V_ν	Peak flux (mJy)	Peak flux error (mJy)	R (mag)
79674	04h 17m 27.2s	$-55°13'07.8''$	438.21	0.33	0.8486	0.0042	20.5522
77927	04h 20m 28.6s	$-55°10'47.2''$	259.71	0.28	1.7690	0.0054	19.0524
78411	04h 17m 14.4s	$-54°39'23.4''$	89.69	0.30	0.4994	0.0079	18.8820
79948	04h 19m 54.1s	$-55°23'13.6''$	200.40	0.61	0.6313	0.0052	22.9639
76861	04h 23m 16.8s	$-55°03'21.3''$	91.63	0.23	0.5256	0.0047	23.3892
79765	04h 17m 14.4s	$-54°39'23.4''$	89.69	0.30	0.3944	0.0043	18.8630
77880	04h 20m 50.6s	$-55°14'29.9''$	84.13	0.32	0.6344	0.0097	22.7796
79920	04h 16m 44.7s	$-54°45'34.4''$	61.99	0.39	0.2873	0.0040	19.4378
79328	04h 18m 12.3s	$-55°15'04.9''$	36.77	0.42	0.2127	0.0062	N/A
79364	04h 18m 08.5s	$-55°04'08.2''$	36.92	0.50	0.2418	0.0051	18.1411
76717	04h 24m 01.1s	$-55°12'22.5''$	29.13	0.48	0.1751	0.0045	16.3209

© University of Venda

4.5.1 SRC79674

SRC78411 is located at RA 04h17m27.2s and DEC −55°13′07.8″. The radio light curve shown in Figure 4.3 shows clear variability, with a maximum peak flux density of 0.8486 mJy and minimum flux density of 0.3440 mJy. The flux density measurements are in the range of 0.0039–0.0060 mJy, which is too small to be noticeable on the light curve. The radio image indicates a change in brightness between epochs, as the source appears dim in one epoch and brightens in another, suggesting variability (see Figure 4.5). The first panel represents source SRC79674.

A search in the Simbad database using its coordinates revealed no known association counterpart. However, in the DES, there was a counterpart, the source is associated with DES J041727.13-551307.7, classified as a galaxy, with an r-band (AB) magnitude of 20.6055 (Abbott et al., 2018) and a peak flux of 0.8486 mJy (see Table 4.2). Additionally, a match was identified in the ALLWISE source catalogue as WISEA J041727.12-551307.6 and as GALEXMSC J041727.20-551308.7, an ultraviolet source with a separation of 0.016 arcminutes (Gezari et al., 2013).

Figure 4.10, SRC79674 is marked by a black star, positioned near the optically selected quasar sample (blue dots) close to the FIRST sensitivity limit, indicating that it is likely an AGN.

4.5.2 SRC77927

SRC77927 is located in RA 04h20m28.6s and DEC −55°10′47.2″. The radio light curve for this source, shown in Figure 4.4, displays a variation, with typical flux density measurement uncertainties in the range of 0.0048- 0.1100 mJy. It shows clear variability, with a maximum peak flux density of 1.7690 mJy and minimum flux density of 1.0094 mJy. The radio image indicates a change in brightness between epochs, as the source appears dim in one epoch and brightens in another, suggesting variability (see Figure 4.5); the middle panel represents source SRC77927.

For the source SRC77927, a search of the Simbad database using its coordinates revealed no known counterpart. However, in the DES, there was a counterpart the source is associated with DES J042044.61-552434.7 (Abbott et al., 2018), with an r-band (AB) magnitude of 24.3780 and a peak flux of 1.7690 mJy (see Table 4.2). A match was also identified in the ALLWISE source catalogue as WISEA J042044.62-552435.0 infrared source with a separation of 0.012 arcminutes (Cutri et al., 2013).

In Figure 4.10, a black diamond symbol marks the source SRC77927; it lies in an optical quasar (blue dot). It is likely to be an AGN.

© University of Venda

4.5.3 SRC78411

SRC78411 is located at RA 04h19m54.1s and DEC $-54°39'23.4''$. The radio light curve for this source, shown in Figure 4.4, exhibits a variation, with typical flux density measurement uncertainties in the range of 0.0039- 0.0079 mJy which are too small to be noticeable on the light curve. The light curve shows clear variability, with a maximum peak flux density of 0.4994 and minimum flux density of 0.0780 mJy. Figure 4.5 the last panel represents source SRC78411, which shows the radio image brightness changes across different epochs, indicating variability.

For the source SRC78411, a search of the Simbad database using its coordinates revealed no counterpart. However, in the DES, there was a counterpart; the source is associated with DES J041954.04-552313.6 (Abbott et al., 2018), with an r-band (AB) magnitude of 23.0164 and a peak flux of 0.4994 mJy (see Table 4.2). A source was also identified in the ALLWISE source catalogue as GALEXMSC J041954.18-552310.0 Ultraviolet source with a separation of 0.061 arcminutes (Gezari et al., 2013).

Figure 4.10, a black plus symbol marks SRC78411. It is positioned where we have GRB and a few X-ray binaries, but the dominant sources are optical quasars, indicating that it is likely an AGN, as it can be traced via the diagonal line (representing the change in optical and radio flux as a function of distance) to the sample of AGN.

4.5.4 SRC79948

SRC79948 is located at RA 04h17m14.4s and DEC $-55°23'13.6''-55°23'13.6''$. The light curve for this source, illustrated in Figure 4.4, demonstrates variations, with flux density measurement uncertainties ranging from 0.0038 to 0.0183 mJy, which are too small to be visible on the curve. The light curve shows clear variability, with a maximum peak flux density of 0.6313 mJy and minimum flux density of 0.2976 mJy. The radio image in Figure 4.6, the first panel represents the source SRC79948, indicates brightness variations across different epochs, showing that the source starts dim and gradually brightens over time, confirming its status as a variable point source.

Searching for the Simbad database counterpart using the source coordinates revealed no known associations. However, a counterpart object was identified in the DES, identified as DES J041637.93-544227.5 (Abbott et al., 2018), with an estimated r-band (AB) magnitude of 20.3012 and a peak flux of 0.6313 mJy, as detailed in Table 4.2. Additionally, a corresponding entry in the ALLWISE source catalogue, WISEA J041638.05-544228.4, is classified as a galaxy, with a separation of 0.063 arcminutes from our target (Cutri et al., 2013). A search within a 0.2 arcminute radius in the Gaia Data Release 2 (Gaia DR2) revealed no associated sources.

Figure 4.10, SRC79948 is marked by a black square near the optically selected quasar sample

© University of Venda

(blue dots) close to the FIRST sensitivity limit, indicating that it is likely an AGN.

4.5.5 SRC76861

SRC76861 is located at RA 04h23m16.8s and DEC −55°03′21.3″. The light curve for this source, illustrated in Figure 4.4, has flux density measurement uncertainties ranging from 0.0040- 0.0064 mJy, which are too small to be visible on the curve. The maximum peak flux density is 0.5256 mJy, and the minimum flux density is 0.2240 mJy. In Figure 4.6, the middle panel represents the radio image of the source SRC76861. It indicates brightness variations across different epochs, confirming its status as a variable point source.

Searching for the Simbad database counterpart using the source coordinates revealed no known associations. However, a counterpart object was identified in the DES, identified as DES J042316.74-550321.2, with an estimated r-band (AB) magnitude of 23.3892 (Abbott et al., 2018) and a peak flux of 0.5256 mJy, as detailed in Table 4.2. Additionally, a corresponding entry in the ALLWISE source catalogue, WISEA J042316.72-550321.6, is classified as the infrared source, with a separation of 0.012 arcminutes from our target (Cutri et al., 2013). A search within a 0.2 arcminute radius in the Gaia Data Release 2 (Gaia DR2) revealed no associated sources.

Figure 4.10, SRC76861 is represented by a black upward triangle. Its position near the FIRST sensitivity limit suggests that it is likely an AGN. This conclusion is supported by the diagonal line in the figure, which illustrates the relationship between optical and radio flux as a function of distance and traces SRC76861 to the AGN sample.

4.5.6 SRC79765

SRC79765 is located at RA 04h17m14.4s and DEC −54°39′23.4″. The light curve for this source, illustrated in Figure 4.4, shows a light curve showing variations over weeks to months, with flux density measurement uncertainties ranging from 0.0037- 0.0163 mJy, which are too small to be visible on the curve. The light curve exhibits clear variability, with a maximum peak flux density of 0.3944 mJy and minimum flux density of 0.1821 mJy. The radio image of the source SRC79765 is represented in Figure 4.6, in the last panel, indicating brightness variations across different epochs, confirming its status as a variable point source.

For the source SRC79765, we searched the Simbad database using the source coordinates but found no known associations. However, we identified a matching object in the DES, identified as DES J041714.30-543923.4 (Abbott et al., 2018), with an estimated r-band (AB) magnitude of 18.9529 and a peak flux of 0.3944 mJy, as detailed in Table 4.2. Additionally, a corresponding counterpart in the ALLWISE source catalogue, WISEA J041714.31-543923.4, is classified as Galaxy, with a separation of 0.009 arcminutes from our target. A search within a

© University of Venda

0.2 arc minute radius in the Gaia Data Release 2 (Gaia DR2) reveals an associated source EDR3 4779235170842511616 (Gaia Collaboration, 2022).

SRC 79765 is marked by a black circle in Figure 4.10 positioned where we have GRB and a few x-ray binaries, but the dominant are optical quasars, indicating that it is likely an AGN, as it can be traced via the diagonal line representation of the change in optical and radio flux as a function of distance) to the sample of AGN.

4.5.7 SRC77880

An object SRC77880 is located at RA 04h20m50.6s and DEC $-55°14'29.9''$. Figure 4.3 presents a light curve that shows variations over weeks to months, with flux density measurement uncertainties ranging from 0.0056 to 0.0076 mJy, which are too small to be visible on the curve. The light curve shows clear variability, with a maximum peak flux density of 0.6344 mJy and minimum flux density of 0.2496 mJy.The radio image in Figure 4.7, the first panel represents the source SRC77880. It reveals brightness variations across different epochs, confirming that SRC 77880 is a variable point source

A search for the counterpart in the Simbad database using the source coordinates revealed no known associations; however, a counterpart object was identified in the DES, as DES J042050.48-551430.0, with an estimated r-band (AB) magnitude of 23.0708 and a peak flux of 0.6344 mJy, as detailed in Table 4.2. Additionally, the ALLWISE catalogue shows a counterpart infrared source, WISEA J042050.52-551429.6, located 0.011 arcminutes from our target (Cutri et al., 2013).

SRC77880 is marked with a cross in Figure 4.10 and is near the FIRST survey's sensitivity limit, suggesting it is likely an Active Galactic Nucleus (AGN), as it aligns with the diagonal line representing the relationship between optical and radio flux as a function of distance for AGN.

4.5.8 SRC79920

SRC79920 is located in RA 04h16m44.7s and DEC $-54°45'34.4''$. Figure 4.3 shows a light curve that varies over a period of weeks to months. The uncertainties in the flux density measurement range from 0.0038 to 0.0114 mJy, which are too small to be seen on the curve. The light curve shows clear variability, with a maximum peak flux density of 0.2873 mJy and minimum flux density of 0.0916 mJy. As a variable point source, the radio image in Figure 4.7, the middle panel represents the source SRC79920. It shows variation in brightness over multiple epochs, indicating that it was extremely bright once or at a single epoch.

Searching for the Simbad database counterpart using the source coordinates revealed no known associations; However, a counterpart object was identified in the DES as J041644.38-544536.9. This object has an r-band (AB) magnitude of 19.4457 and a peak flux of 0.2873 mJy, as shown

© University of Venda

in Table 4.2. Furthermore, a counterpart was found in the ALLWISE source catalogue WISEA J041644.46-544536.4, which is categorised as a Galaxy and is located 0.074 arc minutes away from our target. A search in the Gaia Data Release 2 (Gaia DR2) at a radius of 0.2 arcminutes finds an associated source EDR3 4778857793540101760, with a total Proper Motion (pm) of 24.589 mas/yr (Gaia Collaboration, 2022).

Figure 4.10 shows a source SRC79920 with a black pentagon. It is situated where GRBs and a few x-ray binaries are present, but optical quasars predominate as the diagonal line can trace them.

4.5.9 SRC79328

SRC79328 is located at RA 04h18m12.3s and DEC $-55°15'04.9''$. Figure 4.3 shows light curves with visible flux density measurement error bars that fluctuate over periods of weeks to months. The light curve shows clear variability, with a maximum peak flux density of 0.2127 mJy and minimum flux density of 0.0697 mJy. The uncertainties in the flux density measurement range from 0.0042 to 0.0068 mJy, which are too small to be seen on the curve. Figure 4.7, depicts the last panel represents the source SRC79328 and shows a radio image that confirms the source's classification as a variable point source by showing fluctuations in brightness throughout various epochs.

The search for the source SRC79328 in the Simbad database using its coordinates yielded no counterpart. Additionally, no corresponding counterpart source was found in the DES. Table 4.2 shows that the r-band (AB) magnitude N/A had no counterpart and a peak flux of 0.2127 mJy. Moreover, no match is found in the WISEA catalogue. No corresponding source is found when searching in the Gaia Data Release 2 (Gaia DR2) within a radius of 0.2 arcminutes.

Since there was no optical counterpart for the source in the DES, this source has no optical versus radio flux density diagram.

4.5.10 SRC79364

SRC79364 is located at RA 04h18m8.5s and DEC $-55°04'08.2''$. Figure 4.3 shows light curves varying from weeks to months, With flux density measurement uncertainties ranging from 0.0043 to 0.0092 mJy, with a maximum peak flux density of 0.2418 mJy and minimum flux density of 0.0568 mJy. The radio image in Figure 4.8, the first panel represents the source SRC79364, shows brightness changes across multiple epochs.

The Simbad database was searched using the source coordinates for SRC79364, but no known associations were found. As shown in Table 4.2, we found a counterpart in the DES, identified as DES J041808.42-550408-3 (Abbott et al., 2018). Its r-band (AB) magnitude is 18.2087, and

© University of Venda

its peak flux is 0.2418 mJy. Furthermore, WISEA J041808.44-5504082.3, a matching source in the ALLWISE source catalogue, is categorised as a Galaxy source and is located 0.010 arc minutes away from our target (Maddox et al., 1990). An associated source, EDR3 EDR3 4778798218049443712, classified as Galaxy, is found in the Gaia Data Release 2 (Gaia DR2) within a 0.2 arcminute radius.

SRC79364 is identified by a black side right triangle symbol in Figure 4.10. It is located in the region where GRBs and a few x-ray binaries are present, but optical quasars are the dominant source, as can be traced by diagonal lines.

4.5.11 SRC76717

SRC76717 is located at RA 04h24m1.1s and DEC $-55°12'22.5''$. A radio light curve with a visible error bar is shown in Figure 4.3. Flux density measurement uncertainties range from 0.0041 to 0.0056 mJy, with a maximum peak flux density of 0.1751 mJy and minimum flux density of 0.0395 mJy. The radio image in Figure 4.8, the last panel represents the source SRC76717, illustrates its detection, clearly shows its significance as a variable point source, and was exceptionally bright once or at one epoch. The source was not present during the first two epochs and became more noticeable during the third epoch. The source has 9 points of detection.

Figure 4.10 shows a black downward triangle sign identifying SRC79364. If one were to trace it via a diagonal line, it would be situated in an area dominated by stellar sources, with a few x-ray binaries and supernovae present. A counterpart on DES associated with DES J042401.04-551222.2 is 0.001 arcsec away from SRC76717 and has an R(mag) of 16.1369 (Choi, 2021).

Radio coordinates of source SRC76717 were used to search the Simbad database for a counterpart, leading to the identification of the known association UCAC4 174-004510 — Eruptive Variable star, with a total proper motion (pm) of 41.500 mas/yr (Gaia Collaboration, 2020). At Transiting Exoplanet Survey Satellite (TESS) Input Catalog - v8.0 (TIC-8) source was found and classified as a star, with a period of 5.8911 and distance of 48 parsecs away from Earth (Doyle et al., 2019), which relates to the rotational period of a specific M dwarf star. This rotational period is derived from periodic brightness variations in the light curve caused by star spots rotating in and out of view as the star spins. Such periodic modulations provide crucial insights into the star's activity and magnetic field properties. Stars tend to spin down as they age due to angular momentum loss via stellar winds. A rotational period of ~ 5.9 days suggests the star is relatively young but older than ultra-fast rotators (e.g., periods < 1 day), potentially falling in the middle of its pre-main-sequence or early main-sequence evolution (Doyle et al., 2019). The rotation period can indicate the level of magnetic activity in the star. Generally, younger stars or those with shorter rotation periods tend to exhibit more magnetic activity, which can lead to increased flare occurrences. This is particularly relevant for M dwarfs, which are known for their

© University of Venda

magnetic fields and flare activity. In the context of the study conducted by (Doyle et al., 2019), the researchers found no correlation between flare occurrence and rotational phase for M dwarfs, indicating that flares might not be directly linked to large starspots as previously thought.

There was a countpart in 2MASS (2Micron All-Sky Survey) the study of (Shan et al., 2017) associated with 2MASS J04240094-5512223, spectral type: M2.5 and distance: approximately 46 ± 2 parsecs. This classification indicates that it is a low-mass star, specifically a late-type dwarf, characteristic of stars in the M spectral class. Stars of this type are generally cooler and less luminous than earlier spectral types, contributing to the study of low-mass stellar populations within young moving groups. J04240094-5512223 provides valuable insights into stellar formation and evolution. Astronomers can better understand young stellar populations' dynamics and binarity's role in stellar evolution processes by studying their properties.

The study by (Kraus et al., 2014) reports the identification and confirmation of 129 new members of the Tucana-Horologium (Tuc-Hor) moving group, a young stellar population estimated to be approximately 40 million years old and located about 40 parsecs from Earth. Among the objects studied, 2MASS J04240094-5512223 was included and analysed in detail. The properties of 2MASS J04240094-5512223 listed in Table 2 of (Kraus et al., 2014) are as follows: Radial Velocity ($v_{\rm rad}$) of $19.0 \pm 0.7\,$km/s, Rotational Velocity ($v \sin(i)$) of $6.9 \pm 0.9\,$km/s, Spectral Type (SpT) classified as M2.0, Hα Equivalent Width (EW[Hα]) measured at $-3.54\,$Å, and Lithium Equivalent Width (EW[$\rm Li_{6708}$]) of $21.2\,$mÅ. These properties indicate that the star is a low-mass, cool dwarf in the main sequence or possibly in the pre-main-sequence stage if it is young.

An M2 spectral type corresponds to a low-mass, cool star on the main sequence or in the pre-main-sequence stage if it's young. The relatively low value of $v \sin(i)$ (projected rotational velocity) indicates this star might be rotating moderately for its spectral type. The negative Hα Equivalent Width (EW[Hα]) of $-3.54\,$Å indicates the presence of emission in the Hα spectral line. Lithium Equivalent Width (EW[$\rm Li_{6708}$]) of $21.2\,$mÅ: is a sensitive youth indicator in stars. Its presence in significant amounts in the atmosphere indicates the star is young, as lithium burns out rapidly in stellar interiors once the star ages and its convection zone becomes deep enough. In the DES, a counterpart was found associated with J042401.04-551222.2 (Abbott et al., 2018), as indicated in Table 4.2. At $0.1751\,$mJy, its maximal flux density, its r-band (AB) magnitude is 16.1369.

This section will provide a plot showing a relationship between radio and optical flux between known variable sources and transients. The study was adapted from (Stewart et al., 2018). At the end of this section, I will show the optical counterpart images from DES.

Figure 4.10 shows a density plot of astronomical objects plotted against their radio flux density (in mJy) on the y-axis and optical AB magnitude (in mag) on the x-axis. The plot includes

© University of Venda

background diagonal dashed lines representing the slope of a constant radio-to-optical flux ratio, along with lines indicating survey limits for the FIRST and SDSS surveys. These lines represent constant radio-to-optical flux density ratios. The objects that lie on or near these lines have similar ratios, indicating a consistent relationship between their radio and optical emissions.

FIRST Limit (Horizontal Line) This is the sensitivity limit of the FIRST radio survey, indicating that sources below this line have radio flux densities lower than the FIRST survey's detection threshold. SDSS Limits (Vertical Lines) The left vertical line at 14 mag marks the SDSS saturation limit. Sources to the left of this line are too bright and might be saturated in SDSS data. The right vertical line at 22 mag marks the SDSS 95% completeness limit. Sources to the right of this line might not be reliably detected in SDSS data (Stewart et al., 2018). Most of our radio sources likely fall under the quasar category are AGN, except for one that occupies a stellar sample.

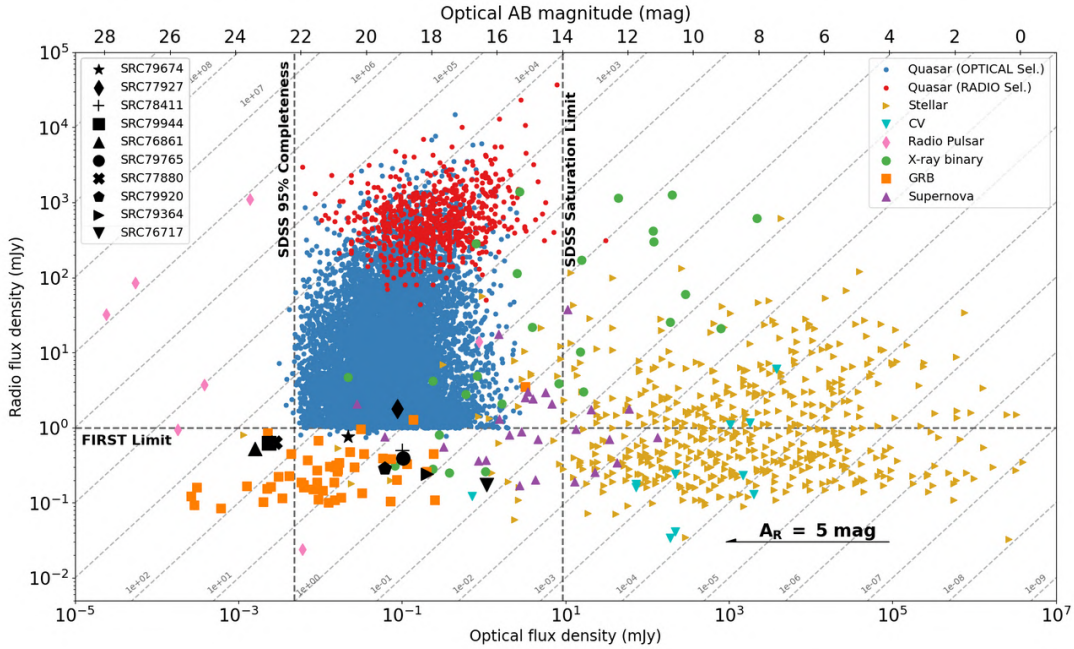


Figure 4.10: Radio versus optical flux density of objects from different classes, adapted from (Stewart et al., 2018), all my sources are represented by black colour with different symbols. Their positions relative to the diagonal dashed lines and survey limits can help identify their classes.

© University of Venda

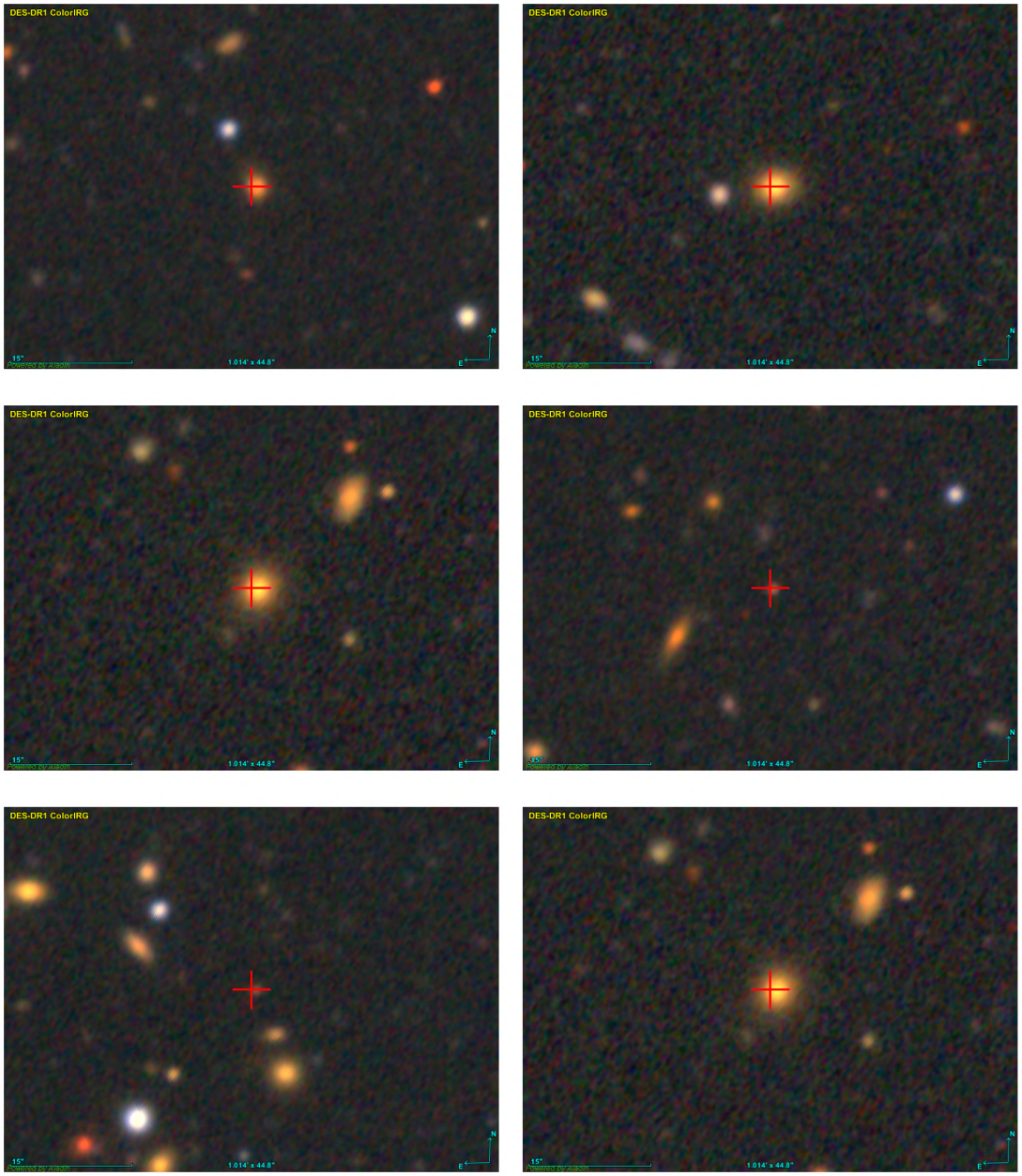


Figure 4.11: The first panel presents optical images from the Dark Energy Survey (DES), with SRC79674 on the left and SRC77927 on the right. The middle panel displays SRC78411 (left) and SRC79948 (right), while the final panel shows SRC76861 (left) and SRC79765 (right). Each source is marked at its central position with a red cross. The images measure 1 arcminute by 45 arcseconds, with arrows in the bottom right corner indicating the sky direction, where "N" denotes North and "E" denotes East.

© University of Venda

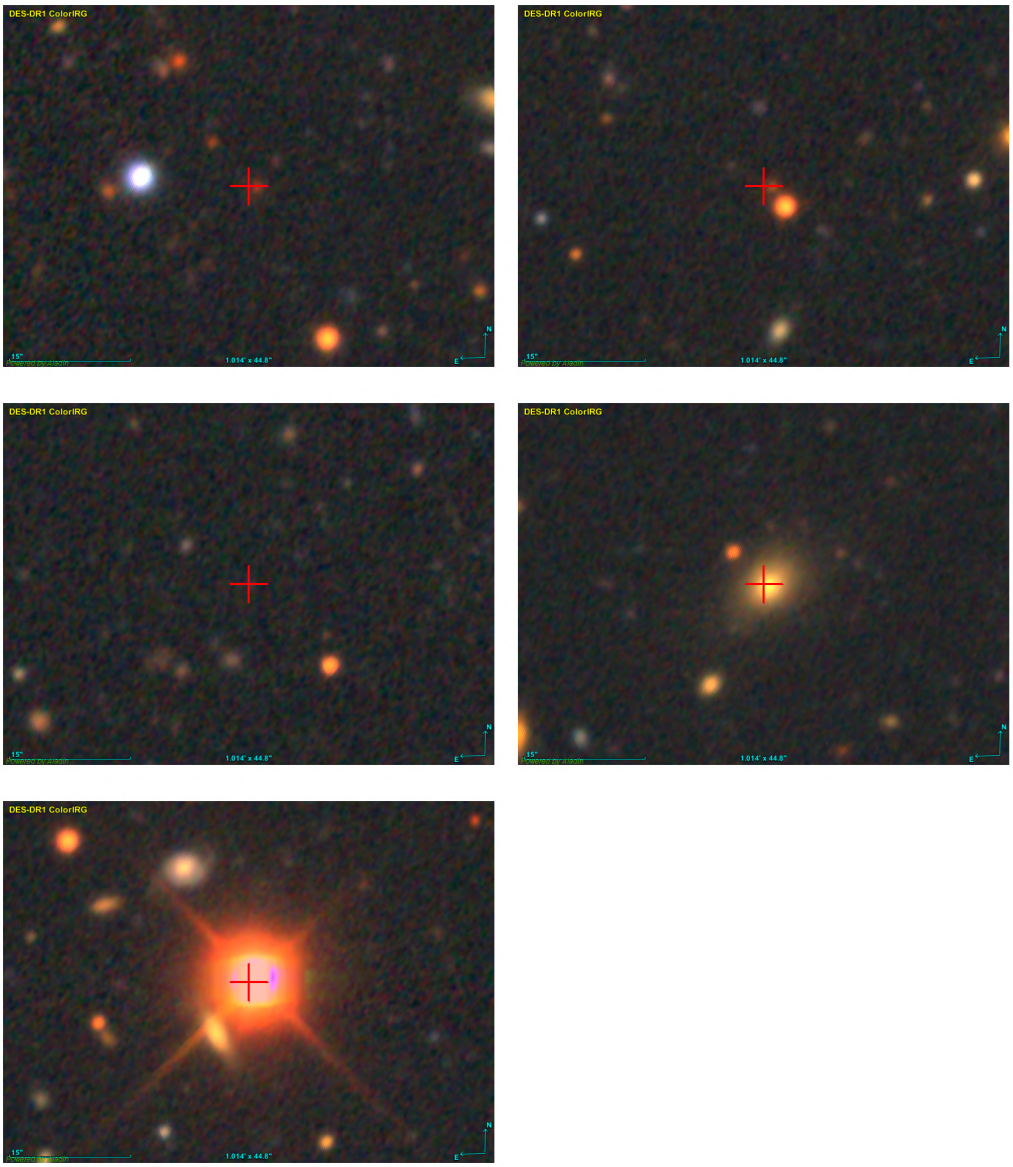


Figure 4.12: The first panel presents optical images from the Dark Energy Survey (DES), with SRC77880 on the left and SRC79920 on the right. The middle panel displays SRC79328 (left) and SRC79364 (right), while the final panel represents SRC76717. Each source is marked at its central position with a red cross. The images measure 1 arcminute by 45 arcseconds, with arrows in the bottom right corner indicating the sky direction, where "N" denotes North and "E" denotes East.

© University of Venda

University of Venda
Creating Future Leaders

Chapter 5

Results for the NGC 1371 field

NGC 1371 is noted for having a low star formation rate (SFR) relative to its stellar mass. This characteristic sets it apart from other galaxies in the MHONGOOSE sample, which are generally more actively forming stars (de Blok et al., 2024). NGC 1371 has also been previously studied for supernova events, such as Supernova 2005ke, which provides insights into stellar phenomena within this galaxy (Immler & Brown, 2005). NGC 1371 consists of 10 different epochs, and the observations were conducted between 31 July 2022 and 09 January 2023. The right ascension (J2000.0) of the galaxy is 03h 35m 01.34s, and the declination (J2000.0) of the galaxy is $-24°55'59.6''$. The analysis results for the NGC 1371 galaxy are shown in this chapter. It starts with the distribution of the variability parameters in Section 5.1. Subsequently, Sections 5.2 and 5.3 analyse the light curves and snapshot images of variable sources identified with TraP. Section 5.5 concludes by providing information on variable sources found and their attributes, as well as the search for multi-wavelength counterparts. Each identified source is discussed in detail.

5.1 Variability parameters η_ν and V_ν

Figure 5.1 shows the distribution of the two parameters of statistical variability: η_ν (x-axis) and V_ν (y-axis). The calculated values were $\eta_\nu = 804.04$ and $V_\nu = 0.24$. A total of 4847 sources with variability metrics were detected with their unique running catalogue number. To characterise these sources, the plot of η_ν against V_ν was plotted, which shows the distribution of sources that tell us how the data looks in terms of population. I used 2σ for either V_ν or η_ν, assuming that it is a well-modelled Gaussian distribution and variable sources were sources that showed more significant variability than the 2σ offset from the (η_ν and V_ν). The sources above the solid black diagonal line represented by different colours and shapes were investigated and considered variables. 9 variable sources were found in this galaxy NGC 1371. These sources, considered as outliers, had high η_ν and V_ν values, suggesting possible variability or transient events.

© University of Venda

The sources marked in green were not investigated further. However, their radio images and light curves were visually inspected in 10 epochs, and their light curves are shown in Appendix C. They were identified as either extended sources, where variability could be attributed to changes in the point spread function (PSF) rather than intrinsic variability, or stable unresolved point sources with consistently flat light curves showing no significant variations within the error bars. Sources below the black diagonal line and marked in black were not investigated because the study by Rowlinson et al. 2022 considered outliers as variable sources that showed more significant variability than the 2σ offset from the (η_ν and V_ν) distributions.

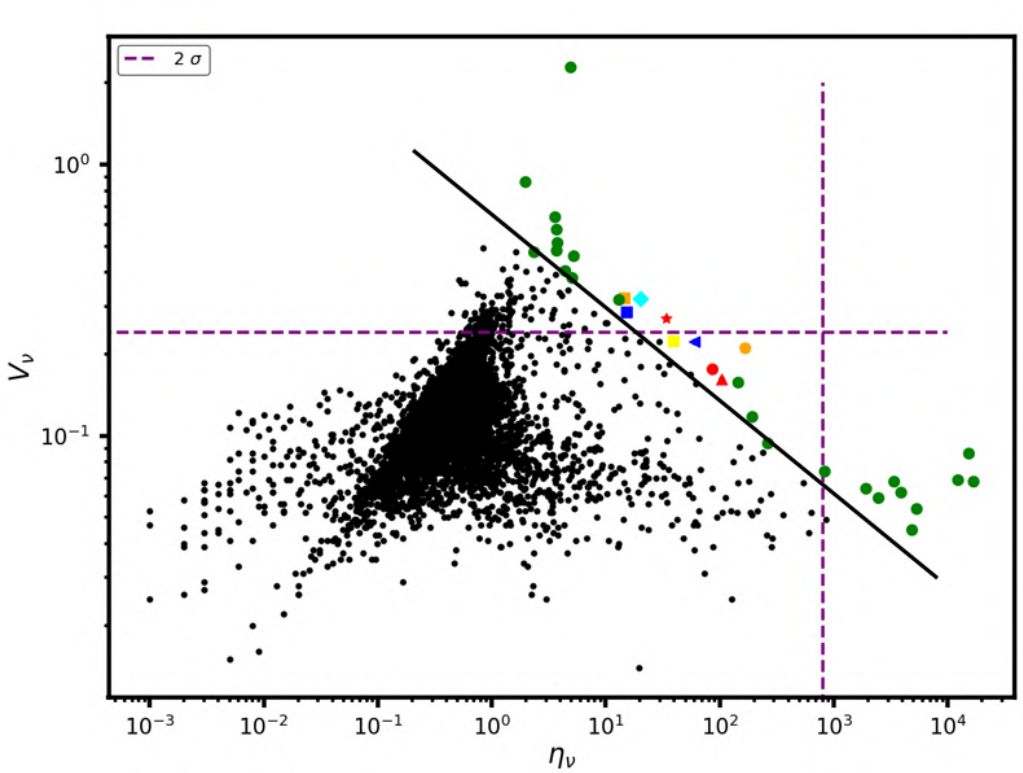


Figure 5.1: The distribution of variability parameters for all sources detected in the NGC 1371 field. Different colours represent the nine variable sources, while black indicates sources that were not investigated. Green denotes sources whose radio images and light curves were visually inspected across ten epochs. The dashed purple lines mark the 2σ thresholds used for filtering these parameters, with $\eta_\nu = 804.04$ and $V_\nu = 0.4$.

© University of Venda

Table 5.1: Characteristics of the nine variable sources identified in the NGC 1371 field, including their ID, position (RA and DEC), variability metrics, colour, and shape.

ID	RA (hh:mm:ss.s)	DEC (dd:mm:ss.s)	η_ν	V_ν	Colour	Shape
68059	03h 35m 03.7s	$-24°39'42.3''$	165.162	0.211	orange	o (circle)
69112	03h 33m 57.6s	$-24°41'30.2''$	103.492	0.162	red	^ (triangle up)
67332	03h 35m 54.3s	$-24°56'04.7''$	85.274	0.176	red	o (circle)
68028	03h 35m 05.4s	$-24°34'36.8''$	59.579	0.223	blue	< (triangle left)
68915	03h 34m 09.5s	$-24°50'20.2''$	38.898	0.224	yellow	s (square)
66491	03h 37m 08.6s	$-25°02'30.1''$	33.752	0.272	red	* (star)
66636	03h 36m 52.0s	$-24°56'52.0''$	20.102	0.321	cyan	D (diamond)
67602	03h 35m 35.9s	$-25°18'51.8''$	15.088	0.286	blue	s (square)
69764	03h 33m 01.4s	$-24°29'34.9''$	14.474	0.323	orange	s (square)

© University of Venda

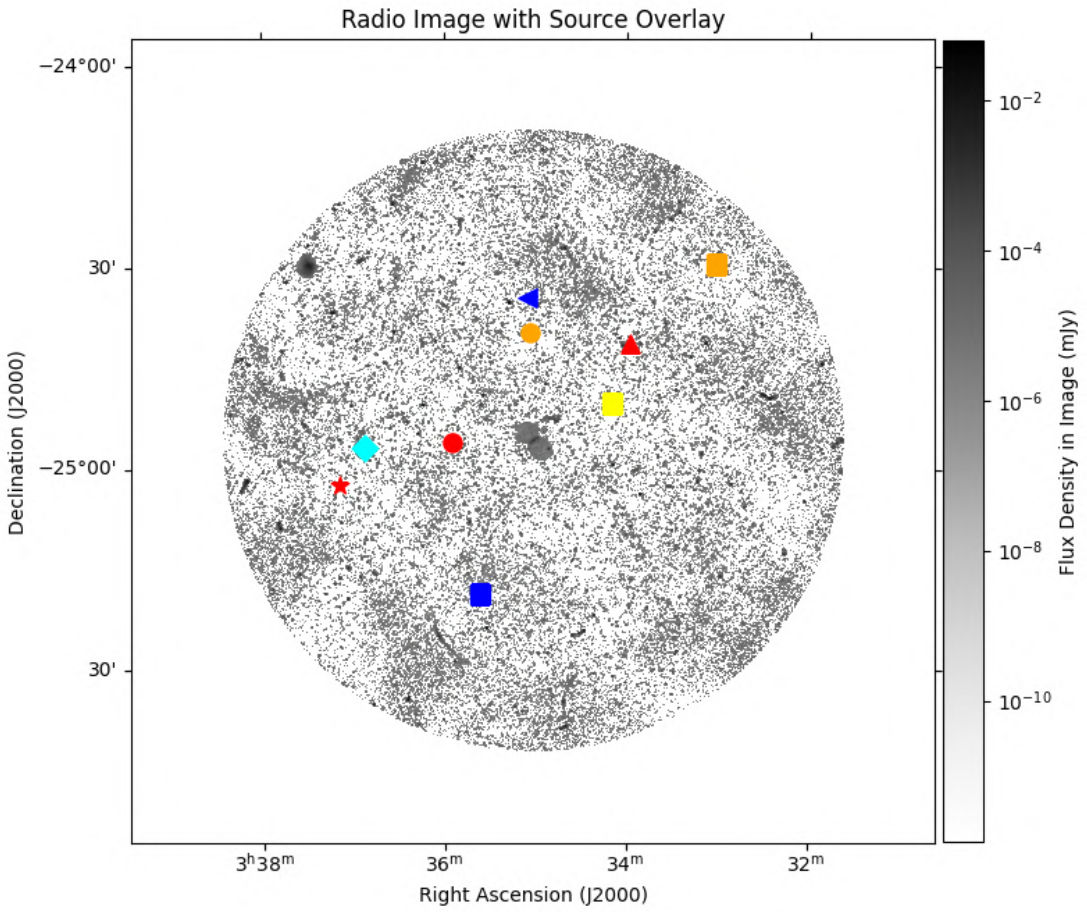


Figure 5.2: MeerKAT SDP image with sources overlayed of the field of NGC 1371. The sources marked in different shapes and colours denote 9 variable sources as listed in Table 5.1.

© University of Venda

5.2 Light curves NGC 1371

The light curves of nine variable sources identified in Figure 5.1 are shown in Figure 5.3, which shows a notable variety among all sources observed. Every plot has a unique ID associated with it. Uncertainty measurements are too small to be visible on the light curve of the source with unique IDs "68059" and "69112". The variation in time of the observed flux density suggests that these radio sources may be associated with active astronomical phenomena like variable stars or AGN. Other multi-wavelengths can be searched for as part of a more thorough analysis of these sources. Each source is discussed in detail in Section 5.5.

© University of Venda

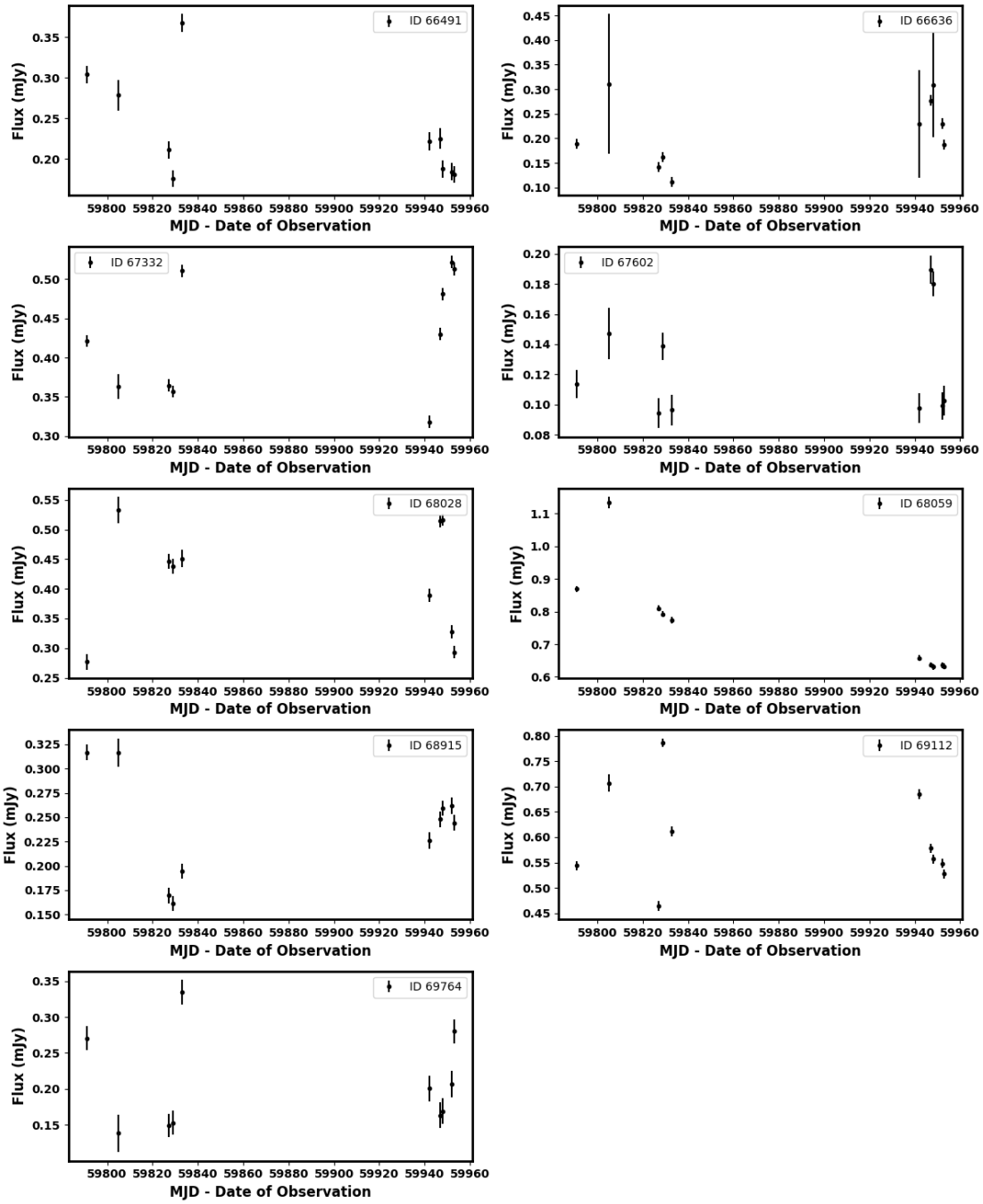


Figure 5.3: The light curves of variable sources identified in Figure 5.1, Each subplot corresponds to a different 9 variable source, identified by unique ID:66491, 66636, 76332, 67602, 68028, 68059, 68915, 69112 and 69764. Uncertainty measurements are too small to be visible on some light curves. The brightest source is 68059 with peak flux density 1.1332 mJy.

© University of Venda

5.3 Snapshots of variable sources identified in NGC 1371

Figures 5.4 to 5.6 show snapshot images of the 9 variable sources identified in Section 5.1 and also marked in Figure 5.1. From upper left to upper right, the images are arranged chronologically. Each image is scaled linearly to the same flux density per panel for each source. Different epochs exhibit different fluxes. In every picture, the synthesised beam may be found in the lower left corner. Point Sources: This observation suggests the source is unresolved, indicating it is a point source rather than an extended object. The point source's brightness fluctuations across different epochs imply it is a variable radio source. This variability could result from changes in intrinsic luminosity or interactions with the surrounding medium. Extended Sources: Extended variations are caused by changes in the PSF and a source larger than the beam (lower left). Transient/Variable classifications are the ones we are specifically searching for, representing point sources with variable light curves.

© University of Venda

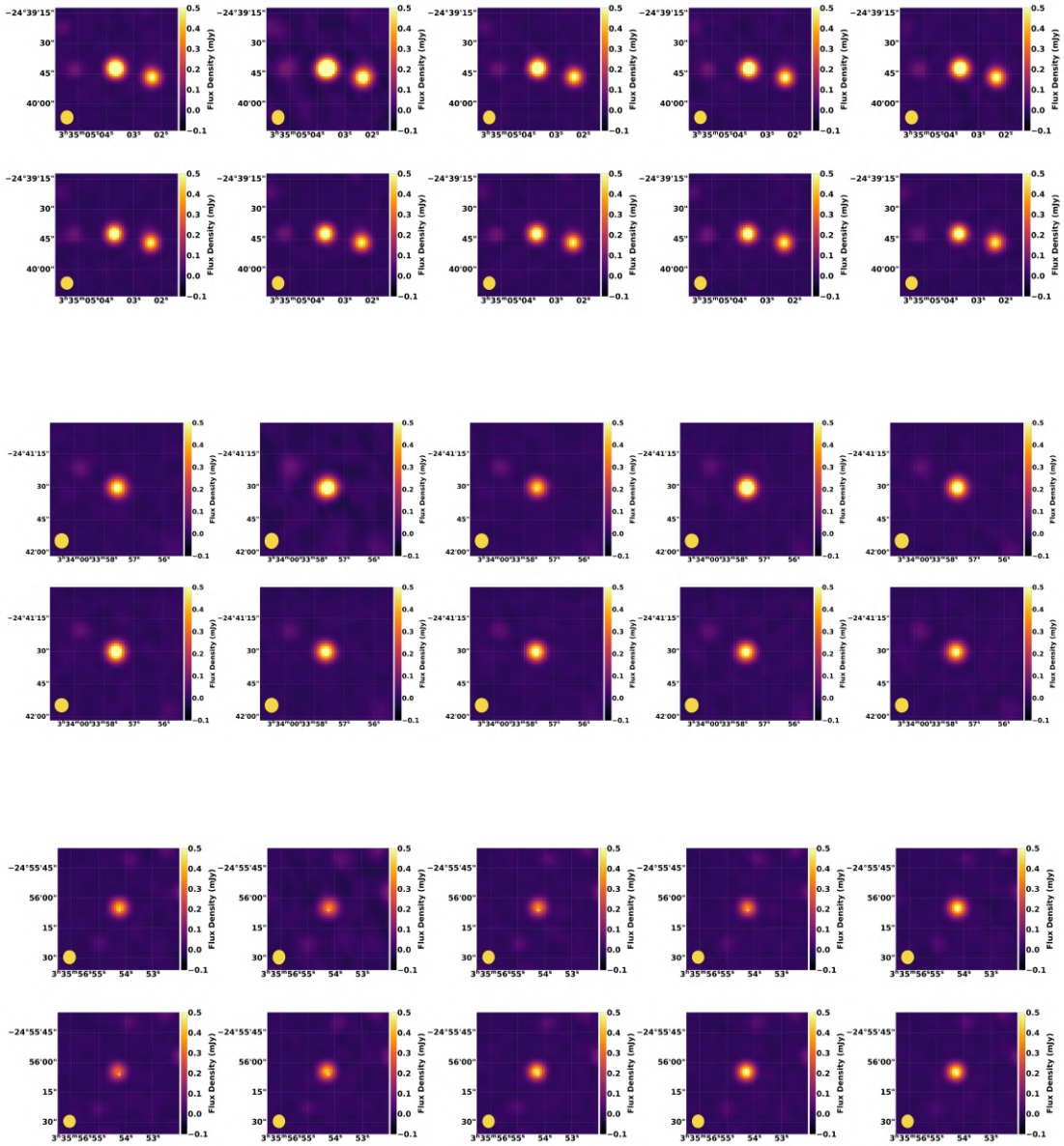


Figure 5.4: Radio image snapshots illustrating the evolution of each source over ten observed epochs. The first panel represents SRC68059, the middle panel shows SRC69112, and the bottom panel corresponds to SRC67332. All the images are scaled to the same flux density range of (-0.1 to 0.5) mJy on a linear scale. The yellow circle in the lower-left corner of each image marks the PSF.

© University of Venda

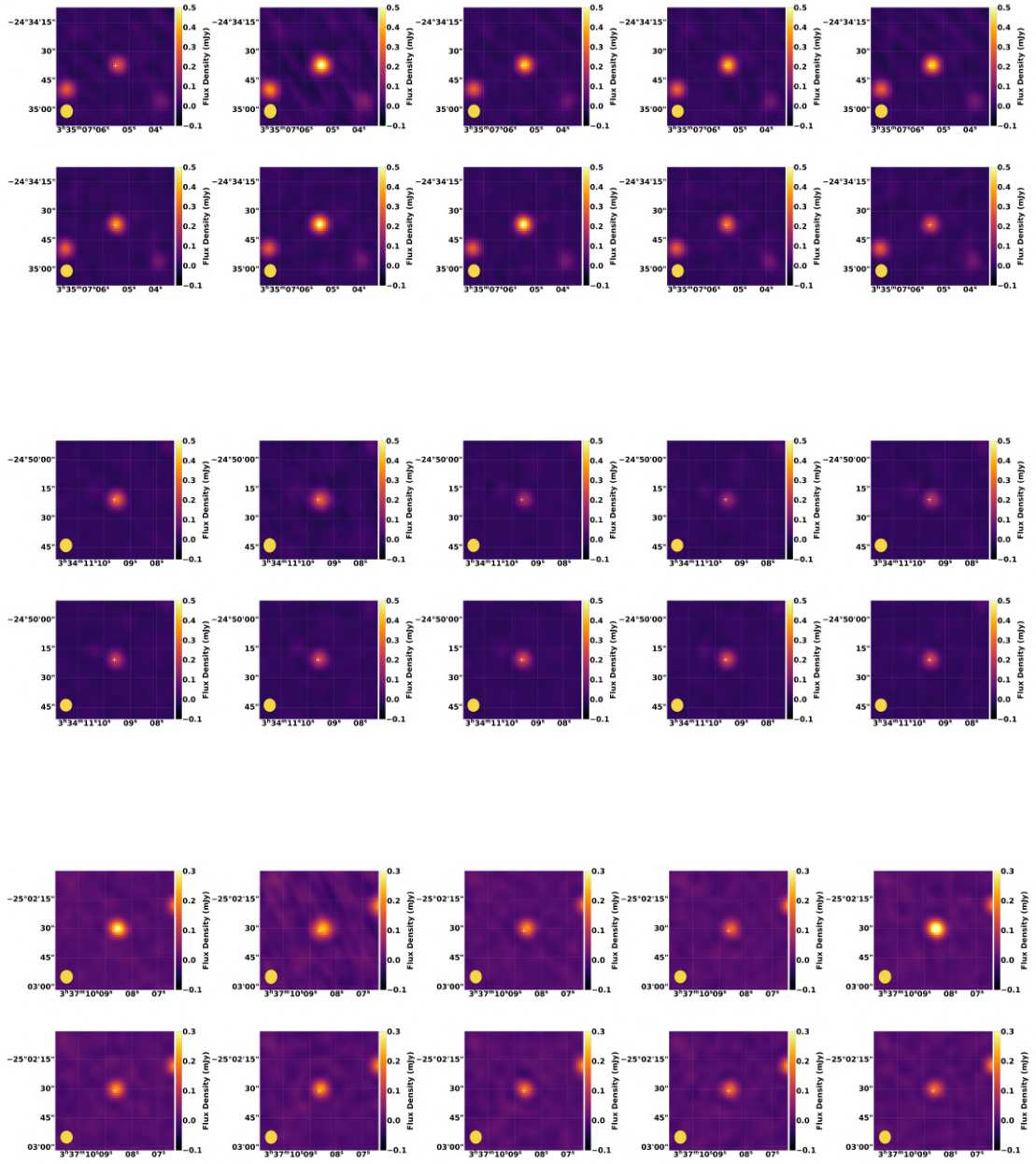


Figure 5.5: Snapshots of radio images showing how each source has changed throughout ten observed epochs. SRC68028 is represented by the first panel, SRC68915 by the middle panel, and SRC66491 by the bottom panel. In the last panel, all the images are scaled to the same flux density range from -0.10 to 0.30 mJy, while in the first and second panels, all images are scaled to the same flux density range of (-0.1 to 0.5) mJy on a linear scale. The yellow circle in the lower-left corner indicates each image's PSF.

© University of Venda

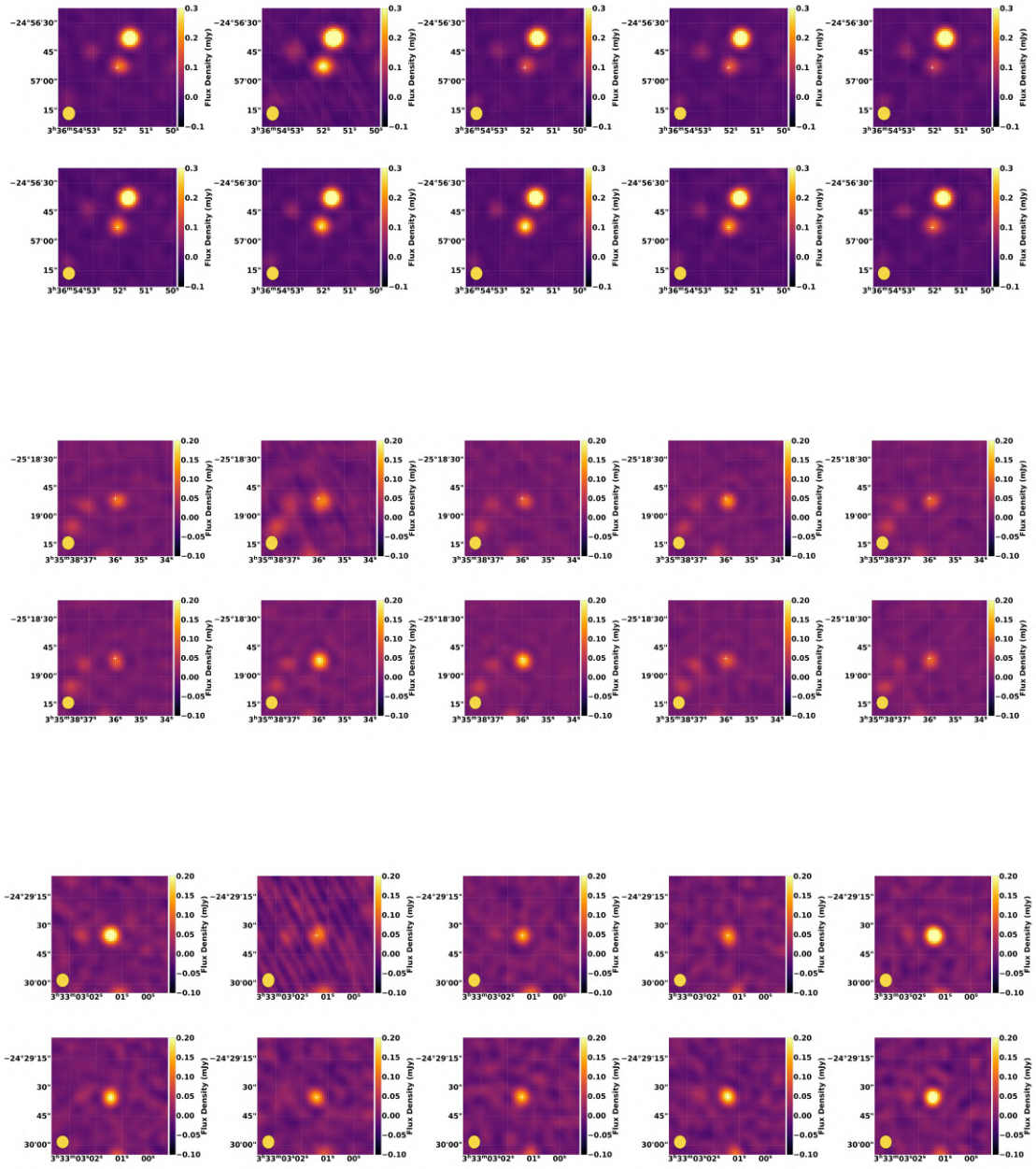


Figure 5.6: Snapshots of radio images illustrating the changes in each source over ten observed epochs. The first panel represents SRC66636, with all images scaled to a flux density range of -0.10 to 0.30 mJy. The middle panel corresponds to SRC67602, and the bottom panel corresponds to SRC69764, with the middle and last panels all images scaled to a flux density range of -0.10 to 0.20 mJy on a linear scale. The yellow circle in the lower-left corner of each image marks the PSF.

© University of Venda

5.4 Correlation of flux density and variability parameter η and V

Figure 5.7 shows cases of the correlation between the flux density measured in millijanskys (mJy) and two variability parameters, η and V, for a set of radio sources in NGC 1371 galaxy. Left Figure: η versus flux density η represents the variability amplitude of the sources. The plot demonstrates a positive correlation between η and the flux density, indicating that sources with higher flux densities exhibit greater variability. The scatter in the data points suggests that, while the trend is generally positive, there is a wide range of variability for sources with similar flux densities. This could imply that other factors, such as intrinsic properties of the sources or observational effects, contribute to the observed variability. The Figure on the right: V versus flux density V represents the variability index, which typically measures the strength or significance of the variability over time. In contrast to η, the right panel shows a negative correlation between V and the flux density. This indicates that sources with higher flux densities tend to have lower variability indices. The data points are tightly clustered at lower V values, especially for higher flux densities, suggesting that brighter sources are more stable in their emission over time compared to fainter ones. This could be due to the averaging effect in more luminous sources or the presence of less significant fluctuations in their light curves.

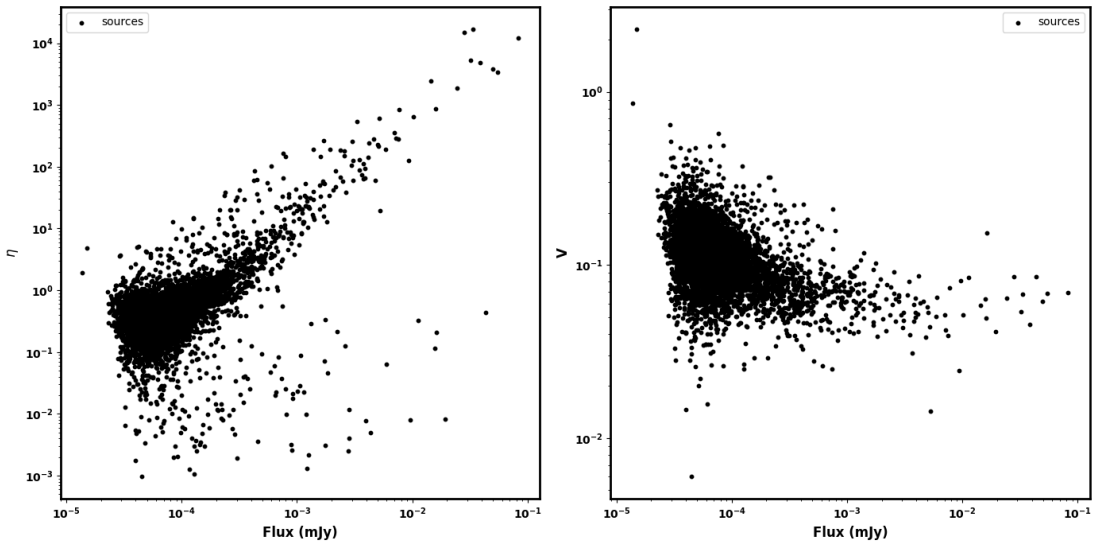


Figure 5.7: The correlation between the flux density and the variability parameters. The left panel shows η vs Flux (mJy), whereas the right panel shows V against flux (mJy).

© University of Venda

5.5 Counterparts across different wavelengths

Counterparts were searched across various wavelengths by examining multiple catalogues in the Vizier database (Ochsenbein et al., 2000). The Dark Energy Survey (DES; (Choi, 2021)) is valued for its deeper optical imaging and was used to search for counterparts and record the R magnitude for the source in Table 5.2. The R magnitude will help to plot the radio flux density (in mJy) versus optical flux density (in mJy) as adapted from the study conducted by (Stewart et al., 2018) to provide an overview of the distribution of different classes of objects. Other significant databases, such as Simbad (Wenger et al., 2000), Gaia (Gaia Collaboration et al., 2023), NED (Helou et al., 1991), AllWISE Source Catalog (Wright et al., 2019), and PanSTARRS (Chambers & Pan-STARRS Team, 2016), were used to search for their counterparts.

The optical counterpart images from The Dark Energy Survey (DES) for the identified sources are shown in Figure 5.9 to 5.10 and discussed in Section 5.5. For each source, Table 5.2 provides the following information: the ID number, right ascension (RA) in hours, minutes, and seconds, declination (DEC) in degrees, arcminutes, and arcseconds, two variability parameters η_ν and V_ν of the sources identified on Figure 5.1, the peak flux in mJy, the associated error in peak flux in mJy, and the R-band magnitude (R mag). These sources are flagged as potential variable sources, with some displaying notable changes in brightness across different epochs. The R-band magnitude provides an estimate of the optical brightness.

Table 5.2: Characteristics of 9 selected variable sources, including Source ID, RA, DEC, variability indices (η_ν and V_ν), and peak flux measurements with uncertainties, summarising their variability and flux ranges.

ID	RA (hh:mm:ss.s)	DEC (dd:mm:ss.s)	η_ν	V_ν	Peak flux (mJy)	Peak flux error (mJy)	R (mag)
68059	03h 35m 03.7s	$-24°39'42.3''$	165.162	0.211	1.1332	0.0104	19.9246
69112	03h 33m 57.6s	$-24°41'30.2''$	103.492	0.162	0.7866	0.0051	23.3392
67332	03h 35m 54.3s	$-24°56'04.7''$	85.274	0.176	0.5218	0.0048	21.4052
68028	03h 35m 05.4s	$-24°34'36.8''$	59.579	0.223	0.5322	0.0130	18.8619
68915	03h 34m 09.5s	$-24°50'20.2''$	38.898	0.224	0.3166	0.0046	21.6389
66491	03h 37m 08.6s	$-25°02'30.1''$	33.752	0.272	0.3037	0.0060	19.3027
66636	03h 36m 52.0s	$-24°56'52.0''$	20.102	0.321	0.2971	0.0588	20.2037
67602	03h 35m 35.9s	$-25°18'51.8''$	15.088	0.286	0.1894	0.0054	23.2482
69764	03h 33m 01.4s	$-24°29'34.9''$	14.474	0.323	0.3345	0.0098	18.9643

5.5.1 SRC68059

SRC68059 is located at RA 03h35m3.7s and DEC $-24°39'42.3''$. The radio light curve shown in Figure 5.3, With measurement uncertainty for flux density ranging from 0.0045-0.0104 mJy, the error bar is too small to be visible on the light curves. Clear variability, with a maximum

© University of Venda

peak flux density of 1.1332 mJy and minimum flux density of 0.6303 mJy. The radio image in Figure 5.4, the first panel represents SRC68059, illustrates its detection and clearly shows its significance as a variable point source and the slight brightness variation from one epoch to another.

The Simbad database was searched using the radio coordinates of SRC68059; however, no known association was identified. In the DES , a counterpart was found associated with DES J033503.66-243942.4, classified as a galaxy (Abbott et al., 2021), as detailed in Table 5.2. At 1.1332 mJy, its maximal flux and r-band (AB) magnitude is 19.9246. Furthermore, WISEA J033503.61-243941.8, a counterpart found in the ALLWISE source catalogue, is categorised as a Galaxy source and is located 0.030 arcminutes away from our target (Cutri et al., 2021).

In Figure 5.8, SRC68059 is marked by a black star positioned in the optically selected quasar sample (blue dots) close to the FIRST sensitivity limit.

5.5.2 SRC69112

SRC69112 is located at RA 03h33m57.6s and DEC $-24°41'30.2''$. Figure 5.3 shows the radio light curve and the flux density measurements uncertainty ranges from 0.0051 to 0.0103 mJy. Clear variability, with a maximum peak flux density of 0.7866 mJy and minimum flux density of 0.4638 mJy. The radio image in Figure 5.4, the middle panel shows SRC69112, clearly showing the detection of SRC69112 as a variable point source, with small variations in brightness from one epoch to another.

The SIMBAD astronomical database was searched using the radio coordinates of the source SRC68059 but could not find any known association source. However, DES had a counterpart associated with DES J033357.58-244130.2, classified as a galaxy (Abbott et al., 2018). This object has a maximum flux of 0.7866 mJy and r-band (AB) magnitude. Additionally, a counterpart source in the ALLWISE catalogue, WISEA J033357.58-244130.3, is categorised as an infrared source and is located approximately 0.004 arcminutes from our target (Cutri et al., 2013).

In Figure 5.8, SRC69112 is marked by a black square near the sensitivity limit of the FIRST survey, suggesting that it is probably an AGN due to its alignment with the diagonal line representing the relationship between optical and radio flux as a function of distance for AGN.

5.5.3 SRC67332

SRC67332 is located at RA 03h35m54.3s and DEC $-24°56'04.7''$. Figure 5.3 shows the radio light curve. The flux density measurements uncertainty ranges from 0.0043 to 0.0090 mJy, and the light curves include visible error bars. Clear variability, with a maximum peak flux density of 0.5218 mJy and minimum flux density of 0.3180 mJy. The radio image in Figure 5.4, the last

© University of Venda

panel represents SRC67332, indicates that is a variable point source, with intensity variations observed across different epochs.

The counterpart of SRC67332 was searched using its radio coordinates in the SIMBAD astronomical database, but no known association was identified. However, a counterpart was detected in the DES, identified as DES J033554.24-245604.7 and classified as a galaxy (Abbott et al., 2018). This galaxy exhibits a maximum flux of 0.5218 mJy and an r-band (AB) magnitude of 21.4052 (see Table 5.2). Additionally, a counterpart was identified in the ALLWISE catalogue, identified as WISEA J033554.25-245605.0 and categorised as an infrared source, located approximately 0.011 arcminutes from the target (Cutri et al., 2013).

In Figure 5.8, SRC67332 is represented by a black diamond; tracing this source by the diagonal line, it is within optical quasars marked by blue dots.

5.5.4 SRC68028

SRC68028 is located at RA 03h35m5.4s and DEC $-24°34'36.8''$. Figure 5.3 illustrates the light curves, including visible error bars. The flux density measurements uncertainty ranges from 0.0058 to 0.0130 mJy. Clear variability, with a maximum peak flux density of 0.5322 mJy and minimum flux density of 0.2769 mJy. The radio image in Figure 5.5, the first panel represents SRC68028, confirms that is a variable point source that shows intensity variations over different epochs.

The counterparts of SRC68028 were searched using its radio coordinates in the SIMBAD astronomical database, but no known association was identified. However, a counterpart was detected in the DES, identified as DES J033505.43-243436.9, which is classified as a galaxy and is located 0.002 arcminutes from the centre (Abbott et al., 2018). This object has a maximum flux of 0.5322 mJy and r-band (AB) magnitude of 18.8619 (see Table 5.2). Additionally, we found a matching source in the ALLWISE catalogue, WISEA J033505.47-243436.2, classified as an infrared source, situated approximately 0.019 arc minutes from our target (Cutri et al., 2013).

In Figure 5.8, SRC68028 is represented by a black plus sign (+), tracing its position with the diagonal line the source is within optical quasars indicated by blue dots, although it is located in a region associated with a gamma-ray burst (GRB).

5.5.5 SRC68915

SRC68915 is located at RA 03h34m9.5s and DEC $-24°50'20.2''$. The light curves illustrated in Figure 5.3, with clear error bars. The flux density measurements uncertainty ranges from 0.0043 to 0.0085 mJy. Clear variability, with a maximum peak flux density of 0.3166 mJy and minimum

© University of Venda

flux density of 0.1614 mJy. SRC68915 is shown by the middle panel r in Figure 5.5. SRC68915 is a variable point source showing intensity changes throughout various epochs.

The source SRC68915 was examined using its radio coordinates in the SIMBAD astronomical database, but no counterpart was identified. Conversely, a counterpart designated as DES J033409.51-245020.3 was detected in the DES. This object is classified as a galaxy located approximately 0.001 arcminutes from the centre of the target (Abbott et al., 2018). This object has an r-band (AB) magnitude of 21.6389 and a maximum flux of 0.3166 mJy (see Table 5.2). Furthermore, a corresponding source, classified as an infrared source and situated 0.027 arcminutes away from our target, was discovered in the ALLWISE database, identified as WISEA J033409.59-245019.3 (Cutri et al., 2013).

The black triangle in Figure 5.8 represents SRC68915, which is located in an area with a gamma-ray burst (GRB); tracing its position with the diagonal line, the source is within optical quasars indicated by blue dots.

5.5.6 SRC66491

SRC66491 is located at RA 03h37m8.6s and DEC $-25°02'30.1''$. Figure 5.3 shows the light curve with clear error bars. The flux density measurements' uncertainty ranges from 0.0060 to 0.0107 mJy. Clear variability, with a maximum peak flux density of 0.3674 mJy and a minimum flux density of 0.1757 mJy. The radio image in Figure 5.5, the last panel, represents SRC66491, which shows variations in intensity over several epochs, indicating that SRC66491 is a variable point source.

The source SRC66491 was searched in the SIMBAD astronomical database using its radio coordinates; however, no counterpart was identified. In contrast, a counterpart was detected in the DES as DES J033708.54-250230 (Abbott et al., 2018). It is classified as a galaxy and lies 0.001 arcminutes from the centre of our target. This has an r-band (AB) magnitude of 19.3027 and max flux of 0.3037 mJy (see Table 5.2). In addition, a counterpart classified as galaxy and located 0.020 arcminutes from our target was found in the ALLWISE catalogue (J033708.55-250230.7) (Cutri et al., 2013).

SRC66491, located in an area with GRBs, is represented by the black circle in Figure 5.8. A diagonal line may be traced to the sample of optical quasars.

5.5.7 SRC66636

SRC66636 is located at RA 03h36m52.0s and DEC $-24°56'52.0''$. Figure 5.3 shows the light curve with clear error bars. The flux density measurements uncertainty ranges from 0.0055 to 0.0762 mJy. Clear variability, with a maximum peak flux density of 0.2971 mJy and minimum

© University of Venda

flux density of 0.1115 mJy. The radio image in Figure 5.6, the first panel, represents SRC66636 and shows intensity variations over multiple epochs, indicating that SRC66636 is a variable point source.

SRC66636 was searched using its radio coordinates in the SIMBAD astronomical database, but no counterpart was identified. A counterpart was detected in the DES as DES J033652.00-245652.1 (Abbott et al., 2018). This object is classified as a galaxy situated just 0.002 arcminutes from the centre of SRC 66636. It has an r-band (AB) magnitude of 20.2037 and a maximum flux of 0.2971 mJy, as detailed in Table 5.2. Additionally, a counterpart in the ALLWISE catalogue was identified as J033651.88+245648.4 (infrared), located 0.064 arcminutes from our target (Cutri et al., 2013).

SRC66636, marked by a black circle in Figure 5.8, is located in an area known for GRBs. Furthermore, it can be traced back to a sample of optical quasars, as shown by the diagonal line.

5.5.8 SRC67602

SRC67602 is located at RA 03h35m35.9s and DEC $-25°18'51.8''$. Figure 5.3 shows the light curve with clear error bars. The flux density measurements uncertainty ranges from 0.0048 to 0.0098 mJy. Clear variability, with a maximum peak flux density of 0.1894 mJy and minimum flux density of 0.0939 mJy. The radio image in Figure 5.6 the middle panel represents SRC67602 reveals intensity variations in multiple epochs, suggesting that SRC67602 is a variable point source

The source SRC67602 was searched in the SIMBAD astronomical database using its radio coordinates, but no counterparts were found. However, a counterpart identified as DES J033535.90-251851.8 was identified in DES (Abbott et al., 2018). This object is classified as a galaxy located just 0.002 arcminutes from the centre of SRC67602. It has an r-band (AB) magnitude of 23.248 and a maximum flux of 0.1894 mJy, as shown in Table 5.2. Additionally, a counterpart was discovered as an infrared in the ALLWISE catalogue (Cutri et al., 2013), named J033535.87-251852.0, located 0.006 arcminutes from SRC67602.

SRC67602 is indicated by a black pentagon in Figure 5.8, is located in a region known for gamma-ray bursts (GRBs). Moreover, SRC67602 can be traced to a sample of optical quasars, as the diagonal line indicates.

5.5.9 SRC69764

SRC69764 is located at RA 03h33m1.4s and DEC $-24°29'34.9''$. Figure 5.3 shows the light curve with clear error bars. The flux density measurements uncertainty ranges from 0.0093 to 0.0106 mJy. Clear variability, with a maximum peak flux density of 0.3345 mJy and minimum flux

© University of Venda

density of 0.1367 mJy. Figure 5.6, the last panel shows SRC69764 radio image with brightness variations across multiple epochs, indicating that SRC69764 is a variable point source.

SRC69764 was searched in the SIMBAD astronomical database using its radio coordinates, but no counterparts were found. However, a counterpart identified as DES J033301.41-242935.0 in the DES (Abbott et al., 2018), classified as a galaxy and located just 0.001 arcminutes from the centre of SRC 69764. This object has an r-band (AB) magnitude of 18.9643 and a maximum flux of 0.3345 mJy, as detailed in Table 5.2. A counterpart was found in the ALLWISE catalogue, classified as galaxy: J033301.40-242934.8 and MRSS 482-092991, situated 0.011 arcminutes from SRC69764. A counterpart association found in Gaia data early release 3: Gaia EDR3 5085883260114831104 (Gaia Collaboration et al., 2021).

SRC69764 is marked by a black right triangle in Figure 5.8 and is located in a region associated with GRBs. Additionally, SRC69764 is associated with a sample of optical quasars, as can be traced by the diagonal line.

This section will provide a plot showing a relationship between radio and optical flux between known variable sources and transients. The study was adapted from (Stewart et al., 2018). At the end of this section, the will be the optical counterpart images from DES.

© University of Venda

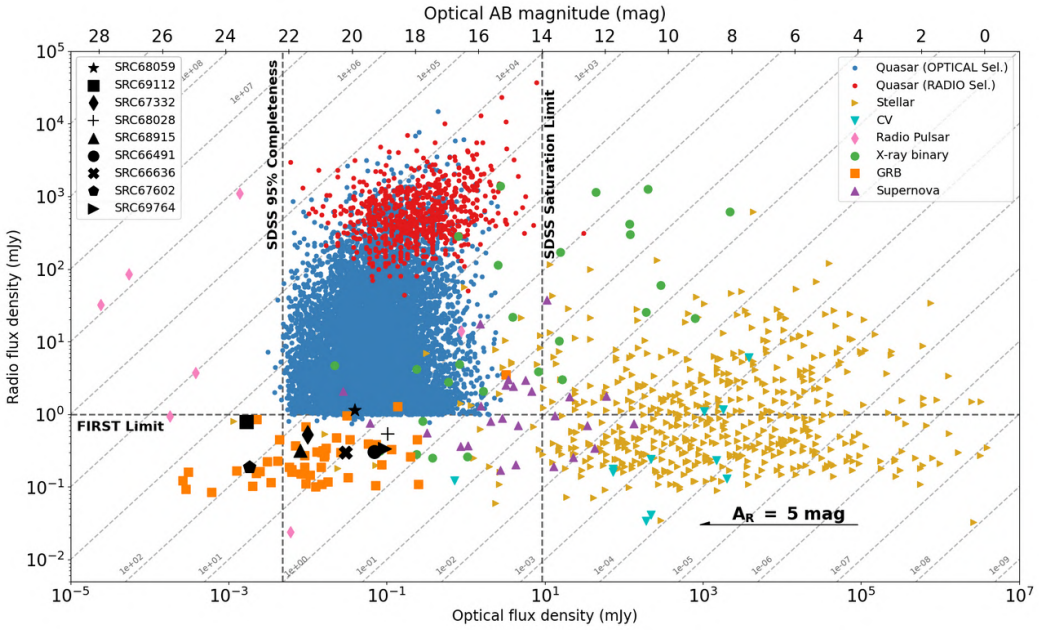


Figure 5.8: Radio versus optical flux density of objects from different classes, adapted from (Stewart et al., 2018), all my sources are represented by black colour with different symbols. Their positions relative to the diagonal dashed lines and survey limits can help identify their classes.

Figure 5.8 shows a density plot of various astronomical objects, with their radio flux density (in mJy) plotted on the y-axis and optical AB magnitude (in mag) on the x-axis. The plot includes diagonal dashed lines representing the slope of a constant radio-to-optical flux ratio, along with lines indicating survey limits for the FIRST and SDSS surveys. These lines represent constant radio-to-optical flux density ratios, and objects that lie on or near these lines have similar ratios, indicating a consistent relationship between their radio and optical emissions. The FIRST limit, represented by a horizontal line, denotes the sensitivity limit of the FIRST radio survey, suggesting that sources below this line have radio flux densities lower than the FIRST survey's detection threshold.

The SDSS limits, represented by vertical lines, include the saturation limit at 14 mag (left line), where sources to the left are too bright and might be saturated in SDSS data, and the 95% completeness limit at 22 mag (right line), where sources to the right might not be reliably detected in SDSS data. In Figure 5.8, All my sources are shown in black and have different shapes. Their positions relative to the diagonal dashed lines and survey limits can help identify their classes, and they are likely to be AGN as they are traced by diagonal lines and fall with the Quasar class. The diagonal lines denote a constant ratio between radio and optical flux density, although all our sources occupy parameter space with GRBs.

© University of Venda

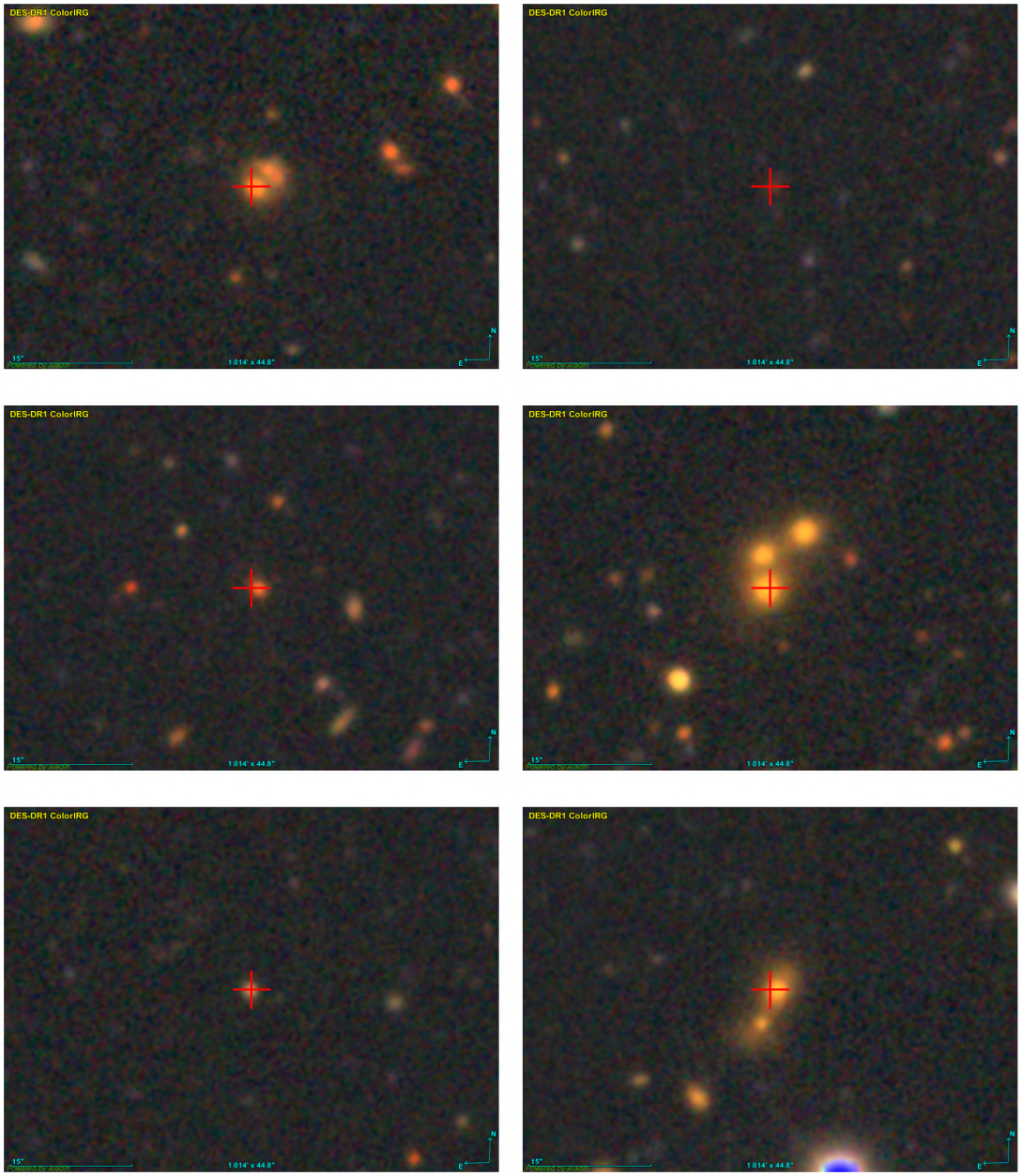


Figure 5.9: The first panel presents optical images from the Dark Energy Survey (DES), with SRC68059 on the left and SRC69112 on the right. The middle panel shows SRC67332 (left) and SRC68028 (right), while the final panel shows SRC68915 (left) and SRC664915 (right). Each source is marked at its central position with a red cross. The images measure 1 arcminute by 45 arcseconds, with arrows in the bottom right corner indicating the sky's direction, where "N" denotes North and "E" denotes East.

© University of Venda

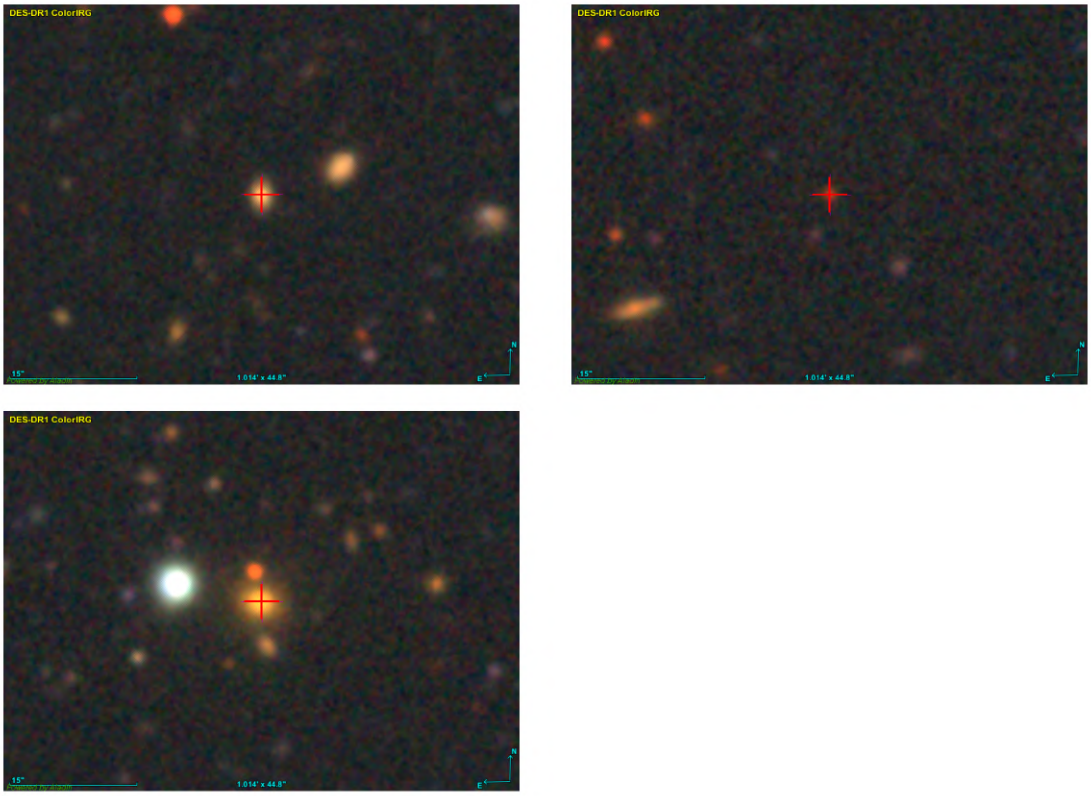


Figure 5.10: The first panel presents optical images from the Dark Energy Survey (DES), with SRC66636 on the left and SRC676027 on the right, while the final panel represents SRC69764. Each source is marked at its central position with a red cross. The images measure 1 arcminute by 45 arcseconds, with arrows in the bottom right corner indicating the sky direction, where "N" denotes North and "E" denotes East.

© University of Venda

University of Venda
Creating Future Leaders

Chapter 6

Conclusion

The study searched for transient and variable sources within the MHONGOOSE Large Survey Project (LSP), specifically focusing on the fields of NGC 1566, NGC 5068, and NGC 1371, observed over 10 epochs. The study used the SDP images from SARAO, which serve as quality-assessed data products of the MHONGOOSE LSP observations. The use of the SARAO SDP images for this purpose is tested as they currently provide the fastest latency between observation and primary beam-corrected images, potentially leading to a near real-time search for transients in images. Each of the three fields was observed for approximately 5.5 hours. To detect transients, we employed the TraP, an automated tool designed for reliable detection of transient and variable sources, which is critical given the expected increase in data volume from large transient surveys.

The TraP processes these datasets by detecting sources, establishing source associations, and generating light curves. However, successfully identifying transients and variables depends on selecting appropriate thresholds, which the astronomer must carefully choose. Although high values of variability parameters often characterise transients, this is not universally applicable. Some transients may lack sufficient data points in their light curves to confirm variability or stabilise after their initial appearance, resulting in relatively stable flux. TraP addresses this challenge by assessing whether sources would have been detectable in previous best images, ensuring reliable source identification.

Employing the TraP with default parameters, sources exhibiting a 2σ threshold of either η_ν or V_ν were considered potential variables. A total of 31 variable sources were identified across these three fields, revealing counterparts associated with AGNs and quasars after multi-wavelength follow-up. Detecting these variable AGNs significantly expands the known population of such sources. Employing imaging surveys to identify variability enhances the ability to uncover and study these dynamic radio sources, contributing to the growing field of time-domain radio astronomy.

© University of Venda

A relevant comparison can be made with the study by Fijma et al. (2024), who conducted a commensal short-duration transient survey of NGC 5068 using MeerKAT data, where no transient sources were found. This also aligns with what was found in this research. No transient was found in the field of NGC 5068. Notably, no previous studies have systematically searched for radio transients in the MHONGOOSE observations of NGC 1566 or NGC 1371, making this study the first to probe these galaxies for variable and transient activity in the radio domain. Several studies have utilised the MHONGOOSE survey data, focusing primarily on the distribution and kinematics of neutral hydrogen (HI) in nearby galaxies. Healy et al. (2024) investigated the HI distribution in NGC 5068, revealing complex structures including a warped outer disk and clumpy gas regions, suggesting possible gas accretion events. Maccagni et al. (2024) discovered a gas-rich low-surface brightness galaxy in the Dorado Group using MHONGOOSE data of the NGC 1566 field, highlighting the survey's capability to detect faint HI sources.

However, notably, one transient was found in the NGC 1566 in this study, "SRC76717", with a total proper motion (pm) of 41.500 mas/yr (Gaia Collaboration, 2020). At Transiting Exoplanet Survey Satellite (TESS) Input Catalog - v8.0 (TIC-8) source was found with ID TIC 396731889 and classified as a star, with a period of 5.8911 days and distance of 48 parsecs away from Earth (Doyle et al., 2019), which relates to the rotational period of a specific M dwarf star. A rotational period of ~ 5.9 days suggests the star is relatively young but older than ultra-fast rotators (e.g., periods < 1 day), potentially falling in the middle of its pre-main-sequence or early main-sequence evolution (Doyle et al., 2019). There was a counterpart on 2MASS (2Micron All-Sky Survey) associated with 2MASS J04240094-5512223. The properties of 2MASS J04240094-5512223 listed in Table 2 of Kraus et al. (2014) are as follows: Radial Velocity ($v_{\rm rad}$) of $19.0 \pm 0.7\,$km/s, Rotational Velocity ($v \sin(i)$) of $6.9 \pm 0.9\,$km/s, Spectral Type (SpT) classified as M2.0, Hα Equivalent Width (EW[Hα]) measured at $-3.54\,$Å, and Lithium Equivalent Width (EW[$\rm Li_{6708}$]) of $21.2\,$mÅ. These properties indicate that the star is a low-mass, cool dwarf in the main sequence or possibly in the pre-main-sequence stage if it is young.

6.1 Future work

Further investigation is essential to confirm the nature of the detected sources and fully explore their astrophysical implications. One key aspect of this follow-up work is to examine whether extrinsic effects, such as interstellar scintillation, drive the observed variability. Interstellar scintillation refers to the scattering of radio waves by irregularities in the electron density of the interstellar medium, which can cause variations in the observed radio brightness of compact sources, including AGN. For AGNs, which are powerful radio emitters, interstellar scintillation can explain short-term variability in their flux. However, not all variability can be attributed to scintillation. In some cases, the observed modulation and variability timescales deviate significantly from those expected based on scintillation models. This suggests that the variability is

© University of Venda

University of Venda
Creating Future Leaders

intrinsic to the AGN itself, possibly driven by physical processes occurring within the nucleus, such as changes in the accretion rate onto the supermassive black hole or jet activity. By distinguishing between extrinsic (scintillation) and intrinsic variability, future studies can provide deeper insights into the mechanisms driving AGN variability. Additionally, Long-term monitoring and multi-wavelength observations could further reveal whether the variability is consistent across different parts of the electromagnetic spectrum, which would support intrinsic processes as the cause. This continued investigation will be crucial for understanding the role of AGNs in galaxy evolution and the behaviour of the transient radio sky.

© University of Venda

University of Venda
Creating Future Leaders

Bibliography

Abbott T. M. C., et al., 2018, ApJS, 239, 18

Abbott T. M. C., et al., 2021, ApJS, 255, 20

Andersson A., et al., 2023, MNRAS, 523, 2219

Andre P., 1996, in Taylor A. R., Paredes J. M., eds, Astronomical Society of the Pacific Conference Series Vol. 93, Radio Emission from the Stars and the Sun. pp 273–284

Barr R., 1998, Advances in Space Research, 21, 677

Bell Burnell J., 2017, Nature Astronomy, 1, 831

Benford G., Tzach D., 2000, MNRAS, 317, 497

Benz A. O., Güdel M., 2010, ARA&A, 48, 241

Berger E., 2014, ARA&A, 52, 43

Bertin E., Arnouts S., 1996, A&AS, 117, 393

Bezuidenhout M. C., et al., 2023, RAS Techniques and Instruments, 2, 114

Bhandari S., et al., 2023, ApJ, 948, 67

Bignall H. E., Hodgson J. A., 2011, Proceedings of the International Astronomical Union, 7, 129–132

Blandford R. D., Königl A., 1979, ApJ, 232, 34

Blandford R. D., Payne D. G., 1982, MNRAS, 199, 883

Blandford R., Meier D., Readhead A., 2019, ARA&A, 57, 467

Burrows A., 2000, Nature, 403, 727

Burrows A., Vartanyan D., 2021, Nature, 589, 29

Caleb M., et al., 2022, Nature Astronomy, 6, 828

© University of Venda

University of Venda
Creating Future Leaders

Caleb M., et al., 2024, Nature Astronomy, 8, 1159

Camilo F., 2018, Nature Astronomy, 2, 594

Cécere M., Velázquez P. F., Araudo A. T., De Colle F., Esquivel A., Carrasco-González C., Rodríguez L. F., 2016, ApJ, 816, 64

Chambers K. C., Pan-STARRS Team 2016, in American Astronomical Society Meeting Abstracts #227. p. 324.07

Chime/Frb Collaboration et al., 2023, ApJ, 947, 83

Choi A., 2021, in APS April Meeting Abstracts. p. Y06.001

Combes F., et al., 2014, A&A, 565, A97

Comrie A., Rosolowsky E., Wang K.-S., Gooch R., et al. 2021, Astronomical Data Analysis Software and Systems XXX (ADASS XXX), ASP Conference Series

Condon J. J., Ransom S. M., 2016, Essential Radio Astronomy. Princeton University Press

Cordes J. M., 1979, Space Sci. Rev., 24, 567

Costa E., et al., 1997, Nature, 387, 783

Cutri R. M., et al., 2013, Explanatory Supplement to the AllWISE Data Release Products, Explanatory Supplement to the AllWISE Data Release Products, by R. M. Cutri et al.

Cutri R. M., et al., 2021, VizieR Online Data Catalog: AllWISE Data Release (Cutri+ 2013), VizieR On-line Data Catalog: II/328. Originally published in: IPAC/Caltech (2013)

Dallal S., Azzam W., 2021, International Journal of Astronomy and Astrophysics, 11, 73

Doyle L., Ramsay G., Doyle J. G., Wu K., 2019, MNRAS, 489, 437

Driessen L., 2020, Astronomy and Geophysics, 61, 5.12

Driessen L. N., et al., 2020, MNRAS, 491, 560

Driessen L. N., et al., 2022, MNRAS, 512, 5037

Driessen L. N., et al., 2024, MNRAS, 527, 3659

Fender R., Stewart A., Macquart J. P., Donnarumma I., Murphy T., Deller A., Paragi Z., Chatterjee S., 2015, PoS, AASKA14, 051

Fender R., et al., 2017, Proceedings of Science

Fijma S., et al., 2024, MNRAS, 528, 6985

© University of Venda

University of Venda
Creating Future Leaders

Gaia Collaboration 2020, VizieR Online Data Catalog: Gaia EDR3 (Gaia Collaboration, 2020), VizieR On-line Data Catalog: I/350. Originally published in: 2021A&A...649A...1G; doi:10.5270/esa-1ug, doi:10.26093/cds/vizier.1350

Gaia Collaboration 2022, VizieR Online Data Catalog: Gaia DR3 Part 2. Extra-galactic (Gaia Collaboration, 2022), VizieR On-line Data Catalog: I/356. Originally published in: Astron. Astrophys., in prep. 2022)

Gaia Collaboration et al., 2018, A&A, 616, A1

Gaia Collaboration et al., 2021, A&A, 649, A1

Gaia Collaboration et al., 2023, A&A, 674, A1

Gehrels N., Mészáros P., 2012, Science, 337, 932

Gezari S., et al., 2013, ApJ, 766, 60

Ghisellini G., Locatelli N., 2018, A&A, 613, A61

Glassgold A. E., Feigelson E. D., Momtmerle T., Wolk S., 2005, ASP Conf. Ser., 341, 165

Grasha K., et al., 2022, The Astrophysical Journal, 929, 118

Güdel M., 2002, Annual Review of Astronomy and Astrophysics, 40, 217

Guedel M., 2002, Annual Review of Astronomy and Astrophysics, 40

Habibi F., Moniez M., Ansari R., Rahvar S., 2013, A&A, 552, A93

Hancock P. J., Charlton E. G., Macquart J.-P., Hurley-Walker N., 2019, arXiv e-prints, p. arXiv:1907.08395

Healy J., et al., 2024, A&A, 687, A254

Helou G., Madore B. F., Schmitz M., Bicay M. D., Wu X., Bennett J., 1991, in Albrecht M. A., Egret D., eds, Astrophysics and Space Science Library Vol. 171, Databases and On-line Data in Astronomy. pp 89–106, doi:10.1007/978-94-011-3250-3_10

Herranz D., Vielva P., 2010, IEEE Signal Processing Magazine, 27, 67

Hester J., 2008, Annual Review of Astronomy and Astrophysics, 46, 127

Hewish A., Bell S. J., Pilkington J. D. H., Scott P. F., Collins R. A., 1968, Nature, 217, 709

Hoare M., et al., 2015, PoS, AASKA14, 115

Holwerda B. W., Blyth S.-L., Baker A. J., 2011, Proceedings of the International Astronomical Union, 7, 496–499

© University of Venda

University of Venda
Creating Future Leaders

Hovatta T., Tornikoski M., Lainela M., Lehto H. J., Valtaoja E., Torniainen I., Aller M. F., Aller H. D., 2007, A&A, 469, 899

Hovatta T., Nieppola E., Tornikoski M., Valtaoja E., Aller M. F., Aller H. D., 2008, A&A, 485, 51

Immler S., Brown P., 2005, Central Bureau Electronic Telegrams, 289, 1

Jansky C. M., 1958, Proceedings of the IRE, 46, 13

Jarrett T. H., Chester T., Cutri R., Schneider S., Skrutskie M., Huchra J. P., 2000, AJ, 119, 2498

Jarvis M., et al., 2018, PoS, MeerKAT2016, 006

Johnston S., et al 2007, Publications of the Astronomical Society of Australia, 24, 174

Jonas J., 2018, PoS, MeerKAT2016, 001

Jones A., Lasenby A., 1998, Living Reviews in Relativity, 1

Kellermann K. I., Pauliny-Toth I. I. K., 1969, ApJ, 155, L71

Kelly B. C., Bechtold J., Siemiginowska A., 2009, ApJ, 698, 895

Kilborn V., Koribalski B., Forbes D., Barnes D., Musgrave R., 2005, Monthly Notices of The Royal Astronomical Society - MON NOTIC ROY ASTRON SOC, 356, 77

Klebesadel R. W., Strong I. B., Olson R. A., 1973, ApJ, 182, L85

Kowalski A., 2024, Living Reviews in Solar Physics, 21

Kraus A. L., Shkolnik E. L., Allers K. N., Liu M. C., 2014, AJ, 147, 146

Kumar P., Zhang B., 2015, Phys. Rep., 561, 1

Labate M. G., Waterson M., Alachkar B., Hendre A., Lewis P., Bartolini M., Dewdney P., 2022, Journal of Astronomical Telescopes, Instruments, and Systems, 8, 011024

Large M. I., 1963, in Palmer H. P., Large M. I., eds, Radio Astronomy Today. pp 126–137

Lawrence A., Watson M. G., Pounds K. A., Elvis M., 1987, Nature, 325, 694

Lee C.-F., Ho P. T. P., Hirano N., Beuther H., Bourke T. L., Shang H., Zhang Q., 2007, ApJ, 659, 499

Lorimer D. R., Bailes M., McLaughlin M. A., Narkevic D. J., Crawford F., 2007, Science, 318, 777

MacFadyen A. I., Woosley S. E., 1999, ApJ, 524, 262

© University of Venda

University of Venda
Creating Future Leaders

Maccagni F. M., et al., 2024, A&A, 690, A69

Maddox S. J., Sutherland W. J., Efstathiou G., Loveday J., Peterson B. A., 1990, MNRAS, 247, 1P

Mauch T., et al., 2020, ApJ, 888, 61

McCray R., Fransson C., 2016, ARA&A, 54, 19

Melrose D. B., 2017, Reviews of Modern Plasma Physics, 1, 5

Merloni A., Heinz S., 2013, in Oswalt T. D., Keel W. C., eds, , Vol. 6, Planets, Stars and Stellar Systems. Volume 6: Extragalactic Astronomy and Cosmology. Springer, p. 503, doi:10.1007/978-94-007-5609-0_11

Metzger B. D., Williams P. K. G., Berger E., 2015, ApJ, 806, 224

Mikhailov K., van Leeuwen J., 2016, A&A, 593, A21

Mohan S., Vig S., Mandal S., 2022, MNRAS, 514, 3709

Murphy T., et al., 2013, , 30, e006

Niu C. H., et al., 2022, Nature, 606, 873

Ochmann M. W., et al., 2024, Astronomy & Astrophysics, 686, A17

Ochsenbein F., Bauer P., Marcout J., 2000, A&AS, 143, 23

Oknyansky V. L., Winkler H., Tsygankov S. S., Lipunov V. M., Gorbovskoy E. S., van Wyk F., Buckley D. A. H., Tyurina N. V., 2019, MNRAS, 483, 558

Orchiston W., Sullivan W. T. I., 2005, Journal of Astronomical History and Heritage, 8, 135

Osten R. A., et al., 2016, ApJ, 832, 174

Padovani P., 2016, A&A Rev., 24, 13

Padovani P., et al., 2017, A&A Rev., 25, 2

Palau A., et al., 2014, MNRAS, 444, 833

Park J., Trippe S., 2017, ApJ, 834, 157

Peebles P. J. E., Schramm D. N., Turner E. L., Kron R. G., 1996, in Schramm D. N., ed., , The Big Bang and Other Explosions in Nuclear and Particle Astrophysics. World Scientific Publishing Co. Pte. Ltd, pp 13–17, doi:10.1142/9789812831538_0002

Perley R., et al., 2009, IEEE Proceedings, 97, 1448

© University of Venda

University of Venda
Creating Future Leaders

Petroff E., Hessels J. W. T., Lorimer D. R., 2019, A&A Rev., 27, 4

Pettersen B. R., 1989, Sol. Phys., 121, 299

Pietka M., Fender R. P., Keane E. F., 2015, MNRAS, 446, 3687

Pleunis Z., et al., 2021, ApJ, 923, 1

Rees M. J., 1978, The Observatory, 98, 210

Reich W., Wielebinski R., 2002, Astronomische Nachrichten, 323, 530

Ricci C., Trakhtenbrot B., 2023, Nature Astronomy, 7, 1282

Rowlinson A., et al., 2022, MNRAS, 517, 2894

Shan Y., et al., 2017, ApJ, 846, 93

Stephenson F. R., 2010, Astronomy and Geophysics, 51, 5.27

Stewart A. J., Muñoz-Darias T., Fender R. P., Pietka M., 2018, MNRAS, 479, 2481

Stinebring D. R., Faison M. D., McKinnon M. M., 1996, ApJ, 460, 460

Swinbank J. D., et al., 2015, Astronomy and Computing, 11, 25

Thompson A. R., Moran J. M., Swenson Jr. G. W., 2017, Interferometry and Synthesis in Radio Astronomy, 3rd edn. Astronomy and Astrophysics Library, Springer, doi:10.1007/978-3-319-44431-4, https://doi.org/10.1007/978-3-319-44431-4

Tsang O., Kirk J. G., 2007, A&A, 463, 145

Ulrich M.-H., Maraschi L., Urry C. M., 1997, ARA&A, 35, 445

Wenger M., et al., 2000, Astronomy and Astrophysics Supplement Series, 143, 9

Westerhout G., 1953, Monthly Notes of the Astronomical Society of South Africa, 12, 2

Wirth H., Haas J., Šubr L., Jerabkova T., Yan Z., Kroupa P., 2024, A&A, 691, A227

Woosley S. E., 1993, ApJ, 405, 273

Woosley S. E., Weaver T. A., 1986, ARA&A, 24, 205

Woudt P. A., et al., 2018, PoS, MeerKAT2016, 013

Wright E. L., et al., 2019, AllWISE Source Catalog, NASA IPAC DataSet, IRSA1, doi:10.26131/IRSA1

Yamasaki S., Goto T., Ling C.-T., Hashimoto T., 2024, MNRAS, 527, 11158

© University of Venda

Young N., 2011, in 41st Young European Radio Astronomers Conference. p. 47

Zhao F.-Y., Strom R. G., Jiang S.-Y., 2006, , 6, 635

Zheleznyakov V. V., Thejappa G., Koryagin S. A., Stone R. G., 2000, Geophysical Monograph Series, 119, 57

da Silva L. A. L., 1993, Ap&SS, 202, 215

de Blok W., et al., 2018, PoS, MeerKAT2016, 007

de Blok W. J. G., et al., 2024, A&A, 688, A109

de Bruyn A. G., Bernardi G., Lofar Eor-Team 2009, in Saikia D. J., Green D. A., Gupta Y., Venturi T., eds, Astronomical Society of the Pacific Conference Series Vol. 407, The Low-Frequency Radio Universe. p. 3

van Haarlem M. P., et al., 2013, A&A, 556, A2

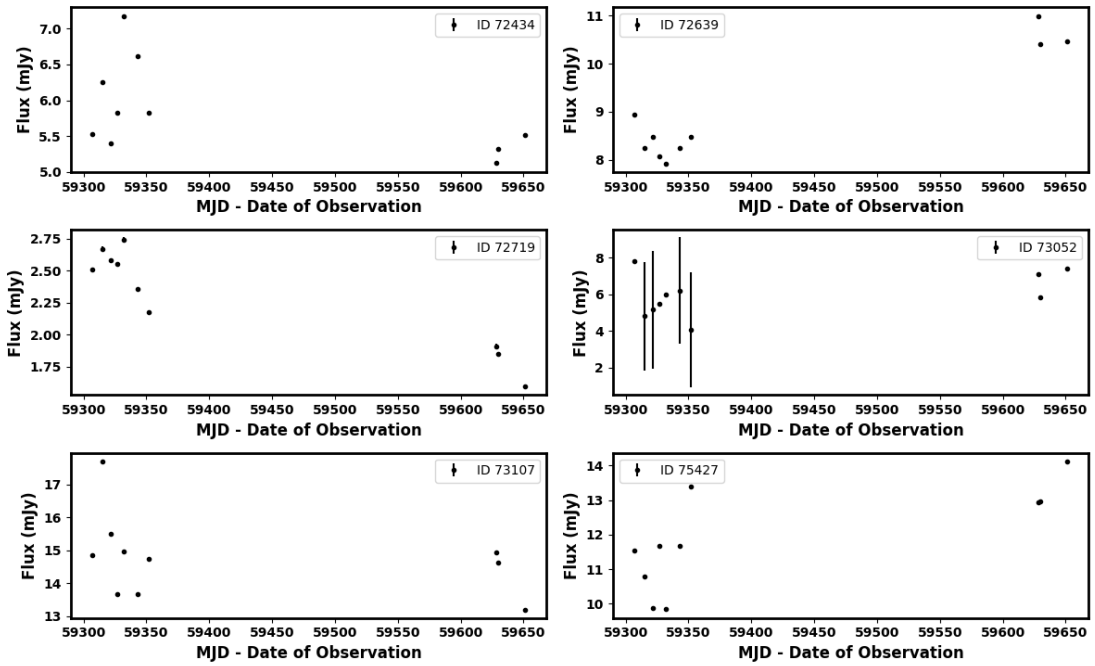
van der Tol S., Jeffs B. D., van der Veen A. J., 2007, IEEE Transactions on Signal Processing, 55, 4497

© University of Venda

University of Venda
Creating Future Leaders

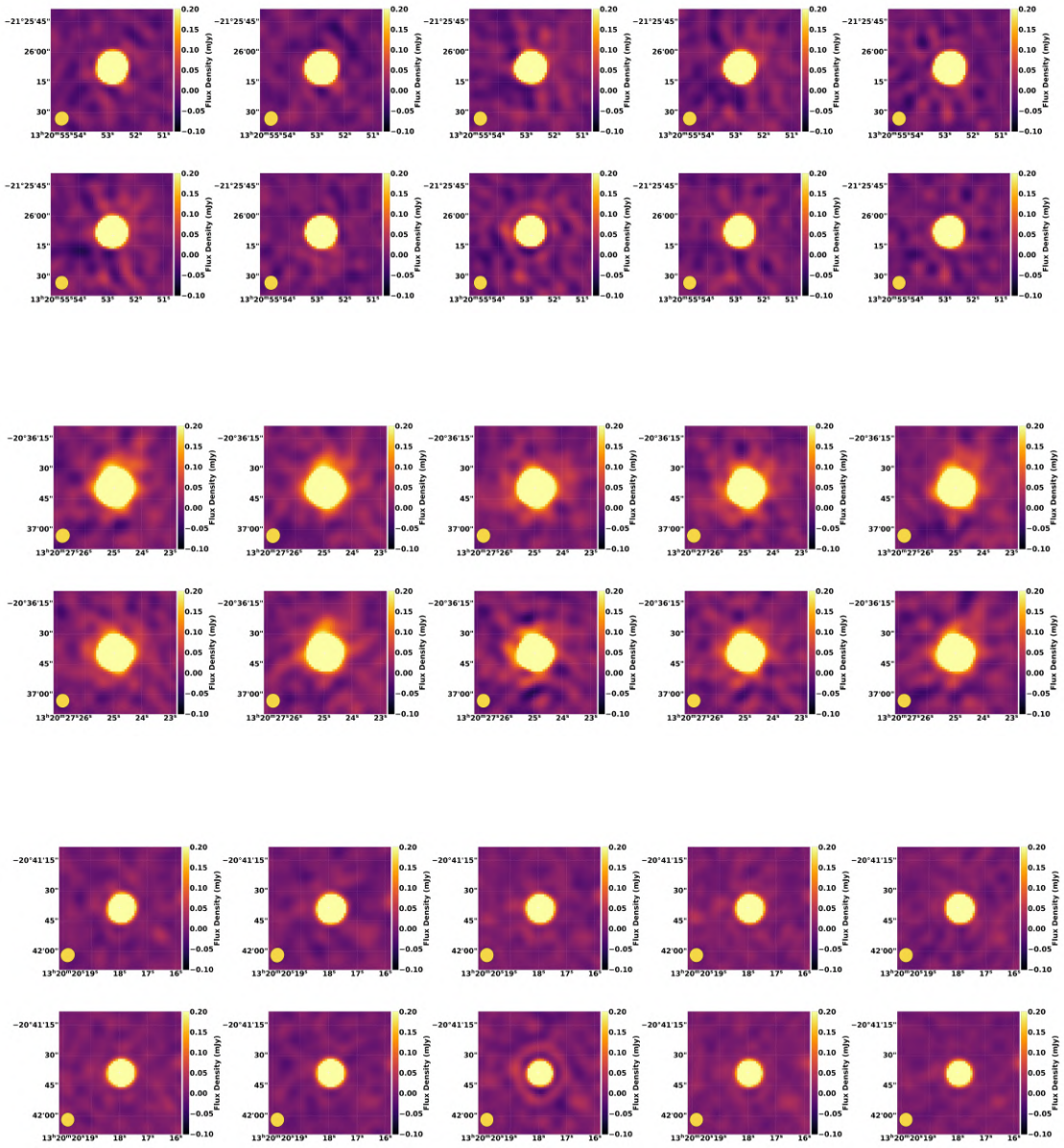
Appendix A

NGC 5068



Light curves of some selected green sources identified in Figure 3.1, corresponding to unique IDs 73107, 72639, 73052, 72434, 75427, and 72719. These light curves show no significant variability, suggesting that the sources remained stable throughout the observation period. In some cases, the error bars were too small to be visible on the light curves.

© University of Venda



The radio snapshot images of green sources identified in Figure 3.1. The first panel represents SRC72434; the middle panel corresponds to SRC72639; the bottom panel represents SRC72719. All the images are scaled to the same flux density range of (-0.10 to 0.20) mJy on a linear scale. The yellow circle in the lower-left corner of each image indicates the PSF. Flux remains constant throughout the whole 10 epochs.

© University of Venda



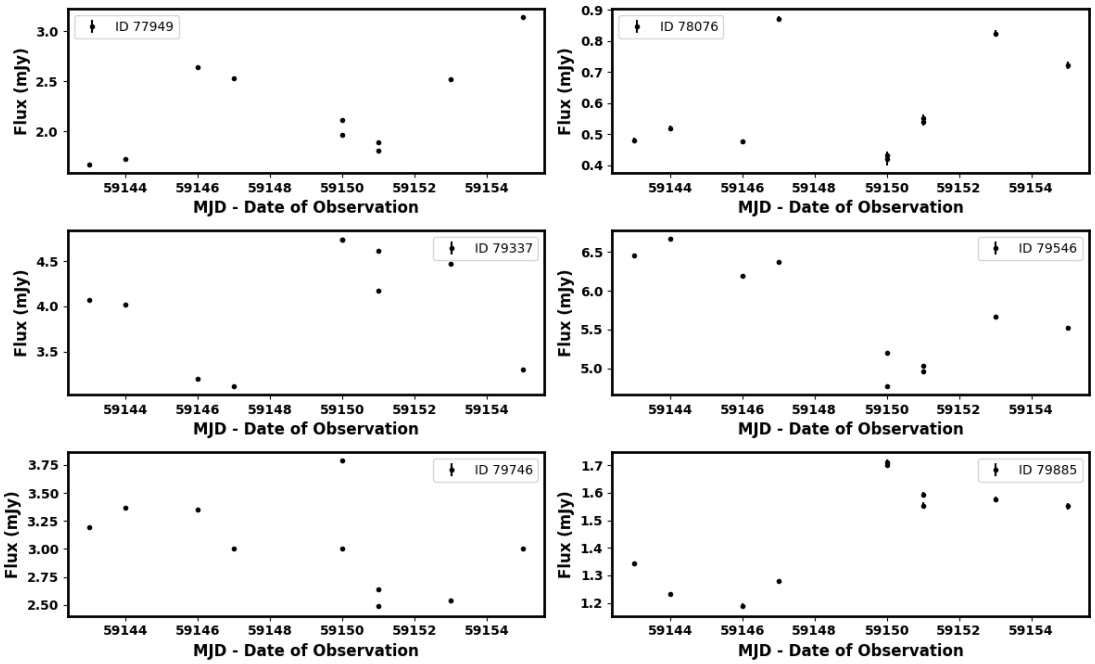
Snapshot of radio images of selected green sources from Figure 3.1. The first panel displays SRC73052, the middle panel shows SRC73107 and the last panel represents SRC75427. Every image has been linearly scaled to the same flux density range: (-0.10 to 0.20) mJy. The yellow circle in the lower-left corner shows each image's PSF. For the entire ten epochs, flux stays constant in each panel.

© University of Venda

University of Venda
Creating Future Leaders

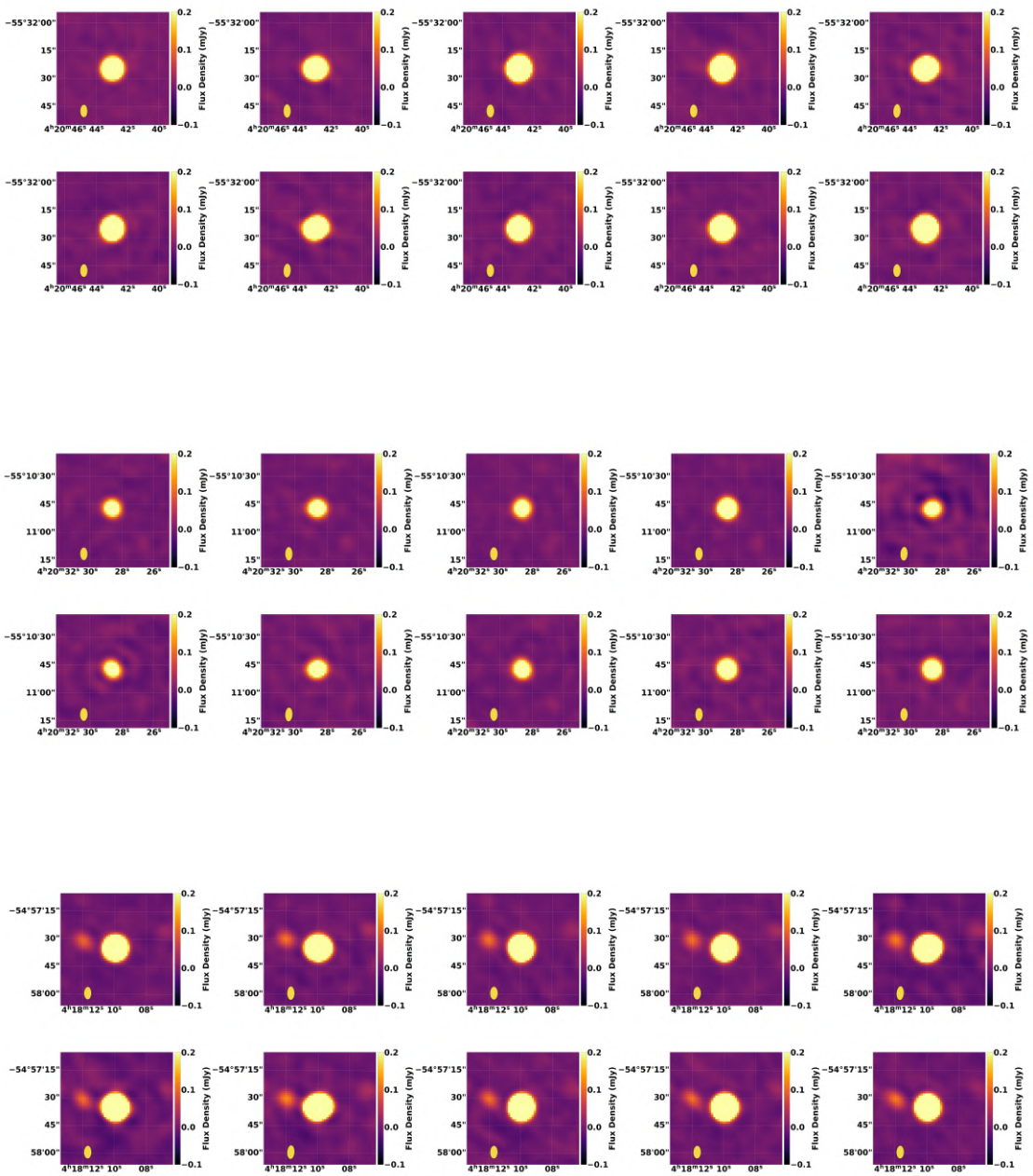
Appendix B

NGC 1566



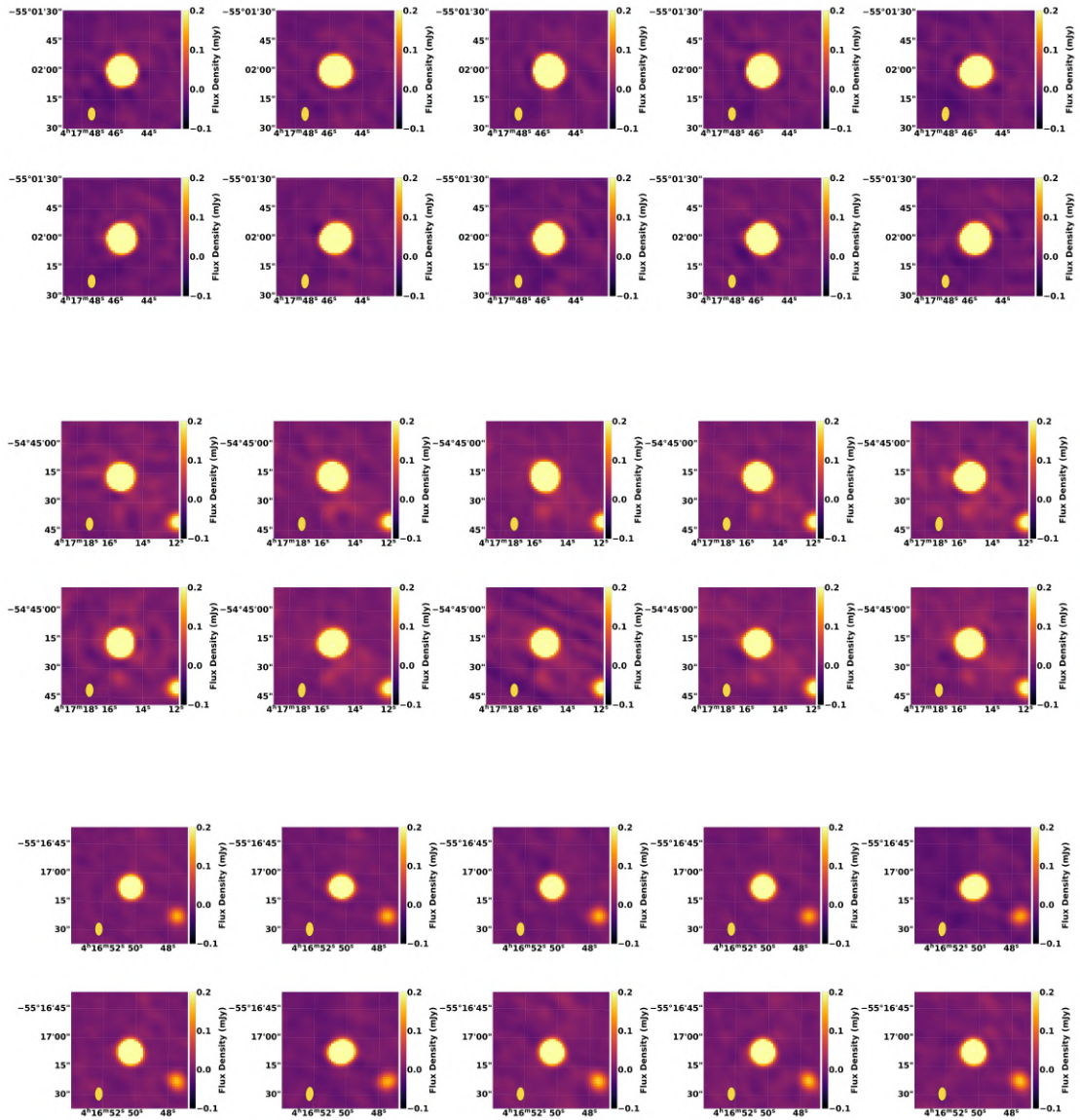
Light curves of some selected green sources identified in Figure 4.1, with unique IDs 77949, 78076, 79337, 79546, 79746 and 79885 display the flux density of each source as a function of observation date. Typical uncertainties in the flux density measurements are too small to be visible in the light curve.

© University of Venda



Snapshot of radio images of selected green sources from Figure 4.1. The first panel shows SRC77949, the middle panel shows SRC78076 and the last panel represents SRC79337. Every image has been linearly scaled to the same flux density range: (-0.10 to 0.20) mJy. The yellow circle in the lower-left corner shows each image's PSF. For the entire ten epochs, flux stays constant in each panel.

© University of Venda



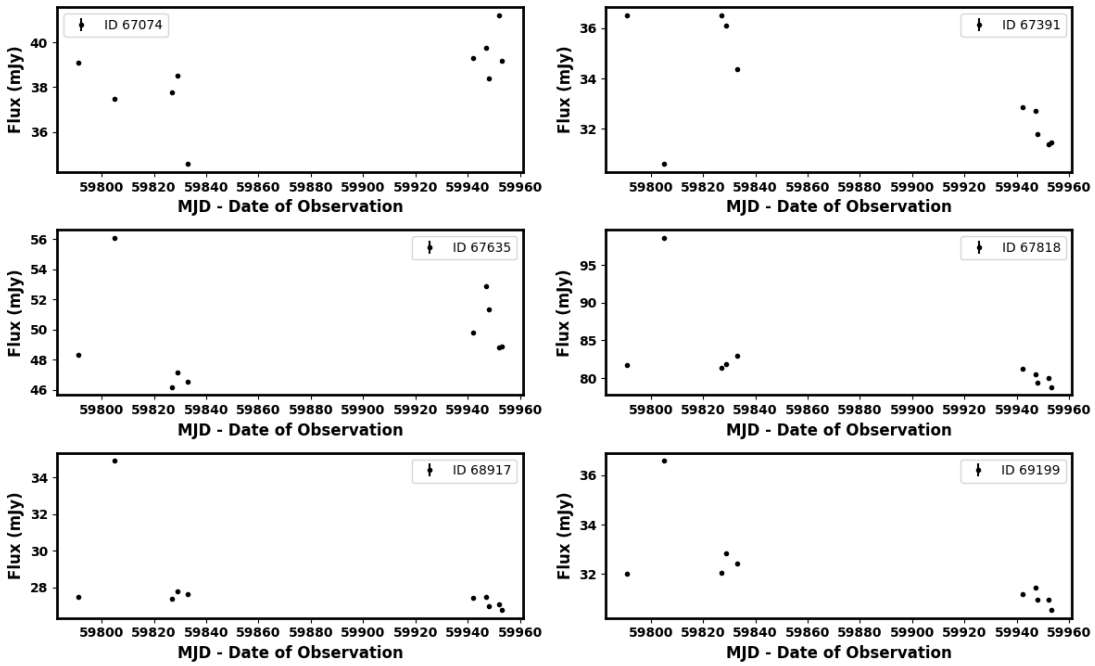
Snapshot of radio images of selected green sources from Figure 4.1. The first panel displays SRC79546, the middle panel shows SRC79746 and the last panel represents SRC79885. Every image has been linearly scaled to the same flux density range: (-0.10 to 0.20) mJy. The yellow circle in the lower-left corner shows each image's PSF. For the entire ten epochs, flux stays constant in each panel.

© University of Venda

University of Venda
Creating Future Leaders

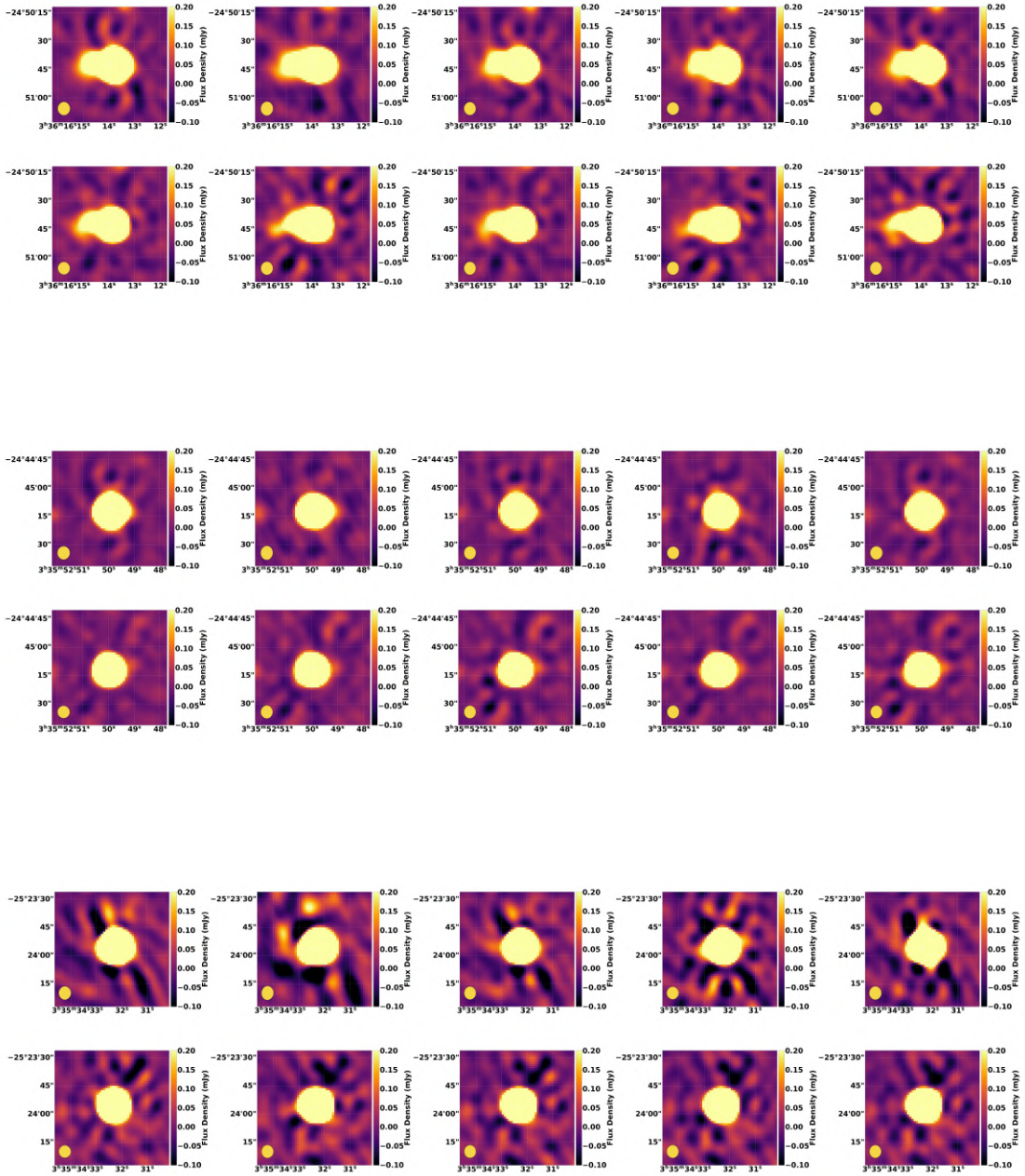
Appendix C

NGC 1371



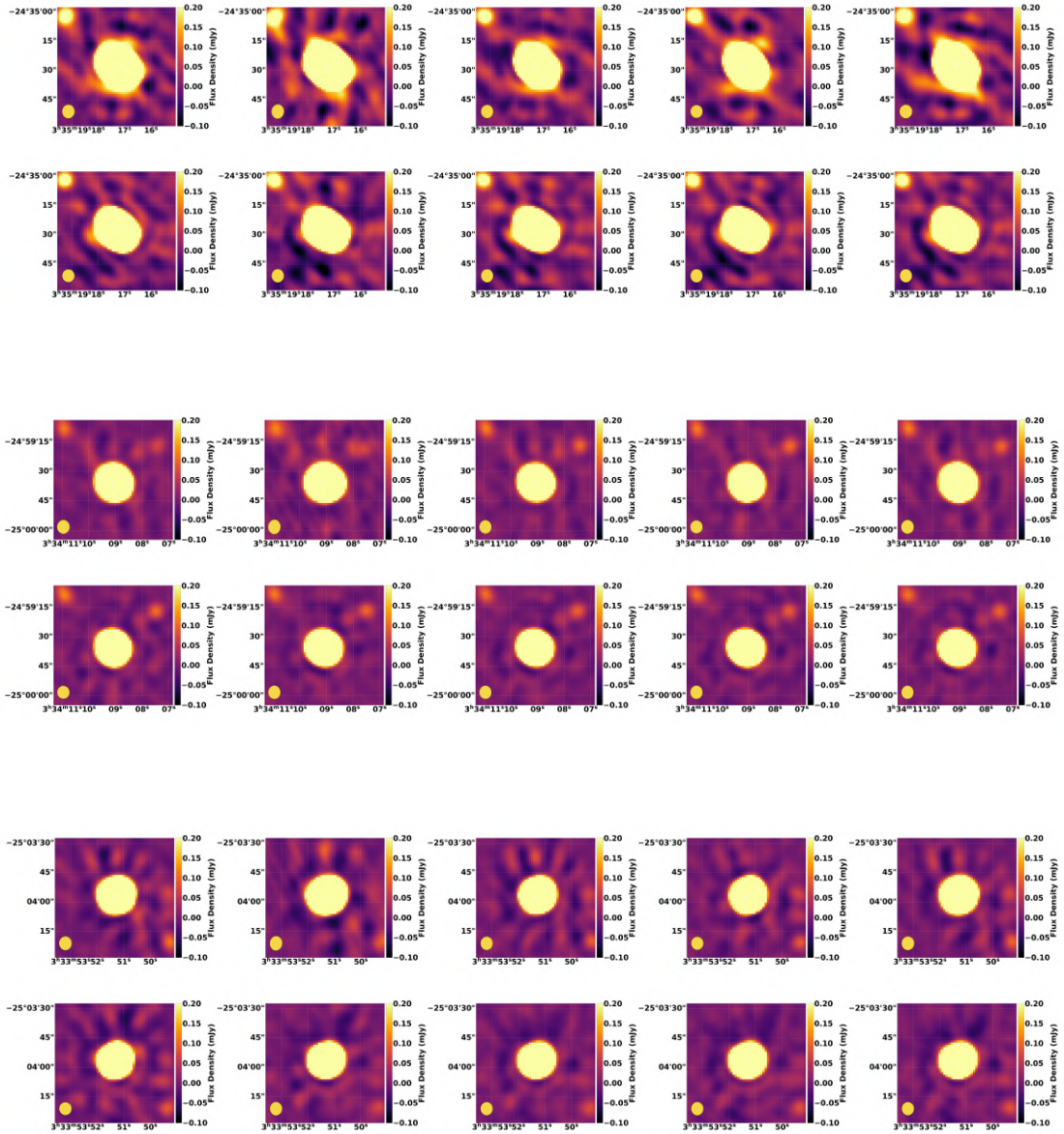
Light curves of some selected green sources identified in Figure 5.1 IDs 67074, 67391, 67635, 67818, 68917 and 69199 display the flux density of each source as a function of observation date. Typical uncertainties in the flux density measurements are too small to be visible in the light curve.

© University of Venda



Snapshot of radio images of selected green sources from Figure 5.1. The first panel displays SRC67074, the middle panel shows SRC67391 and the last panel represents SRC67635. Every image has been linearly scaled to the same flux density range: (-0.10 to 0.20) mJy. The yellow circle in the lower-left corner shows each image's PSF. For the entire ten epochs, flux stays constant in each panel.

© University of Venda



Snapshot of radio images of selected green sources from Figure 5.1. The first panel displays SRC67818, the middle panel shows SRC68917 and the last panel represents SRC69199. Every image has been linearly scaled to the same flux density range: (-0.10 to 0.20) mJy. The yellow circle in the lower-left corner shows each image's PSF. For the entire ten epochs, flux stays constant in each panel.

© University of Venda